Growth and Characterization of Epitaxial Manganese Silicide Thin Films

Dissertation zur Erlangung des naturwissenschaftlichen Doktorgrades der Julius-Maximilians-Universität Würzburg

vorgelegt von
Mirko Trabel
aus Eisingen

Würzburg 2019

Eingereicht am: 20.03.2019
bei der Fakultät für Physik und Astronomie

1. Gutachter: Prof. Dr. Karl Brunner
2. Gutachter: Prof. Dr. Grzegorz Karczewski
3. Gutachter: ....
der Dissertation

Vorsitzender Prof. Dr. Vladimir Dyakonov

1. Prüfer: Prof. Dr. Karl Brunner
2. Prüfer: Prof. Dr. Grzegorz Karczewski
3. Prüfer: Prof. Dr. Ronny Thomale
im Promotionkolloquiums

Tag des Promotionskolloquiums: 21.06.2019

Doktorurkunde ausgehändigt am: ....

Contents

1 Introduction **1**

2 Basic properties and methods **5**

2.1 Structural properties of bulk single crystal manganese silicide (MnSi) . 5

2.2 Structural characterization methods 8

2.2.1 Reflection High Energy Electron Diffraction (RHEED) 8

2.2.2 X-Ray Diffraction (XRD) 9

2.2.3 X-Ray Reflectivity (XRR) 12

2.3 Magnetic properties of bulk single crystal MnSi 13

2.4 Magnetic characterization methods 17

2.4.1 Magnetometry measurement 17

2.4.2 Magneto- and Hall-resistivity theory and measurement 19

2.4.3 Anisotropic MagnetoResistance (AMR) theory and measurement 22

3 Epitaxial growth and structural characterization of MnSi **29**

3.1 Historical growth process review 31

3.2 Growth process overview 34

3.2.1 Substrate preparation 34

3.2.2 Seed layer 39

3.2.3 MnSi layer and cap 41

3.3 Basic structural characterization 50

3.4 Structural characterization of twin domains 59

3.5 Suppression of twin domains 69

3.5.1 Growth on Si(111) substrate with miscut 69

3.5.2 Growth on chiral Si surfaces 72

4 Magnetic characterization of MnSi 87
4.1 Magnetometry . . . 87
4.2 Magneto- and Hall-resistivity . . . 95
4.3 AMR and Planar Hall Effect (PHE) . . . 101
4.3.1 AMR and PHE in the field polarized phase . . . 101
4.3.2 AMR and PHE below critical field and temperature . . . 113

5 Summary 117

6 Zusammenfassung 121

Bibliography 125

Publications and conference contributions 139

Acknowledgments 141

Glossary

AFM Atomic Force Microscopy.

AHE Anomalous Hall Effect.

AMR Anisotropic MagnetoResistance.

CBED Convergent Beam Electron Diffraction.

EDX Energy Dispersive X-Ray spectroscopy, also EDS.

FWHM Full Width Half Maximum.

HMS Higher Manganese Silicide.

MBE Molecular Beam Epitaxy.

ML MonoLayer.

PHE Planar Hall Effect.

RHEED Reflection High Energy Electron Diffraction.

SAED Selected Area Electron Diffraction.

SEM Scanning Electron Microscopy.

SPE Solid Phase Epitaxy.

SQUID Superconducting Quantum Interference Device.

TEM Tunneling Electron Microscopy.

XRD X-Ray Diffraction.

XRR X-Ray Reflectivity.

1 Introduction

Manganese silicide (MnSi) belongs to a group of noncentrosymmetric materials, that are very interesting because of their unusual spin structure. Here the spins are tilted to each instead of a parallel or antiparallel alignment, as for ferro- or antiferromagnets. This results in a rich magnetic phase diagram with a helical ground state, whose chirality depends on the chirality of the crystal structure [IEM+85].
The most interesting magnetic phase is probably the skyrmion lattice, a lattice of vortex like spin arrangements, which was first experimentally demonstrated in MnSi by Mühlbauer *et al.* [MBJ+09]. This early experimental results made MnSi the prototype material for a lot of investigations of the nature of the skyrmion lattice.
The main goal for applications is to use skyrmions as information carriers in magnetic memory or logic devices. Such applications, for example a racetrack memory system with skyrmions instead of Domain Walls, were theoretically proposed with a broad overview of the current status of the field discussed by Kang *et al.* [KHZ+16] [KBSR11, FCS13].
What makes skyrmions interesting for this type of application is the small skyrmion lattice constant of about 19 nm for MnSi, possibly leading to a higher information density than possible with a typical Domain Wall spacing above 30 nm, and the low current density of MAm^{-2}, orders of magnitude below typical values for Domain Wall motion, required to manipulate the skyrmion lattice by spin transfer torque [MSK+13, KHZ+16, JMP+10].
But there are also two main obstacles, hindering the implementation of these applications. One of them is the low critical temperature of about 30 K for bulk MnSi, above which the system becomes paramagnetic like [WWSW66]. However the critical temperature, as well as the magnetic field and temperature boundaries of the skyrmion phase can be influenced by applying pressure [RHF+13]. Molecular Beam Epitaxy (MBE) of MnSi on Si(111) is supposed to result in epitaxial strain, owing to the differing lattice constants, which was proposed as a tool to investigate the in-

fluence of pressure on the magnetic phases [KKM+10]. Instead of pressure chambers with isotropic pressure, a more appropriate comparison to the epitaxial strain would be uniaxial stress. Experiments on bulk MnSi with uniaxial stress perpendicular or parallel to the applied magnetic field show that strain engineering can be used to create or annihilate skyrmions [NNK+15]. Transferring these results to MnSi on Si(111) would result in a suppression of the skyrmion phase for a magnetic field applied out of the layer plane and a stabilization for a magnetic field applied in the layer plane. This is a hot topic and controversially discussed in literature, an overview of which can be found in section 2.3. Therefore the possibility to stabilize the skyrmion phase makes the case of a magnetic field in the layer plane of MnSi on Si(111) very interesting to investigate, which will be a main topic of this thesis.
The other main obstacle is the occurrence of twin domains with different crystal chirality in epitaxial MnSi layers. Both, the chirality of the helical state and of the skyrmion, are linked to the chirality of the crystal structure [IEM+85, MSK+13]. Therefore skyrmion transport through twin domain boundaries could be problematic, as they would eventually have to change their chirality. This could prevent the application of skyrmions as information carriers, as a path without domain boundaries would be needed for a racetrack. For this reason the characterization and suppression of twin domains are the other main focus of the present thesis.
The occurrence of such twin domains is not only an obstacle in MnSi but also in FeGe on Si(111), which also belongs to this group of noncentrosymmetric materials exhibiting a skyrmion lattice [YKO+11, HC12]. This material has other disadvantages and advantages compared to MnSi, like a larger skyrmion lattice constant of about 70 nm or a way higher critical temperature of about 270 K. [YKO+11, HC12, ARE+18]
As both materials are grown on Si(111) a twin suppression method found for one of them could eventually also be applied to the other material, which makes the goal of the present thesis even more important.
To demonstrate the occurrence of twin domains, their characteristics and influence on magnetotransport properties, as well as to investigate ways to suppress them, the thesis is structured as follows. In the second chapter, basic structural and magnetic properties of MnSi are discussed, together with explanations of the applied experimental methods. This is followed by a historical growth process review at the beginning of the third chapter. In the first half of the third chapter, an overview of the applied growth process and structural characterization is given. In the second half, the struc-

tural characterization of the aforementioned twin domains, as well as their successful suppression are demonstrated.

The fourth chapter is concerned with the magnetic and magnetotransport properties of MnSi and the influence of twinning on them. These are studied by Superconducting Quantum Interference Device (SQUID) magnetometry, as well as magneto- and Hall-resistivity measurements, and Anisotropic MagnetoResistance (AMR) and Planar Hall Effect (PHE) measurements, experimental methods that are discussed in the following chapter.

2 Basic properties and methods

MnSi belongs to a group of noncentrosymmetric materials, such as FeGe, $Fe_xCo_{1-x}Si$ and $Co_xMn_{1-x}Si$, which gathered interest during the 70s and 80s because of a helical spin arrangement arising from the reduced symmetry of their B20 crystal structure [LBA+70, ITBR76, BVT+81, BVR83].
This spin structure is caused by competition between exchange interaction and the Dzyaloshinsky-Moriya interaction, where the later occurs because the crystal structure is lacking inversion symmetry [Dzy58, Mor60, Mor76, MM78, BJ80, NYHK80].
In the following sections the principal crystal structure of bulk single crystal MnSi will be discussed first, followed by investigation methods. Afterwards an overview of the magnetic and magnetotransport properties is given, followed by an explanation of the methods to investigate them.

2.1 Structural properties of bulk single crystal manganese silicide (MnSi)

MnSi has the B20 crystal structure, which is a cubic crystal with the $P2_13$ space group and a lattice constant of $a = 4.5603(2)\text{Å}$ [JR91]. It can be described as an fcc lattice with each of the Mn and Si atoms of the cubic unit cell displaced with respect to the fcc positions. MnSi exists in two chiralities, right and left handed MnSi. For the right handed crystal structure, the atoms occupy the positions (x, y, z)

$$\begin{aligned}
&(u_A, u_A, u_A) \\
&\left(\frac{1}{2} + u_A, \frac{1}{2} - u_A, -u_A\right) \\
&\left(-u_A, \frac{1}{2} + u_A, \frac{1}{2} - u_A\right) \\
&\left(\frac{1}{2} - u_A, -u_A, \frac{1}{2} + u_A\right) \quad ,
\end{aligned} \tag{2.1}$$

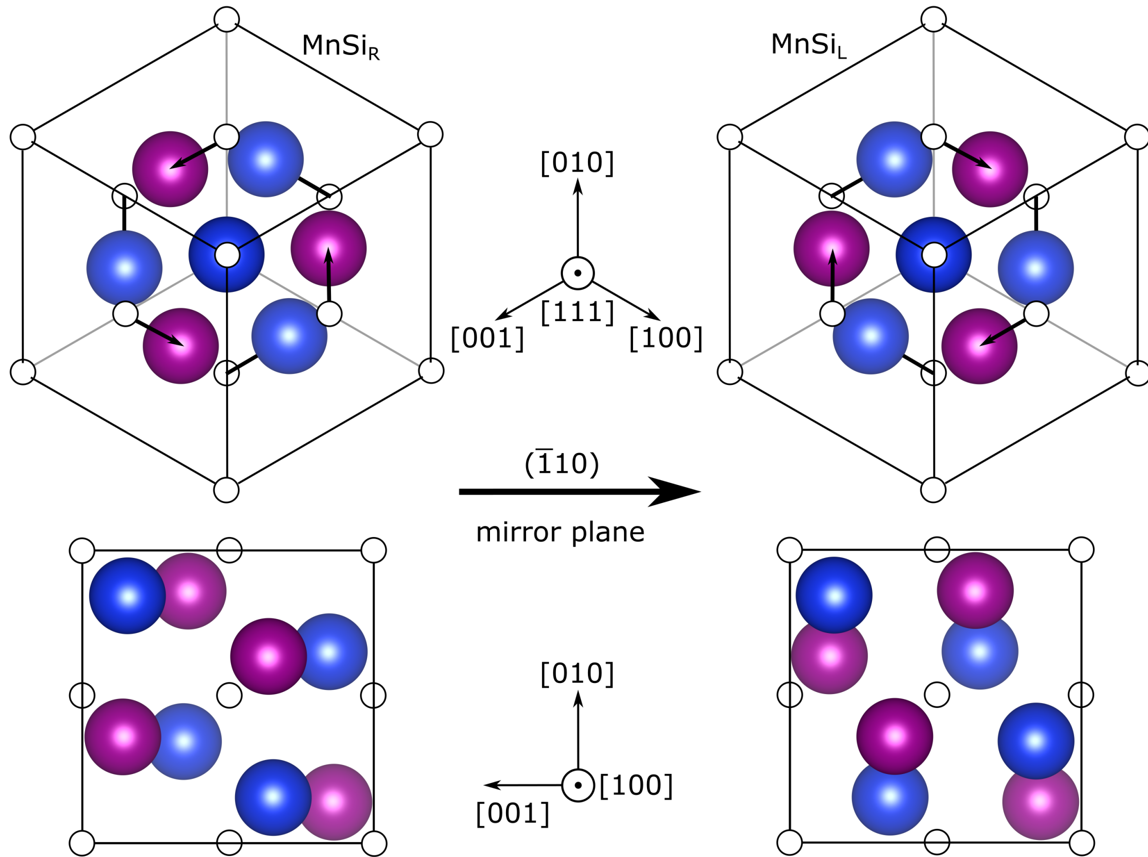

Figure 2.1: B20 crystal structure of right- and left-handed MnSi along the [111] and [100] direction with fcc positions represented by the white balls and the displacements (indicated by the arrows) of Mn (violet) and Si (blue) atoms with regard to this positions. Pictures of the crystal structures have been produced with Vesta 3 [MI11].

with $u_{\mathrm{Mn}} = 0.138$ and $u_{\mathrm{Si}} = 0.846(\equiv -0.154)$ in units of a [IEM+85]. This configuration is shown in Fig. 2.1 on the left side. It is connected to the left handed crystal structure, shown in Fig. 2.1 on the right side, by a mirror operation at the $(\bar{1}10)$ plane or an equivalent plane like $(1\bar{1}0)$, that is exchanging the x and y coordinates for all

atom positions. Thus the atom positions are

$$\begin{aligned}
&(u_A, u_A, u_A)\\
&\left(\frac{1}{2} - u_A, \frac{1}{2} + u_A, -u_A\right)\\
&\left(\frac{1}{2} + u_A, -u_A, \frac{1}{2} - u_A\right)\\
&\left(-u_A, \frac{1}{2} - u_A, \frac{1}{2} + u_A\right)
\end{aligned} \tag{2.2}$$

for left handed MnSi. [IEM+85]
With conventional X-Ray Diffraction (XRD) the structure factor for right handed MnSi with (111) surface and left handed MnSi with $(\bar{1}\bar{1}\bar{1})$ surface are identical, meaning this experimental method can not be directly used to identify the handedness, which will be discussed in more detail in the next chapters. However, the anomalous dispersion of XRD lifts this degeneracy and has been used to determine the handedness of the crystal structure. A separate method successfully used to confirm the results is Convergent Beam Electron Diffraction (CBED). [IEM+85, TTIE85]
Single crystals of MnSi have been grown by the Czochralski method [ITBR76]. The method has been shown by Dyadkin *et al.* [DGM+11] to result mostly in single crystals with the handedness depending on the used seed crystal. These results have to be evaluated carefully as the used atom positions and definitions of handedness are in contrast to the ones cited within their work and previously described.
The main focus of chapter 3 is how the twinning can be identified in epitaxially grown layers, as well as possibilities to suppress twinning.

2.2 Structural characterization methods

The aforementioned structural properties as well as the crystal quality of the MnSi thin film presented in this work are mainly studied by diffraction methods. First Reflection High Energy Electron Diffraction (RHEED), a surface analysis method that can be applied in situ, and afterwards by X-Ray Diffraction and Reflectivity. These methods are explained in the following.

2.2.1 Reflection High Energy Electron Diffraction (RHEED)

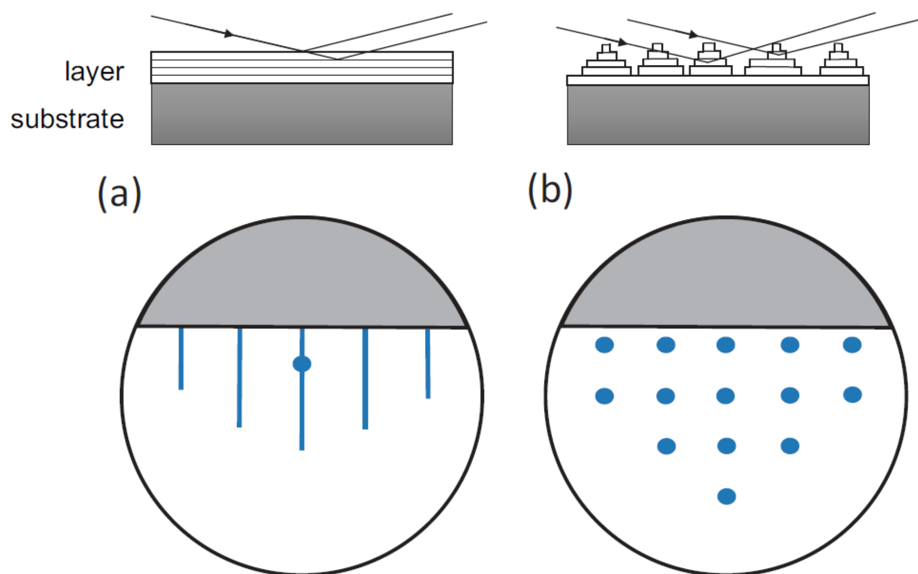

Figure 2.2: Sketch of the RHEED picture for
a) a flat surface and
b) a rough surface with islands.
Reprinted with permission from Steffen Schreyeck, Molecular Beam Epitaxy and Characterization of Bi-Based V_2VI_3 Topological Insulators, Dissertation, urn:nbn:de:bvb:20opus-145812, Julius-Maximilians-Universität Würzburg, 2016. [Sch16]

The following explanation of RHEED, a surface analysis method, is based on [IC04, HS96] and can be found in more detail there. For RHEED a high energy electron beam from the RHEED gun hits the substrate surface under a low incident angle, which means that only the upper atomic layers are penetrated and investigated. The diffraction pattern will then be visualized with a fluorescent RHEED screen and can be

analyzed. Diffraction only occurs at intersections of the Ewald sphere with reciprocal lattice points or, in the case of a flat surface, reciprocal lattice rods perpendicular to the surface. This leads to long streaks on the RHEED screen in the case of a perfectly flat surface. A rough surface or crystallites at the surface on the other hand leads to a spotty RHEED pattern, which comes from transmission instead of reflection. This is illustrated in Fig. 2.2 a) for a flat surface and b) for a rough surface with islands. Reconstruction of the surface, meaning that the surface unit cell is different from the underlying bulk unit cell, are also visible, as RHEED is such a surface sensitive analysis method.

2.2.2 X-Ray Diffraction (XRD)

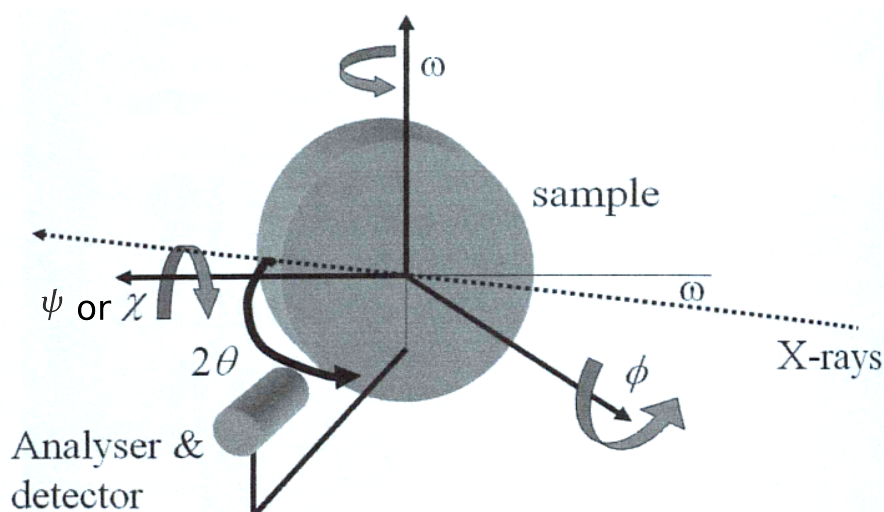

Figure 2.3: Sketch of the relevant XRD angles.
X-Ray Scattering from Semiconductors and Other Materials by Fewster, Paul F Reproduced with permission of WORLD SCIENTIFIC in the format Republish in a thesis/dissertation via Copyright Clearance Center. With additional angle label ψ. [Few15]

For XRD measurements the sample is placed inside a diffractometer and the orientation of the sample with respect to the incident beam and scattered beam to the detector can be varied as depicted in Fig. 2.3 a). The incidence angle ω, between incident beam and sample surface, and 2θ, between detector and sample surface, can be changed. Additionally the out of plane tilt angle ψ, also often called χ, and the

azimuthal rotation angle ϕ are varied. The prime beam of the X-Ray source travels through a slit, mirror and monochromator setup before arriving at the sample. The scattered beam goes directly to the detector or first through a slit analyzer. For asymmetric reflections a parallel plate collimator or soller at the detector side is used as well. These can be described by a set of parallel plates which filter out beams tilted away from the parallel beam.
The X-Rays are scattered on the crystal lattice planes and the different lattice parameters of the phases lead to different 2θ values owing to the Bragg relation

$$\sin(\theta) = \frac{\lambda}{2d_{hkl}} \tag{2.3}$$

with the used wavelength $\lambda = 1.5406$Å of CuKα_1 [MNT16] and the lattice plane spacing

$$d_{hkl} = \frac{a}{\sqrt{h^2 + k^2 + l^2}} \ . \tag{2.4}$$

Here h, k, l are the Miller indices of the reflection and a the cubic lattice constant. [Few15]
For symmetric reflections, which have lattice planes parallel to the nominal layer surface, the angles ψ and ϕ are only used to adjust the orientation of the surface with respect to the diffractometer coordinate system. For asymmetric reflections ψ and ϕ are needed to bring the lattice plane into reflection condition. With the surface normal $[mno]$ of the layer, the inclination angle ψ for a reflection hkl can be calculated with

$$\psi = \frac{[hkl] \cdot [mno]}{|\,[hkl]\,||\,[mno]\,|} \ . \tag{2.5}$$

The azimuthal angle ϕ to the projection of a reference direction $[abc]$ on the surface can be calculated with

$$\begin{aligned}
\phi\,(hkl) =& \phi'_m\,(hkl) \ \text{ for} \\
& [mno] \cdot \left(\left([abc] - \frac{[abc] \cdot [mno]}{[mno] \cdot [mno]} [mno] \right) \times \left([hkl] - \frac{[hkl] \cdot [mno]}{[mno] \cdot [mno]} [mno] \right) \right) \geq 0 \\
\phi\,(hkl) =& 360° - \phi'_m\,(hkl) \ \text{ for} \\
& [mno] \cdot \left(\left([abc] - \frac{[abc] \cdot [mno]}{[mno] \cdot [mno]} [mno] \right) \times \left([hkl] - \frac{[hkl] \cdot [mno]}{[mno] \cdot [mno]} [mno] \right) \right) < 0
\end{aligned} \tag{2.6}$$

and

$$\phi'_{\mathrm{m}}(hkl) = \arccos\left(\frac{\left([hkl] - \frac{[hkl]\cdot[mno]}{[mno]\cdot[mno]}[mno]\right)\cdot\left([abc] - \frac{[abc]\cdot[mno]}{[mno]\cdot[mno]}[mno]\right)]}{|\,[hkl] - \frac{[hkl]\cdot[mno]}{[mno]\cdot[mno]}[mno]\,||\left([abc] - \frac{[abc]\cdot[mno]}{[mno]\cdot[mno]}[mno]\right)|}\right) . \quad (2.7)$$

The relative peak intensity of a reflection hkl can be estimated from the structure factor F as $|F(hkl)|^2$ is proportional to the intensities.

$$F(hkl) = \sum_j f_j e^{2\pi i(hx_j+ky_j+lz_j)} \quad (2.8)$$

summing up over all atoms j in a unit cell with the atomic scattering factor f_j. [IEM+85, Wil95]

With the atom coordinates of right handed MnSi described in Eq. 2.1 one gets [IEM+85]

$$\begin{aligned} F^{\mathrm{R}}(hkl) = \sum_{A=\mathrm{Si,Mn}} f_A[&e^{2\pi i(h+k+l)u_A} + e^{2\pi i(h-k-l)u_A}e^{\pi i(h+k)} \\ &+ e^{2\pi i(-h+k-l)u_A}e^{\pi i(k+l)} + e^{2\pi i(-h-k+l)u_A}e^{\pi i(l+h)}] . \end{aligned} \quad (2.9)$$

This results in an equal structure factor for even permutations of (hkl) or all h, k, l even or all h, k, l odd and in different structure factors for odd permutations.

Without dispersion corrections the atomic scattering factors can by interpolated with [Wil95]

$$f\left(\frac{\sin\theta}{\lambda}\right) = \sum_{i=1}^{4} a_i e^{\left(-b_i \frac{\sin^2\theta}{\lambda^2}\right)} + c \quad (2.10)$$

for small scattering angles $\sin\theta/\lambda < 2.0\text{Å}^{-1}$ with the coefficients listed in table 2.1 Taking the $\{210\}$ reflection family as an example $1/(2d_{210}) = \sin\theta/\lambda \approx 0.245\text{Å}^{-1}$ results in $f_{\mathrm{Si}} \approx 8.93$ and $f_{\mathrm{Mn}} = 17.53$. Two different intensities appear for this reflection family with the atomic scattering factor ratio $|F(210)|^2/|F(120)|^2 \approx 9.6$.

The change of chirality from right- to left-handed MnSi by a mirror operation at the $(\bar{1}10)$ plane, as shown in section 2.1, changes the structure factor to [IEM+85]

$$\begin{aligned} F^{\mathrm{L}}(hkl) = \sum_{A=\mathrm{Si,Mn}} f_A[&e^{2\pi i(h+k+l)u_A} + e^{2\pi i(h-k-l)u_A}e^{\pi i(l+h)} \\ &+ e^{2\pi i(-h+k-l)u_A}e^{\pi i(h+k)} + e^{2\pi i(-h-k+l)u_A}e^{\pi i(k+l)}] , \end{aligned} \quad (2.11)$$

as the atom positions change. Because of that, the structure factor for an odd permu-

Element	Z	a_1	b_1	a_2	b_2
Si	14	6.29150	2.43860	3.03530	32.3337
Mn	25	11.2819	5.3409	7.35730	0.34320
Element	a_3	b_3	a_4	b_4	c
Si	1.98910	0.678500	1.54100	81.6937	1.14070
Mn	3.01930	17.8674	2.24410	83.7543	1.08960

Table 2.1: Parameter for the atomic scattering factor interpolation with Eq. 2.10. b_i are in units of $Å^2$. Taken from [Wil95].

tation of (hkl) becomes equal to the structure factor of the original (hkl) for the other chirality meaning $|F^{\mathrm{R}}(hkl)| = |F^{\mathrm{L}}(khl)|$ [IEM+85]. For the {210} reflection family a high intensity for one chirality switches to a low intensity for the other chirality.

2.2.3 X-Ray Reflectivity (XRR)

X-Ray Reflectivity (XRR)-measurements are done under a low incident angle as symmetric $2\theta-\theta$-scans, meaning nominal $\omega=\theta$, and can give different information about material and layer properties. The critical angle until which total reflectivity occurs can give information about the electron density of the material. What complicates this analysis is a decrease in reflective intensity for lower angles as the area illuminated by the X-Ray beam is larger than the sample size [Bir06]. This effect is illustrated in Fig. 2.4 for XRR-scans of quartz glass with different sizes.
The interference of reflected beams at the various interfaces leads to intensity maxima with index m, which can be used to calculate the thickness d of a layer by the separation of two adjacent fringes significantly above the critical angle [Bir06]

$$d \approx \frac{\lambda}{2\theta_{m+1} - 2\theta_m} \tag{2.12}$$

with the used wavelength λ of $\mathrm{CuK}\alpha_1$.
This is obviously more complicated for multiple layer structures, since several beams interfere with each other, but nowadays simulation programs are used where different interface models, interface and surface roughness and instrumental functions can be accounted for. The simulations shown in this work are done with Leptos 7.6 [Bru].

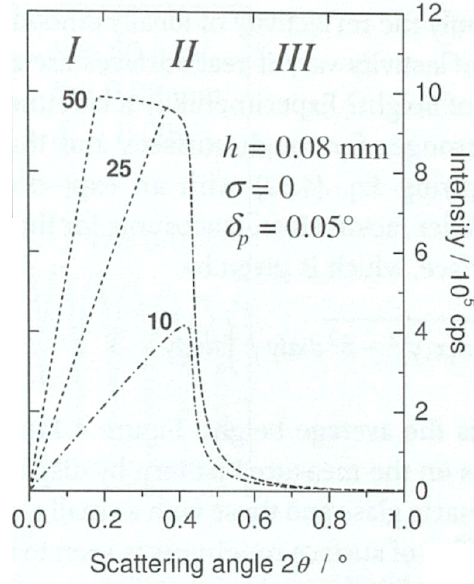

Figure 2.4: XRR-scans of quartz glass with length 10 mm, 25 mm and 50 mm. Reprinted with permission from John Wiley and Sons: Thin Film Analysis by X-Ray Scattering, Grazing Incidence Configurations, Dr. Mario Birkholz, Copyright 2006 Wiley-VCH Verlag GmbH & Co. KGaA, Weinheim. [Bir06]

2.3 Magnetic properties of bulk single crystal MnSi

The occurrence of a helical spin structure is one interesting aspect of MnSi and first led to interest in its magnetic properties. To understand this phenomenon one has to understand the influence of the so called Dzyaloshinsky-Moriya interaction, which prefers a perpendicular alignment of neighboring spins (magnetic moments).
The magnetic energy density of a system including the Dzyaloshinsky-Moriya interaction has been described based on the free energy functional by Bak and Jensen [BJ80] and other previous work [Dzy64, NYHK80]. In an magnetic field $\boldsymbol{H}$ with the magnetization vector $\boldsymbol{M}$ it becomes [BLRB10, WBBM14]

$$\begin{aligned} w(\boldsymbol{M}) = & A(\nabla \boldsymbol{M})^2 \\ & + D\boldsymbol{M} \cdot (\nabla \times \boldsymbol{M}) \\ & + \sum_i \left[B^* (\partial_i M_i)^2 + K_c M_i^4 \right] \\ & - \boldsymbol{M} \cdot \boldsymbol{H} \; . \end{aligned} \tag{2.13}$$

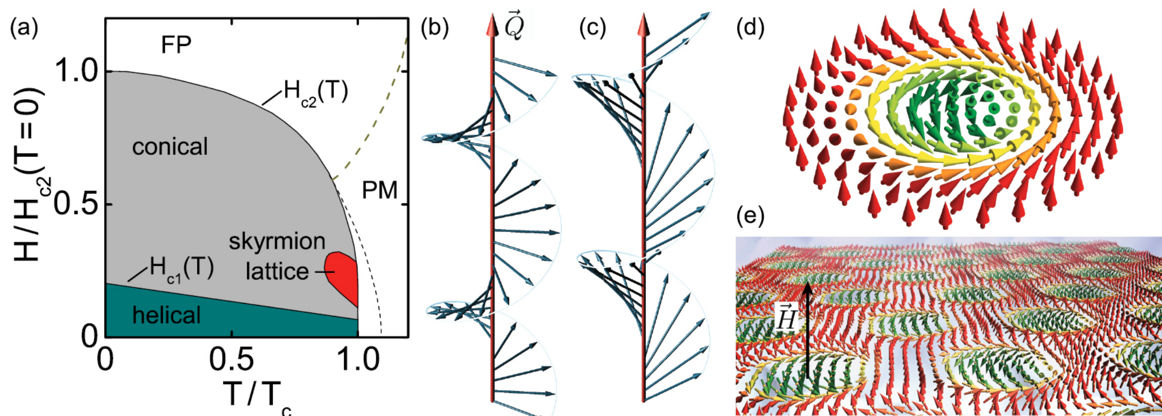

Figure 2.5: a) Magnetic field and temperature dependent phase diagram of cubic chiral magnets with schematic representations of the helical phase in b), the conical phase in c), the skyrmion lattice in e) and a single skyrmion in d). Reprinted from Markus Garst, Johannes Waizner, and Dirk Grundler, Journal of Physics D: Applied Physics, 50, 293002, 2017, DOI: 10.1088/1361-6463/aa7573, Creative Commons Attribution 3.0 licence (http://creativecommons.org/licenses/by/3.0). [GWG17]

Here the first term describes the exchange interaction with stiffness constant A and the second term describes the Dzyaloshinsky-Moriya interaction with the Dzyaloshinsky constant D. The second term prefers a perpendicular arrangement of the neighboring spins and is a small perturbation to the parallel arrangement preferred by the exchange interaction [BJ80]. The third term describes exchange and cubic anisotropies with the corresponding constants B^* and K_c and the last term is the Zeeman energy.

The result of the competition of magnetic interactions on the magnetic phases is depicted in Fig. 2.5. Above the critical temperature T_c, which is about 30 K for bulk MnSi [WWSW66], the system is paramagnetic like. Below T_c and without an external magnetic field $H = 0$ the system is in a helical state, as shown in Fig. 2.5 b). This helical state corresponds to the displayed spin spiral where the sign of the anisotropy coefficient B^* from Eq. 2.13 determines the propagation direction either along $\langle 111 \rangle$ or $\langle 100 \rangle$ [BJ80]. The handedness of the spin spiral depends on the sign of the Dzyaloshinsky constant D in Eq. 2.13 and can be determined by polarized neutron diffraction. It was shown that the crystal handedness is directly linked to the magnetic handedness and that in MnSi a left handed crystal leads to a left handed spin helix. The periodicity of this spin helix is about 18 nm. [IEM+85, ITBR76]

In MnSi without an external magnetic field, domains with propagation directions along

⟨111⟩ exist. A magnetic field above a critical value H_{c1} leads to the conical phase with the propagation direction along and the spins tilting in the direction of the external field, as depicted in Fig. 2.5 c). Above the critical magnetic field H_{c2}, which is about 0.6 T [WWSW66], and below the critical temperature T_c the spins align along the external field and form a field polarized phase with a saturation moment of 0.4 μ_B per Mn atom [WWSW66].

In the red T, H region of Fig. 2.5 a new phase, the so called A phase, was discovered quite early on, without a proper explanation for the actual spin configuration within this region [KYKI76]. The understanding came decades later, again by means of polarized neutron diffraction [MBJ+09]. It was shown that within the A-phase the helices form triplets with propagation vectors perpendicular to the magnetic field and an angle of 120° between them. Neutron diffraction rocking curves also implied a long range order and the suggested underlying structure to explain this is the skyrmion lattice shown in Fig. 2.5 e) stabilized by thermal fluctuations. In addition, it was shown that the handedness of the skyrmion is linked to the handedness of the crystal structure in the same way as described for the spin helix [MSK+13].

Another prominent method to reveal the formation of the skyrmion lattice was the measurement of the topological Hall effect by Neubauer *et al.* [NPB+09], which appears as an additional contribution to the normal and anomalous Hall effect, arising from the orientation of spin polarization in the skyrmion lattice. Further explanations for the basic Hall effects can be read in chapter 2.4.2 and in the work of Nagaosa *et al.* [NSO+10].

There is a broad consensus that the skyrmion lattice occurs in bulk MnSi under the aforementioned conditions. The same can not be said about the occurrence of a skyrmion lattice in epitaxially grown thin films, where contradicting results can be found in the literature.

For a perpendicular magnetic field, measurements of the topological Hall effect, as well as Lorentz Tunneling Electron Microscopy (TEM), were used by Li *et al.* [LKY+13], similar to what was previously done on bulk MnSi. From the results the occurrence of a skyrmion lattice in a broad temperature and magnetic field region was concluded.

However, the methodology of the Lorentz TEM measurements was soon put into question. Additionally, differing explanations of the topological Hall effect were proposed. [MLRB14, LKY+14, WBBM14, MWL+14]

For a deeper understanding of the actual spin arrangement and with that the reason

for the topological Hall effect, methodologies like Lorentz TEM and spin polarized Atomic Force Microscopy (AFM) would have to be used. Using them, topological Hall effect measurements could directly be linked to specific magnetic structures. As these measurement methods were not available for this thesis, the topological Hall effect will not be discussed.
On the other hand a lot of publications exist claiming the occurrence of skyrmion strings for a magnetic field in the layer plane, but with varying temperature and magnetic field boundaries [WKQ+12, WKL+13, YKT+15, MWK+17].
But even here opposition exists with the work of Wiedemann *et al.* [WCZ+17] claiming that no skyrmions occur at least in the thick film limit.
In conclusion the case of a magnetic field in the layer plane seems still more promising but unresolved and is a big focus in later chapters of this work.

2.4 Magnetic characterization methods

The magnetic properties of the MnSi thin film presented in this work are studied by magnetometry and magnetotransport measurements. These methods as well as the underlying theoretical models are explained in the following.

2.4.1 Magnetometry measurement

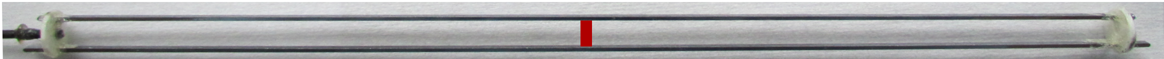

Figure 2.6: SQUID sample holder for perpendicular magnetic field measurements with the sample position sketched in red.

The SQUID magnetometry measurements shown in this work are done with a Quantum Design MPMS. The basic working principle and ways to reliably measure materials with a low magnetic moment are described by Sawicki *et al.* [SSN11]. The samples are glued with PMMA onto Si stripes, as these provide excellent magnetic uniformity and have a low temperature dependent magnetic moment which is necessary to measure the small magnetic moments of the MnSi layers [SSN11].
The sample holder for measurements with a magnetic field perpendicular to the layer plane is shown in Fig. 2.6, where the sample is glued in between two Si stripes at the center position sketched in red. For measurements with a magnetic field in the layer plane the sample can be glued on the side of the two stripes or on a single stripe holder. The first sample holders were build and improved during a collaboration visit to Prof. Sawicki at the Institute of Physics, Polish Academy of Science.
The raw measurement signal consists of a contribution from the silicon, possibly a contribution from measurement artifacts, and a contribution from the MnSi layer. All contributions have different magnetic field and temperature dependencies. Thus the dependencies have to be determined and subtracted to be able to acquire the actual MnSi moment from the raw data. The following part describes this data processing procedure, for reference measurements of a cleaned Si(111) substrate.
Fig. 2.7 a) shows the temperature dependence of the magnetic moment for the Si(111) substrate wafer piece at a magnetic field of $\mu_0 H = 2$ T. The temperature dependence

is described by a polynomial fit

$$\begin{aligned}\frac{m(T)}{m(300\text{K})} =& \mathrm{B}_0 + B_1T + B_2T^2 + B_3T^3 + B_4T^4 \\ &+ B_5T^5 + B_6T^6 + B_7T^7 + B_8T^8 + B_9T^9\end{aligned} \tag{2.14}$$

to the measurement data with the used values displayed in Tab. 2.2

Parameter	Value	Parameter	Value
B_0	1.0128	B_5	4.61×10^{-10}
B_1	2.77×10^{-3}	B_6	-2.41×10^{-12}
B_2	1.40×10^{-4}	B_7	7.49×10^{-15}
B_3	3.65×10^{-6}	B_8	-1.27×10^{-17}
B_4	-5.34×10^{-8}	B_9	9.12×10^{-21}

Table 2.2: Parameter for the polynomial fit in Eq. 2.14 shown in Fig. 2.7 a).

As the MnSi layer does not significantly contribute to the total magnetic moment at $T = 300$ K, the $m(300\text{K})$ value of a MnSi on Si(111) layer, scaled with Eq. 2.14, can be used to determine the substrate contribution at lower temperatures.
Measurements at the Si(111) substrate wafer piece can also be used to demonstrate flux trapping, an artifact that occurs for almost all measurements and has to be accounted for before further analysis [SSN11]. Fig. 2.7 b) shows the raw magnetic moment measurement at $T = 300$ K in a varied magnetic field μ_0H in the layer plane as blue dots together with linear fits to the negative and positive magnetic field region. The mean slope of the linear fits is used to subtract the diamagnetic signal and the result after subtraction is shown in Fig. 2.7 b) as purple dots. The residual signal has a weak curvature and stems from trapped flux within the superconducting magnet of the SQUID [SSN11]. This contribution is not temperature dependent, as can be seen from the measurement at $T = 1.8$ K after subtraction of the same linear background scaled with Eq. 2.14, which is shown in Fig. 2.7 b) as magenta dots. If this contribution is to big in comparison to the measurement signal it can be subtracted after determination at $T = 300$ K.
To determine this temperature independent contribution of the flux trapping, a Boltzmann function

$$y = A + \frac{B - A}{1 + \exp\left(\frac{x - x_0}{C}\right)} \tag{2.15}$$

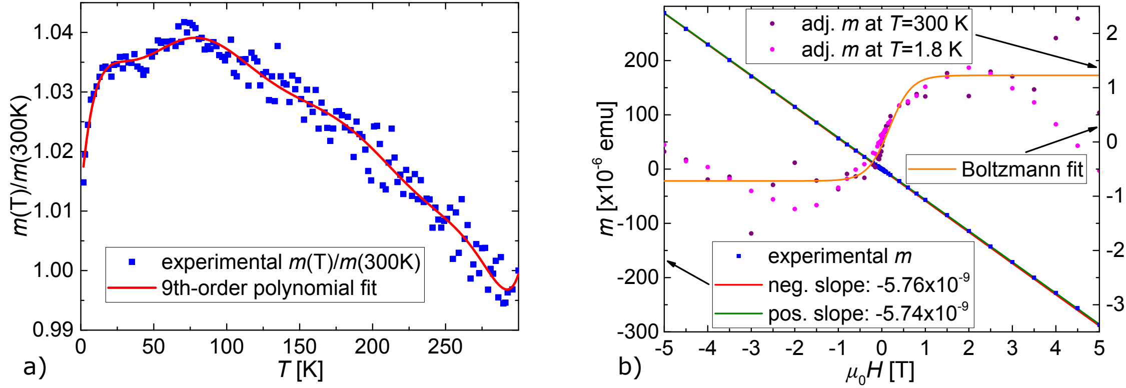

Figure 2.7: a) Temperature dependent magnetic moment of a Si(111) wafer piece at an in plane magnetic field of $\mu_0 H = 2$ T. Fit of Eq. 2.14 with Tab. 2.2. b) Raw in plane magnetic field dependent magnetic moment (left axis) in blue of the sample from a) at $T = 300$ K with linear fit to both magnetic field directions above ± 1 T. Adjusted magnetic moment (right axis) in purple for $T = 300$ K and magenta for $T = 150$ K. Fit of Boltzmann function according to Eq. 2.15 in orange.

is fitted to the adjusted $T = 300$ K curve and then subtracted from the measurements at lower temperature. As can be seen in Fig. 2.7 b), the fit has a large error which prevents the precise determination of absolute values. This data processing procedure is used to determine all magnetic moments for the MnSi layers shown in this work.

2.4.2 Magneto- and Hall-resistivity theory and measurement

Magnetotransport measurements are done with samples prepared as lithographic Hallbars, a sketch of which can be seen Fig. 2.8. Different designs are used with the width ranging between 1 and 100 µm and the distance between the contacts between 3 and 300 µm. The Hallbar design and fabrication process is described in the thesis of Constantino [Con13] and was later on further improved by M. Baussenwein by a different Hallbar design and etching steps.

The four point measurements are done either with a DC- or AC-voltage applied along a reference resistor and the Hallbar, as sketched in Fig. 2.8 a) or with a LR700 resistance bridge as constant AC current source as sketched in 2.8 b). In the first case the voltage drop over the reference resistor is used to calculate the current. The voltage drop over the Hallbar contacts is measured with 1:1 amplifiers and voltmeters and

in the case of an AC-Voltage with Lock-In technique. With the current through the Hallbar and the voltage drop at the contacts the resistances can be calculated. In the second case the LR700 resistance bridge is not only used as a constant AC-current source but also to directly measure the resistance. Additional Lock-Ins are used as well to measure more contacts simultaneously. With the dimensions of the Hallbar, layer thickness and the resistances the resistivities can be calculated. To measure temperature dependencies the Hallbars are placed in a He^4 cryostat, where the sample is heated from base temperature. For measurements of the magnetic field dependencies the cryostats are equipped with magnets where the sample can be placed in a variable homogeneous magnetic field.
For Magnetotransport and Hall-resistivity measurements the magnetic field is perpendicular to the layer plane. In addition to the normal Hall effect $\rho_{\mathrm{xy}} = R_{\mathrm{H}} * \mu_0 H$ with the Hall constant R_{H} depending on the charge carrier density, other contributions arise in magnetic conductors.

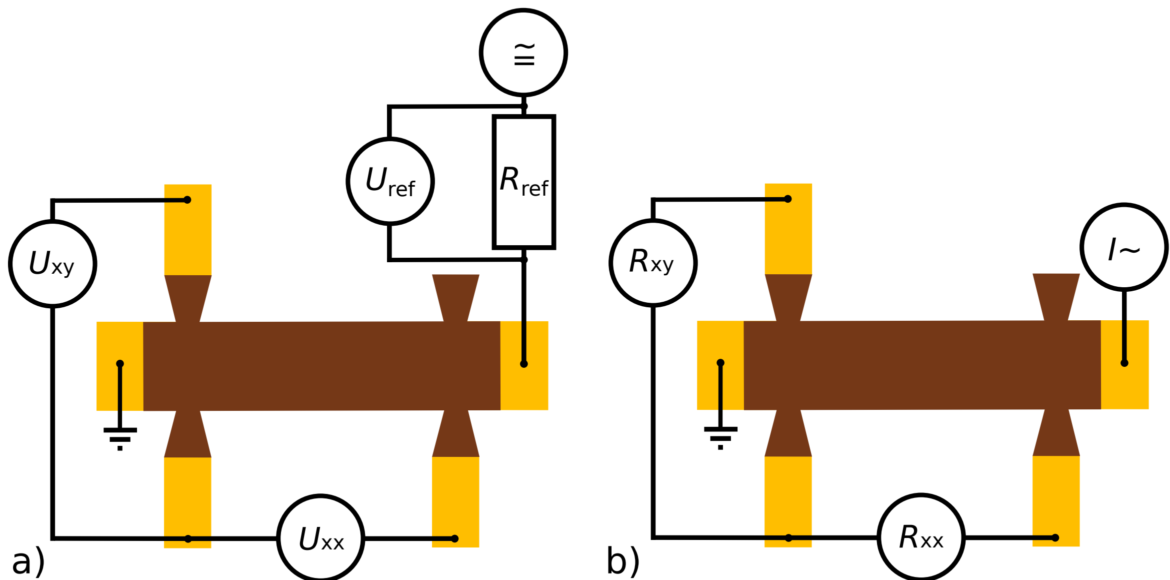

Figure 2.8: Schematic of the four point measurement setups at a Hallbar with a) an AC or DC voltage applied along a reference resistor R_{ref} and the Hallbar and measurement of the voltage drops U or b) a resistance bridge as constant AC current source and for direct measurement of the resistances R.

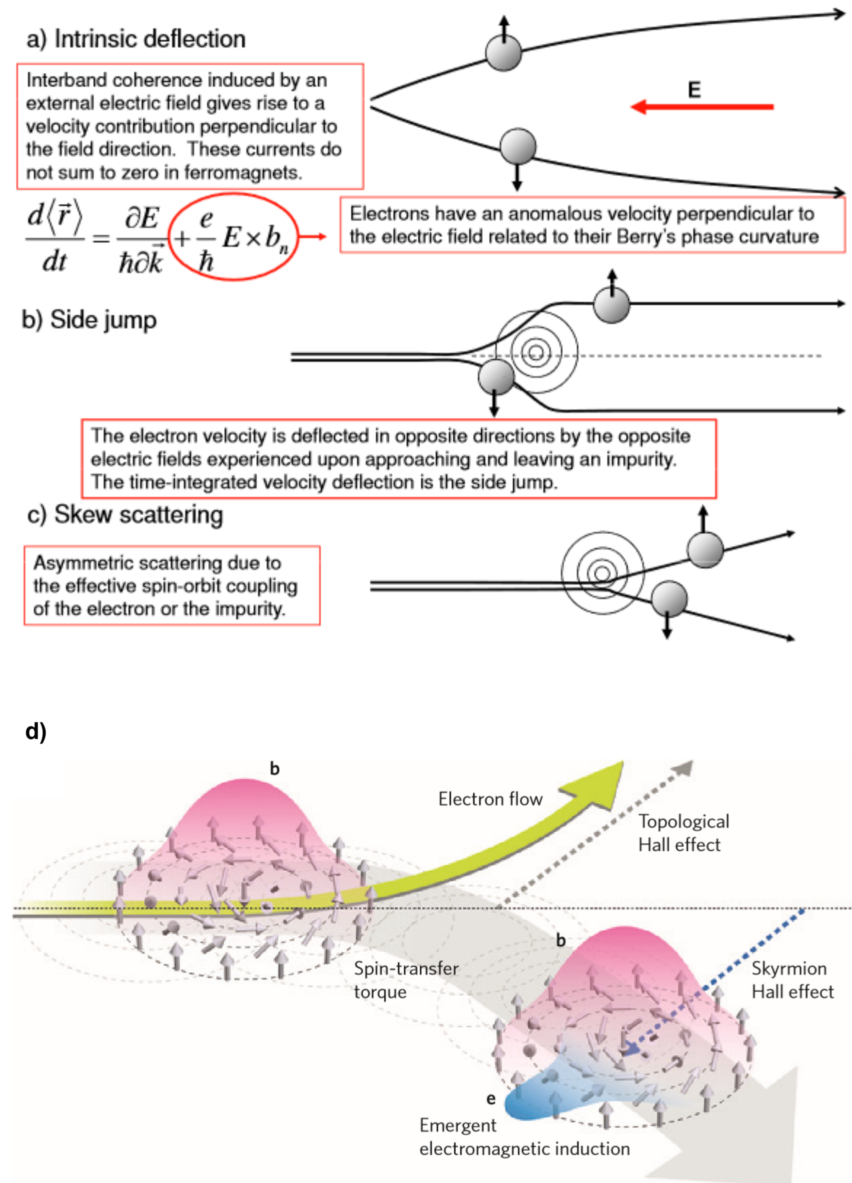

Figure 2.9: a) to c) Schematic of the three main contributions to the AHE.
d) Schematic of the Topological and Skyrmion Hall effect.
Reprinted figure a) to c) with permission from [Naoto Nagaosa, Jairo Sinova, Shigeki Onoda, A. H. McDonald, and N. P. Ong, Reviews of Modern Physics, 82, 1539, 2010, DOI: 10.1103/RevModPhys.82.1539] Copyright 2010 by the American Physical Society. [NSO+10]
d) reprinted by permission from Springer Nature Customer Service Centre GmbH: Springer Nature, Nature Nanotechnology, Topological properties and dynamics of magnetic skyrmions, Naoto Nagaosa, and Yoshinori Tokura, 2013. [NT13]

The AHE can be divided in three main parts, as illustrated in Fig. 2.9 a) to c), where a simplified explanation is given. A throughout explanation can be found in the work by Nagaosa *et al.* [NSO+10].
The intrinsic contribution depends only on the band structure of the crystal, while the other terms depend on the scattering at impurities. As these terms depend not only on the external magnetic field strength but also on the magnetization and longitudinal resistivity, the behavior and separation of the different terms becomes quite complicated.
For the non-coplanar spin arrangement of the skyrmion lattice, additional phenomena arise, sketched in the following based on Nagaosa *et al.* [NT13]. Assuming a strong coupling of the conduction electrons to the local spin structure, the electron spin following the local spin direction can be interpreted as an emergent magnetic field b, as sketched in Fig. 2.9 d). The resulting Lorentz force then leads to an additional Hall contribution, the topological Hall effect. Spin-transfer torque can lead to a motion of the skyrmion, the Skyrmion Hall effect which results in an emergent electric field e with a contribution to the Hall effect opposite to the Topological Hall effect.
These set of contributions make the interpretation of the Hall effect in MnSi quite complicated and controversial, as discussed in chapter 2.3. For this reason it will not be a focus of this thesis.
Another method proposed by Yokouchi *et al.* [YKT+15] to identify the skyrmion lattice is the measurement of the PHE, as also discussed in chapter 2.3. This effect is the perpendicular manifestation of the AMR, where the magnetic field is in the layer plane, and discussed in detail in the following section.

2.4.3 Anisotropic MagnetoResistance (AMR) theory and measurement

AMR, meaning the anisotropic response of transversal and longitudinal resistivity to electric current and magnetic field direction, was proposed by Yokouchi *et al.* [YKT+15] as a tool to identify in plane skyrmions in epitaxial MnSi layers. The basic theory of this effect will be discussed in the following, based on the work of Döring, McGuire *et al.*, Hurd and especially the recent work of Rout *et al.*, which is based on Birss [Dör38, MP75, Hur74, RAM+17, Bir66].
For a ferromagnetic material the electric field vector $\boldsymbol{E}$ depends on the current density

vector $\boldsymbol{j}$ with [Dör38]

$$E_i = \sum_{j=1}^{3} \omega_{ij} j_j \ . \tag{2.16}$$

With $\boldsymbol{\beta}$ being the unit direction vector of the current, this leads to a resistivity along the current direction (longitudinal resistivity) of [Dör38]

$$\rho_{\text{xx}} = \sum_{i,j=1}^{3} \omega_{ij} \beta_i \beta_j \ , \tag{2.17}$$

where the ω_{ij} are functions depending on the unit direction vector $\boldsymbol{\alpha}$ of the magnetization. These can be expanded as [RAM+17, Bir66]

$$\omega_{ij} = a_{ij} + a_{kij}\alpha_k + a_{klij}\alpha_k\alpha_l + a_{klmij}\alpha_k\alpha_l\alpha_m + a_{klmnij}\alpha_k\alpha_l\alpha_m\alpha_n + ... \tag{2.18}$$

taking the Einstein summation into account.
What is of interest here for the magnetoresistance is the symmetric part [RAM+17, Bir66]

$$\omega_{ij} = a_{ij} + a_{klij}\alpha_k\alpha_l + a_{klmnij}\alpha_k\alpha_l\alpha_m\alpha_n + a_{klmnpqij}\alpha_k\alpha_l\alpha_m\alpha_p\alpha_q + ... \ , \tag{2.19}$$

which is even in the magnetic field and because of that is symmetric in indices of group 1 (i, j). As indices of group 2 $(k, l, m, n, p, q, ...)$ can also be interchanged freely, the value of the coefficients only depends on the number of indices in group 1 and group 2 being 1, 2 or 3, corresponding to x, y, and z [RAM+17].
The further derivation will be restricted to a 2D case (x, y-plane), adequate for a thin MnSi layer. The resistivity then simplifies to

$$\begin{aligned}\rho_{\text{xx}} =& \beta_1^2(a_{1,1} + \alpha_1^6 a_{1,1,1,1,1,1,1,1} + 6\alpha_1^5\alpha_2 a_{1,1,1,1,1,2,1,1} + \alpha_1^4 a_{1,1,1,1,1,1} + ... \\ &+2\beta_1\beta_2(a_{1,2} + \alpha_1^6 a_{1,1,1,1,1,1,1,2} + 6\alpha_1^5\alpha_2 a_{1,1,1,1,1,2,1,2} + \alpha_1^4 a_{1,1,1,1,1,2} + ... \\ &+\beta_2^2(a_{2,2} + \alpha_1^6 a_{1,1,1,1,1,1,2,2} + 6\alpha_1^5\alpha_2 a_{1,1,1,1,1,2,2,2} + \alpha_1^4 a_{1,1,1,1,2,2} + ... \ ,\end{aligned} \tag{2.20}$$

with $\boldsymbol{\alpha} = \begin{pmatrix} \cos\theta \\ \sin\theta \end{pmatrix}$ and $\boldsymbol{\beta} = \begin{pmatrix} \cos\phi \\ \sin\phi \end{pmatrix}$ where θ and ϕ are the in-plane angles between reference crystal axis and magnetic field or current direction respectively [RAM+17].

Thus the resistivity can be expressed as

$$\begin{aligned}\rho_{\mathrm{xx}} = P_{00} &+ P_{01}{*}\cos(2\theta+2\phi) + P_{11}{*}\cos(2\theta-2\phi)\\ &+P_{21}{*}\cos(4\theta+2\phi) + P_{31}{*}\cos(4\theta-2\phi)\\ &+P_{41}{*}\cos(6\theta+2\phi) + P_{51}{*}\cos(6\theta-2\phi)\\ &+P_{61}{*}\cos(2\theta) + P_{71}{*}\cos(4\theta) + P_{81}{*}\cos(6\theta) + P_{91}{*}\cos(2\phi)\\ &+P_{02}{*}\sin(2\theta+2\phi) + P_{12}{*}\sin(2\theta-2\phi)\\ &+P_{22}{*}\sin(4\theta+2\phi) + P_{32}{*}\sin(4\theta-2\phi)\\ &+P_{42}{*}\sin(6\theta+2\phi) + P_{52}{*}\sin(6\theta-2\phi)\\ &+P_{62}{*}\sin(2\theta) + P_{72}{*}\sin(4\theta) + P_{82}{*}\sin(6\theta) + P_{92}{*}\sin(2\phi)\ ,\end{aligned} \tag{2.21}$$

with the parameters P_{ow} representing sums of the a coefficients. The relative change of the longitudinal resistivity ρ_{xx} with the angles θ and ϕ is called AMR.
The derivation can also be done for the transversal resistivity ρ_{xy}, which is the so called PHE. It is just a manifestation of AMR but perpendicular to the current direction and not related to the classical Hall effect. Eq. 2.16 becomes [RAM+17]

$$\rho_{\mathrm{xy}} = \sum_{i,j=1}^{3} \omega_{ij}\beta_i^{\perp}\beta_j\ , \tag{2.22}$$

with $\boldsymbol{\beta}^{\perp} = \begin{pmatrix}-\sin\phi\\ \cos\phi\end{pmatrix}$ being the direction vector perpendicular to the current.
This results in

$$\begin{aligned}\rho_{\mathrm{xy}} = &P_{02}{*}\cos(2\theta+2\phi) - P_{12}{*}\cos(2\theta-2\phi)\\ &+P_{22}{*}\cos(4\theta+2\phi) - P_{32}{*}\cos(4\theta-2\phi)\\ &+P_{42}{*}\cos(6\theta+2\phi) - P_{52}{*}\cos(6\theta-2\phi)\\ &+P_{62}{*}\cos(2\theta)\\ &-P_{01}{*}\sin(2\theta+2\phi) + P_{11}{*}\sin(2\theta-2\phi)\\ &-P_{21}{*}\sin(4\theta+2\phi) + P_{31}{*}\sin(4\theta-2\phi)\\ &-P_{41}{*}\sin(6\theta+2\phi) + P_{51}{*}\sin(6\theta-2\phi)\\ &-P_{61}{*}\sin(2\theta)\ ,\end{aligned} \tag{2.23}$$

with the same P parameters as before, as AMR and PHE reflect the same physics. This can be further simplified by applying symmetry considerations for the crystal structure of the studied layer. A transformation matrix T that does not change the crystal must not change the value of a coefficient, meaning [MP75, Bir66]

$$a_{i,j,k,...,z} = T_{i,p}T_{j,q}T_{k,r}...T_{z,s}a_{p,q,r,...,s} \ . \tag{2.24}$$

The strength of symmetry considerations is obvious in the simple example of the mirror symmetry of a two dimensional square lattice. Matrix V for reflections at the x-axis

$$V = \begin{pmatrix} -1 & 0 \\ 0 & 1 \end{pmatrix} \tag{2.25}$$

leads to $a_{1,2} = V_{1,p}V_{2,q}a_{p,q} = -a_{1,2}$ and consequently to $a_{1,2} = 0$. The same can be applied to the reflection along the y-axis and for all coefficients. This leads to the result that only coefficients with an even number of indices equal to 1 or 2 do not vanish. Thus all $\sin(...)$ terms in Eq. 2.21 and all $\cos(...)$ terms in Eq. 2.23 vanish, which reduces the complexity quite drastically. [RAM$^+$17]
To measure AMR and PHE, a set of Hallbars produced with optical lithography, as shown in Fig. 2.10 a), with a connected current path and an angle variation of 15° between each, is used. With that design five different angles ϕ between current and reference crystal direction can be measured in parallel.
The measurement setup at the central Hallbar of Fig 2.10 a) is sketched in Fig 2.10 c). Fig. 2.10 b) shows a 4-terminal Corbino disc with the corresponding measurement setup sketched in d). Here the current is flowing radialsymmetrically from the inner contact to the outermost ring. The two rings in between are used to measure the voltage drop and the measured resistivity is equivalent to ρ_{xx} [RVK$^+$07]. As the current flows radialsymmetrically, all terms in Eq. 2.21 and Eq. 2.23 which are depending on the current direction average to zero and only the P_{61}, P_{62}, P_{71}, P_{72}, P_{81} and P_{82} terms are left and can be measured independently from the others.
All measurements are done with the sample holder in a He^4 cryostat thermally coupled to liquid helium after a wait time between each rotation step to get back to thermal equilibrium. The expected T^2 dependence of the resistivity at low temperatures and heat from the rotation friction would cause severe variations in resistivity [KOD82, UM75].

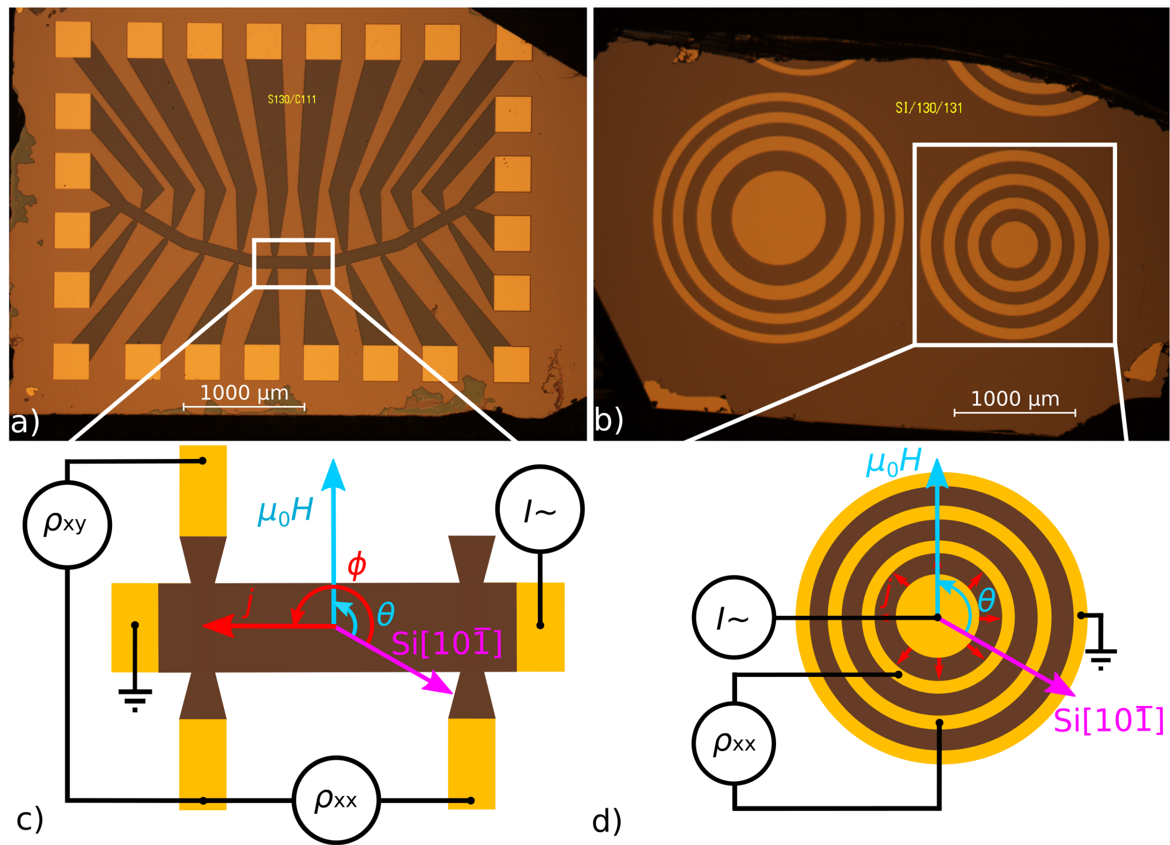

Figure 2.10: a) Optical picture of a Hallbar-set with one current path and an angle difference of 15° between each 300 µm × 100 µm Hallbar.
b) Optical picture of two Corbino-discs with gold contacts at constant radial steps of the used disc on the right.
c) Schematic of the measurement setup at the central Hallbar of a) which is aligned to the Si$[10\bar{1}]-150°$ direction. The angle θ is between magnetic field $\mu_0 H$ and reference crystal direction Si$[10\bar{1}]$ and the angle ϕ between current j and reference crystal direction Si$[10\bar{1}]$
d) Sketch of the measurement at the Corbino-disc of b) with the angle θ between magnetic field $\mu_0 H$ and reference crystal direction Si$[10\bar{1}]$ and radialsymmetric current flow.

The sample is placed in a constant magnetic field $\mu_0 H$ and rotated with a step motor to change the angle θ between magnetic field and reference crystal direction Si[10$\bar{1}$]. The head of the rotating sample holder used is shown in Fig. 2.11 a) with the worm rotated by the step motor and the wheel, in which the chipcarrier with the sample gets mounted. To determine the absolute angle and relative angle change a Hallsensor is placed on the wheel. Fig. 2.11 b) shows the Hall-voltage at the Hallsensor versus the stepnumber together with a sinusoidal fit, from which one can get an angle change of about 0.75° per stepmotor step. Such a fit is done for each rotation measurement.

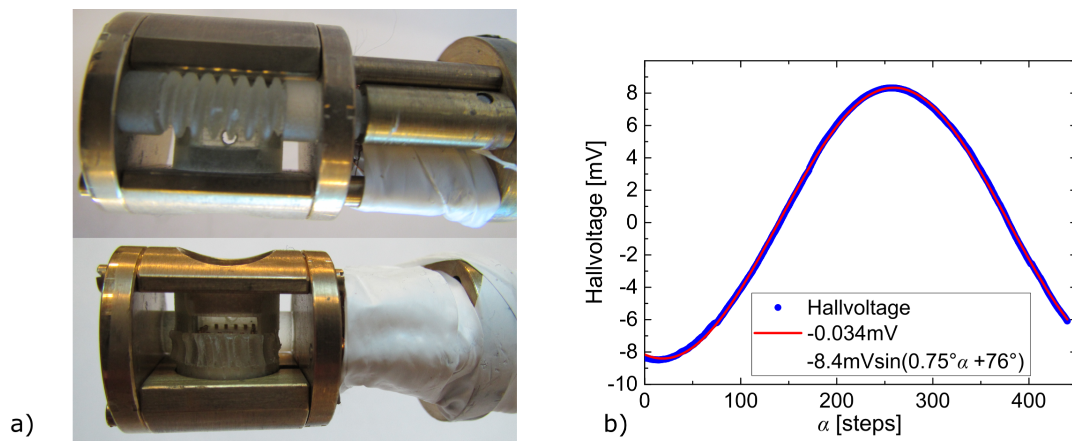

Figure 2.11: a) Front and back-view on the head of the rotating sample holder. b) Hall-voltage at the Hallsensor depending on number of stepmotor steps at $\mu_0 H = 2$ T with sinusoidal fit.

3 Epitaxial growth and structural characterization of MnSi

Independent of the interest in the rather exotic magnetic phase diagram of single crystal MnSi, explained in detail in the previous chapter, the first interest in MnSi was arising from the formation of metallic silicides on silicon, as a way to contact the silicon. Here amorphous Mn layers were deposited on Si substrates and annealed until MnSi layers are formed, the so called Solid Phase Epitaxy (SPE). [SPT73, ET82]
Also the rather exotic magnetic phase diagram, discussed in the previous chapter, was of further interest, especially how the boundaries of the different regions could be influenced by applying high pressure, which was demonstrated to decrease the critical temperature down to zero at a critical pressure of $p_\mathrm{c} = 14.6$ kbar. [BVJW75, TFL90, PMJL97, TPSF97]
Combining the early findings of MnSi formation on Si substrates with the pressure dependence of the phase diagram also makes the epitaxial growth on Si(111) interesting as it leads to epitaxial strain in the MnSi lattice-mismatched layer, which could influence the magnetic phases similar to the way extrinsic pressure does [KKM+10].
In the following section the growth process of MnSi on Si(111) will be discussed together with means to analyze the structural properties. Afterwards the occurrence of twin domains in the material will be described followed by steps to suppress them.

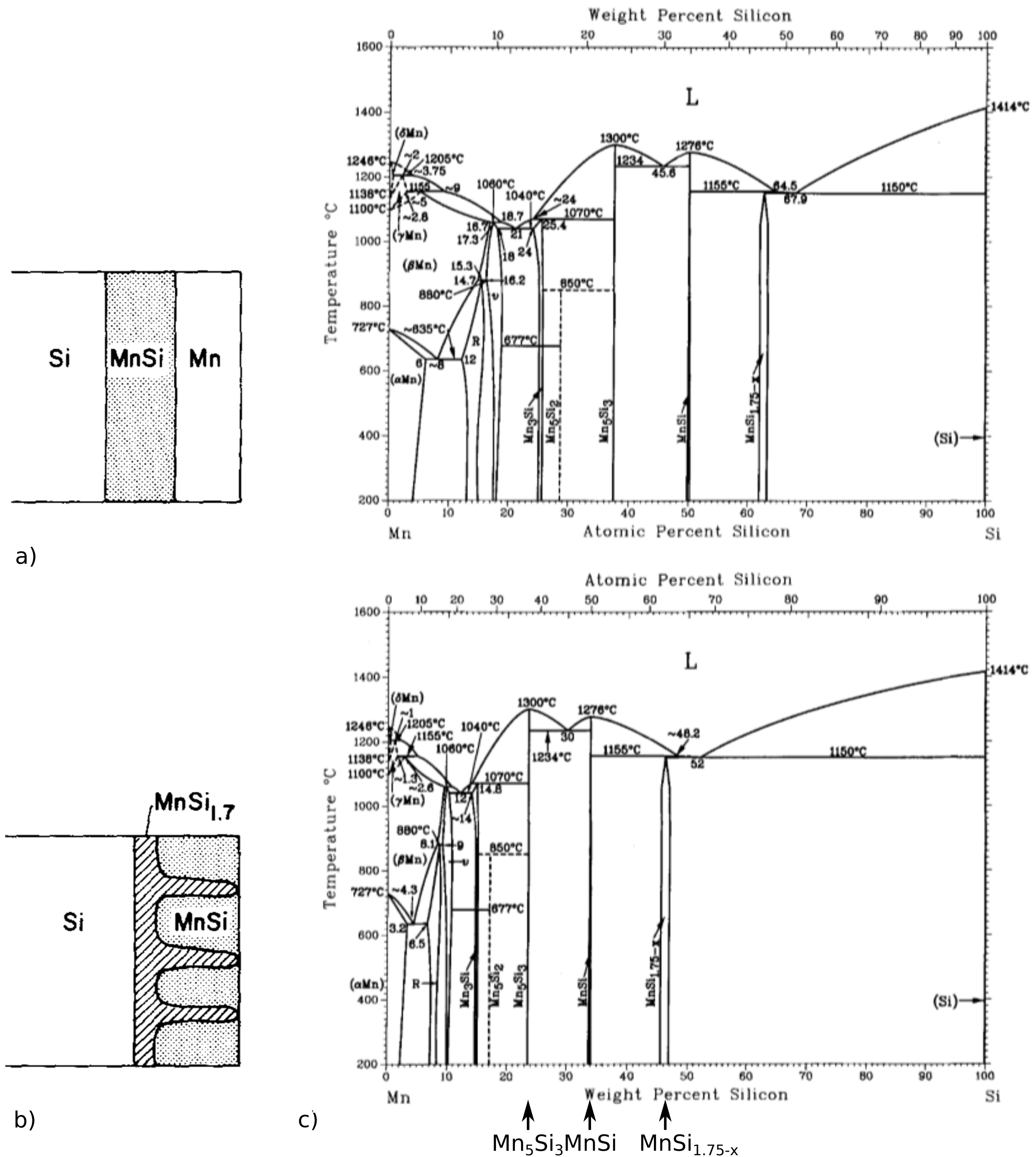

Figure 3.1: Schematic depiction of the formation of a) MnSi and b) $MnSi_{1.7}$ by SPE. c) Mn-Si equilibrium diagram with the different stable phases depending on temperature and atomic percentage of Si.
a) and b) reprinted from Formation and Schottky behavior of manganese silicides on n-type silicon, M. Eizenberg and K. N. Tu, Journal of Applied Physics, 53, 6885, 1982, with the permission of AIP Publishing. [ET82]
c) reprinted by permission from Springer Nature Customer Service Centre GmbH: Springer Nature, Journal of Phase Equilibria, The Mn-Si (Manganese-Silicon) system, A. B. Gokhale, R. Abbaschian, 1990. With additional labels for the important stable phases in c). [GA90]

3.1 Historical growth process review

For the first realization of MnSi layers on Si(111) and Si(100), amorphous Mn was deposited and annealed [SPT73, ET82]. The annealing was monitored by ion-backscattering to get the depth depended Mn/Si ratio and the exact phase of Mn_xSi_y was determined by XRD. On both substrate orientations the MnSi formation started at about 400°C with the suggested formation mechanism depicted in Fig. 3.1 a), where the reaction of Mn and Si, forming MnSi, happens below the actual surface. Increasing the annealing temperature further resulted in the formation of $MnSi_{1.7}$ patches as depicted in Fig. 3.1 b).
This highlights one of the possible problems occurring during MnSi growth, the formation of nonstoichiometric phases. Fig. 3.1 c) shows the Mn-Si equilibrium diagram with different stable phases. Here the most problematic ones for MnSi growth are Mn_5Si_3, if an excess of Mn is available during the formation, and $MnSi_{1.75-x}$, called Higher Manganese Silicide (HMS), where a deficit of Mn occurs. The aforementioned $MnSi_{1.7}$ belongs to this group of HMS.
A lot of studies of Mn deposition on Si(111) substrates with 7×7 surface reconstruction and subsequent annealing can be found in the literature with both island (Volmer-Weber) and layer plus island (Stranski-Krastanov) growth modes proposed [EGN96, SAA+97, NOMH99, ZTTF02, KTH+04, CDS+05, SMM+05, HIKT08, HKT09, HGZJ09, SIF+09, KKM+10, MBC+10, ZL11, GKS+12].
The studies differ in how much Mn is deposited, how long it is annealed, and at which temperature it is annealed. These parameters seem to be the most important for growth optimization leading to an epitaxial stoichiometric MnSi layer on Si(111).
Fig. 3.2 a)-e) schematically shows the layer formation proposed by Zou *et al.* [ZL11] for annealing an amorphous Mn layer on a $Si(111) - 7 \times 7$ substrate. The reaction starts at substrate defects and tabular MnSi islands form. These become a closed film over time, except for some holes. Possible explanations for the holes are the island growth mode, the diffusion of Si atoms from the substrate to form MnSi, or a strain relief. Fig. 3.2 f) shows a topview on the surface cells of Si and right handed MnSi, which are obviously quite different in size as the cubic lattice constant of MnSi $a_{\text{MnSi}} = 4.5603$Å [JR91] is about 16% smaller than the one for Si with $a_{\text{Si}} = 5.4310$Å [MNT16].
For MnSi islands on Si(111) Zhang *et al.* [ZTTF02] showed an orientation of Si(111) $\|$MnSi(111) and Si$[\bar{1}01]$ $\|$MnSi$[\bar{1}2\bar{1}]$. This corresponds to, as depicted in

Fig. 3.2 f) and shown by Kumar *et al.* [KTH$^+$04], the layer growth of MnSi on Si(111) with an azimuthal rotation of 30° reducing the misfit from $f = 19\%$ to $f = 3.1\%$. The reduction of f can be calculated by

$$f = \frac{\cos(30°)\sqrt{2}a_{\mathrm{Si}} - \sqrt{2}a_{\mathrm{MnSi}}}{\sqrt{2}a_{\mathrm{MnSi}}} \tag{3.1}$$

according to Herman *et al.* [HRS04] based on [Mat75, Nab79].

Zou *et al.* [ZL11] proposed that the annealing temperature is a important parameter for the growth mode, as they observed island formation by successively increasing the temperature, probably as a result of diffusion of the Mn and Si atoms.
Other proposed growth methods are codeposition of Mn and Si at room temperature and subsequent annealing, as well as sandwich structures. The later is a subsequent deposition of Mn and Si layers at room temperature followed by annealing. This methods are leading to more homogeneous and smoother surfaces than pure Mn deposition as Si atoms are mainly supplied by deposition reducing the holes caused by Si diffusion from the substrate. [MCN$^+$06, HKT09]
Later Karhu *et al.* [KKR$^+$11] presented a new method leading to significant improvements in reducing the surface roughness in comparison to their own samples produced by SPE. For this they use the previously described method of an amorphous Mn layer and subsequent annealing to form a MnSi film as a seed layer and afterwards codeposit Mn and Si for the actual layer growth. This method was used as a starting point for the work by Pohl [Poh13] and this work. In the following section the development of the growth process and the influence of different parameters on it will be described in detail.

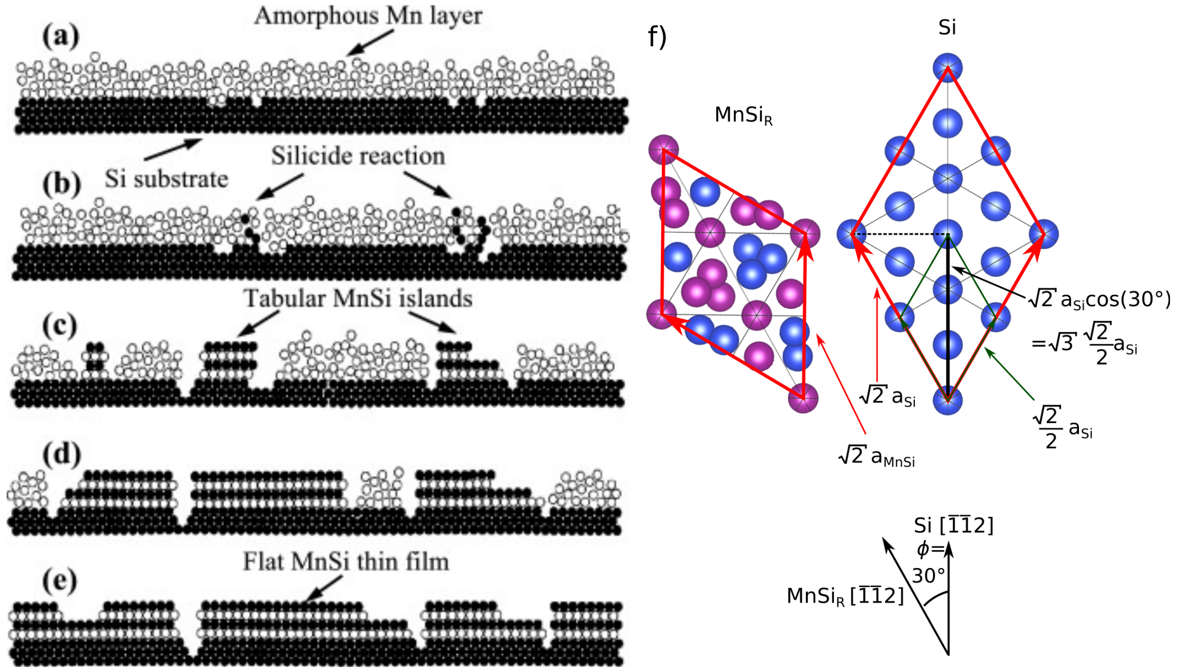

Figure 3.2: a) to e) Schematic depiction of the formation of MnSi layers by annealing amorphous Mn layers on Si substrates.
f) Surface cell in red of right handed MnSi on the left and red and green of Si on the right with Si atoms in blue and Mn atoms in purple. The different length scales that lead to a reduction of misfit by the 30° orientation are labeled with arrows in corresponding colors.
a) to e) reprinted from Physics Letters A, 375(4), Zhi-Quiang Zou and Wei-Cong Li, Two-dimensional fractal-like growth on semiconductors: The formation of continuous manganese monosilicide ultrathin films on Si(111), pages 849-854, 2011, with permission from Elsevier. [ZL11]
f) reprinted with additional labels and unit cell from M. Trabel, N. V. Tarakina, C. Pohl, J. A. Constantino, C. Gould, K. Brunner, and L. W. Molenkamp, Twin domains in epitaxial thin MnSi layers on Si(111), Journal of Applied Physics, 121(24):245310, 2017, https://aip.scitation.org/doi/abs/10.1063/1.4990284?journalCode=jap, where pictures of the crystal structures have been produced with Vesta 3 [MI11]. [TTP+17]

3.2 Growth process overview

In the beginning of this work a series of MnSi layers with varying thickness were grown following closely the preceding work by Pohl and Karhu *et al.* [Poh13, KKR+11]. During the course of this work modifications were done to the MBE chamber, which is shown in Fig. 3.3. The most influential ones are the replacement of the substrate heater in the main chamber and the installation of a silicon sublimation source, both influencing the actual temperature at the substrate surface in comparison to the temperature measured by a thermocouple at the backside of the substrate.
As the discussed changes at the chamber led to a change in substrate temperature, recalibration of the growth process had to be done and the growth process was examined in more detail. In the following sections this will be described in detail, starting with the substrate preparation followed by the MnSi seed layer and the actual layer growth finished with a protecting amorphous Si cap layer.

3.2.1 Substrate preparation

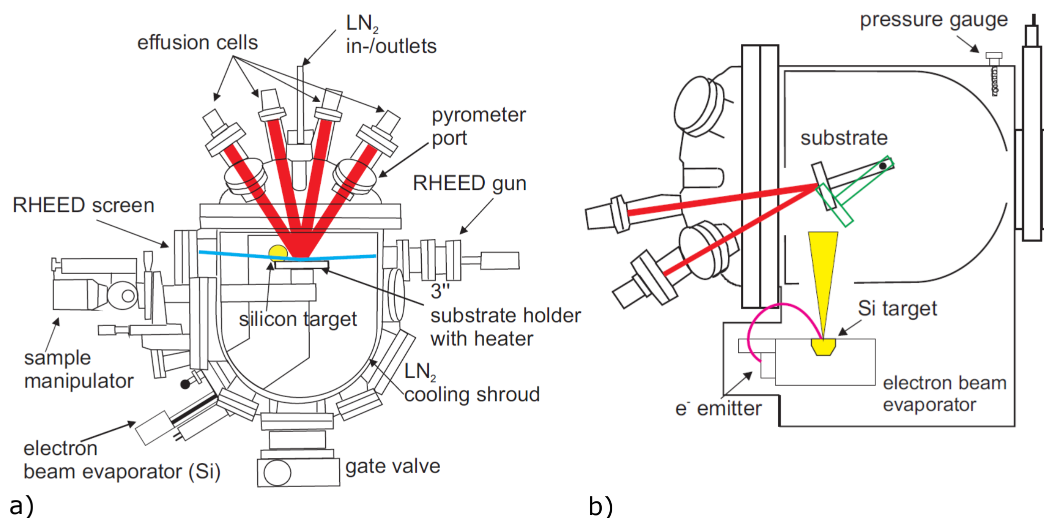

Figure 3.3: a) Top-view and b) side-view on the MBE chamber depicting the flux from the effusion cells and the electron beam evaporator on the sample. Additionally possible in-situ analysis by RHEED and pyrometer measurements is shown.
Reprinted with permission from Christoph Pohl, Silicon Based MBE of Manganese-Silicide and Silicon-Suboxide, Dissertation, urn:nbn:de:bvb:20-opus-83757, Julius-Maximilians-Universität Würzburg, 2013. [Poh13]

The standard substrates used during this work are intrinsic high resistivity (> 10000 Ωcm) 3 " Si(111) substrates, polished on the front side and etched on the back side.
In the beginning of this work the Si substrates were prepared by removing the native oxide and forming a H-passivation with a 30 s dip in undiluted HF (50%) followed by the immediate transfer in a N_2 atmosphere or the MBE system to prevent contamination and reoxidization. The MBE system has a prechamber (not shown), which is equipped with a heating station. There a preheating step of 30 min at 400°C to remove water or other residuals on the passivated surface is done.
Then the wafer is transferred into the main chamber, shown in Fig. 3.3, a detailed description of the MBE setup can by found in the work of Pohl [Poh13]. The substrate is loaded onto the substrate holder equipped with a heater, as shown in Fig. 3.3 a). There the substrate is heated to 850°C to remove the H-passivation and after 10 min cooled to 750°C, where a buffer layer of about 32 nm Si is deposited with the electron beam evaporator shown in Fig. 3.3. Because of the chamber design and the simultaneous growth with the electron beam evaporator for Si and an effusion cell for Mn, as depicted in Fig. 3.3 b), the substrate surface is at the edge of the beam profile of the electron beam evaporator which leads to a low Si deposition rate. With a constant beam profile and Si target, the Si flux is low (about 0.2Å/s) but held constant by regulation with a Sentinel III control unit. To achieve the desired Mn-Si ratio, the Si flux is held constant and the Mn cell temperature and with that the Mn flux is varied.
RHEED, as explained in section 2.2.1, is used to monitor the complete process in-situ. During the removal of the H-passivation additional spots next to the Si streaks appear in the RHEED picture. While cooling of the substrate to 750°C the Si(111)-7×7 reconstruction appears, the aforementioned additional spots are however still visible. These additional spots disappear during the buffer growth indicating that the surface smoothens by the buffer. One possibility to explain the rough surface would be surface defects by the etching process.
To exclude the dilution of HF being responsible, etching with HF (50%) 1:200 diluted with water was tried. The RHEED picture of a substrate prepared by that is shown in Fig. 3.4 a), together with a picture after a rotation of a few degree. This is the case for all following double RHEED pictures.

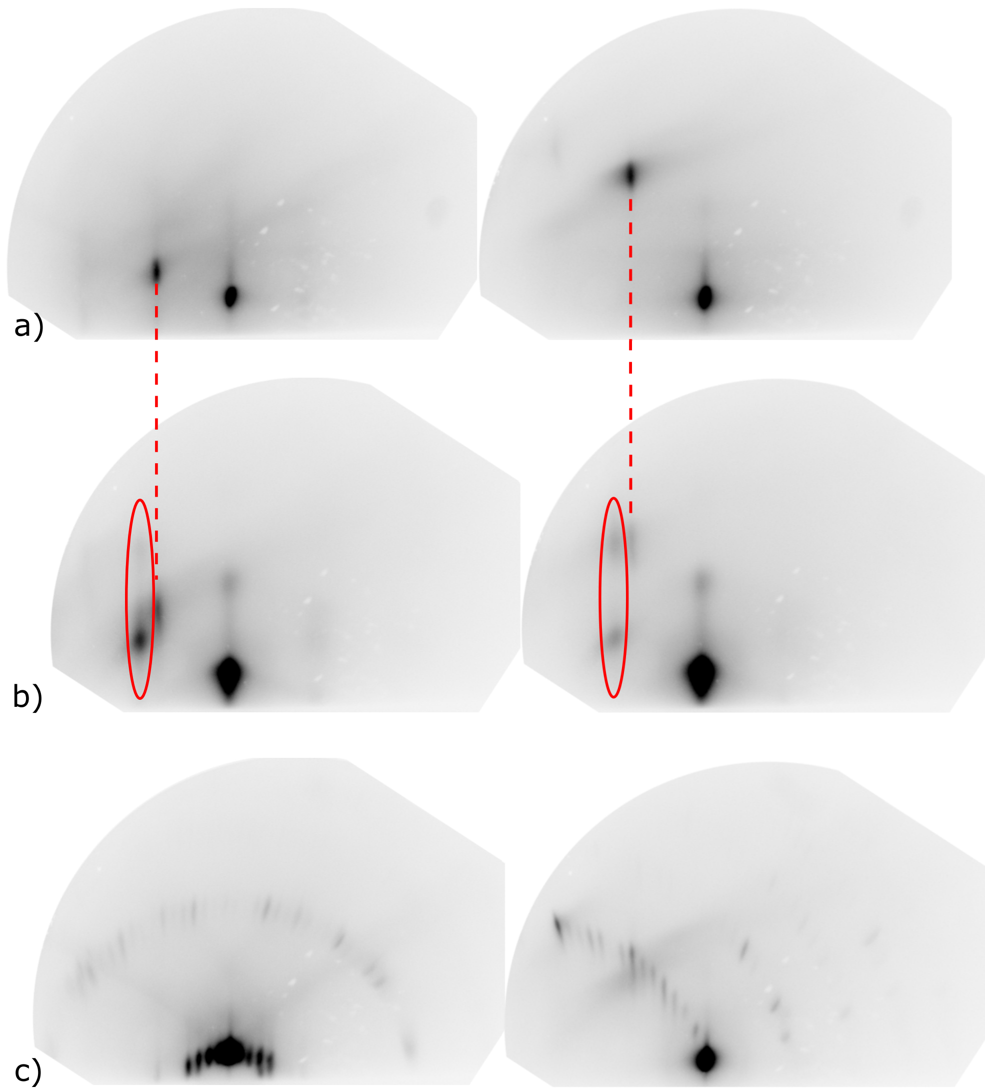

Figure 3.4: a) RHEED of a HF etched Si(111) substrate before deoxidization with an Si streak marked with the dashed line.
b) At 850°C with an Si streak marked with the dashed line and an β-SiC spot marked by the ellipses.
c) 7×7 reconstruction after deposition of a Si buffer layer.

Even here the additional spots appear during passivation removal shown in Fig. 3.4 b). The Si streaks are indicated by the dashed lines and the additional spots marked by the ellipses. Fig. 3.4 c) shows the RHEED pattern after buffer growth with a 7×7 reconstruction and no additional spots indicating a well ordered clean surface. Therefore the concentration of HF seems unlikely to be the reason for the spots.
In literature, these additional spots are interpreted as β-SiC as shown by Becker *et al.* [BLM94], so a substrate preparation method designed to prevent carbon contamination was tried as described by Eberl [Ebe90]. Here the untreated Si substrate is loaded in the MBE system where it undergoes the same preheating process. Then it is loaded into the chamber and heated to 500°C where it stays overnight for at least 15 h. During that time carbon is supposed to evaporate, while the oxide layer is protecting the substrate against diffusion of the carbon. Then it is heated above 800°C within 15 min where it stays for 5 min, which leads to the deoxidization, before it is cooled to 750°C for the buffer growth.
Fig. 3.5 a) shows a practically amorphous surface after 22 h at 500°C, indicating that the oxide layer is still intact. This is even the case after annealing the sample to 800°C as shown in Fig. 3.5 b). Fig. 3.5 c) shows the substrate at 900°C with Si 1×1 streaks but no indication of β-SiC. During cooling, the 7×7 reconstruction appears between 850°C and 830°C with the RHEED picture at the latter temperature shown in Fig. 3.5 d). This shows a well ordered clean surface even without the buffer layer, which nevertheless is grown to further increase crystal quality of the surface. In conclusion the preparation of pristine Si(111) substrate at 400°C for 30 min followed by 500°C for more than 15 h and then 5 min above 800°C leads to a reduction of carbon defects at the interface. The substrates surface is now prepared for the further growth process of MnSi layers, as confirmed by the high quality RHEED 7×7 pattern, especially for the deposition of a Mn wetting layer which will be discussed in the following section.

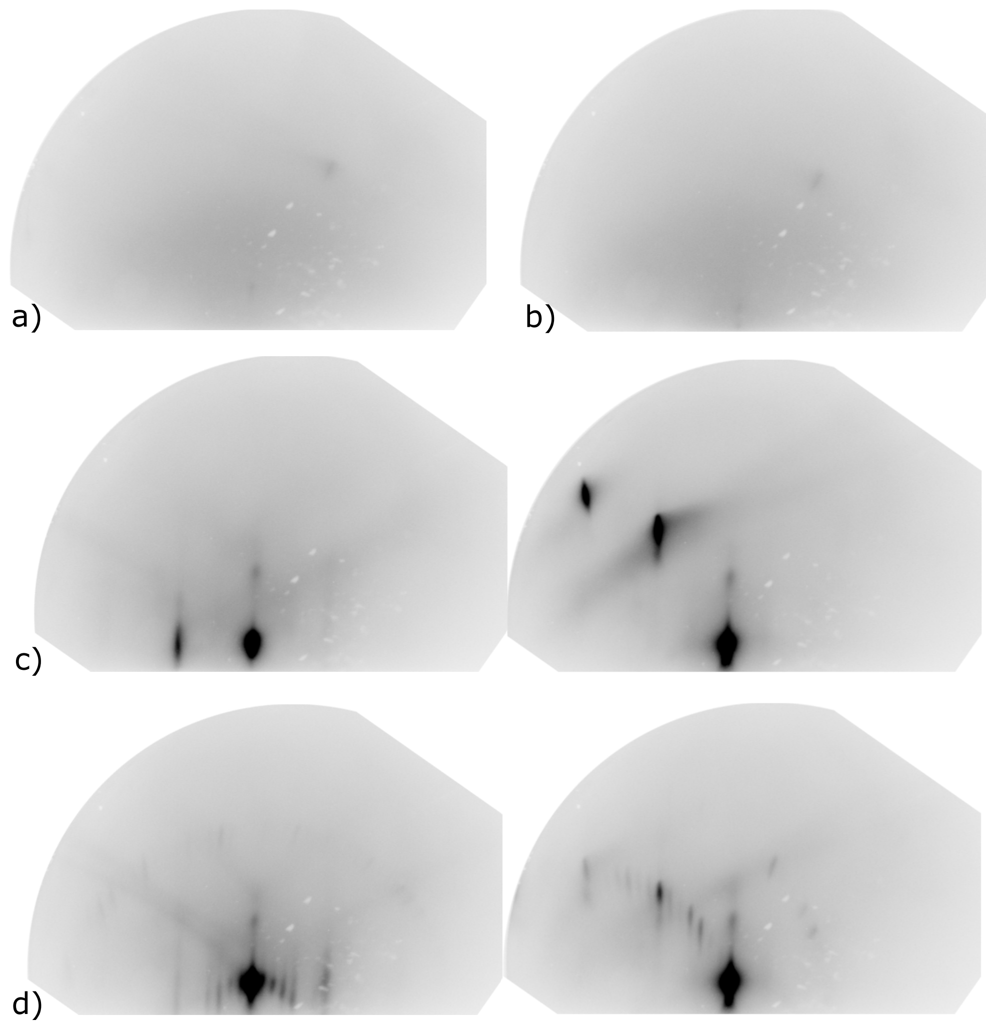

Figure 3.5: RHEED of a oxidized Si(111) substrate before deoxidization at 500°C in a) and at 800°C in b).
c) At 900°C with Si streaks.
d) 7×7 reconstruction after cooling to 830°C.

3.2.2 Seed layer

As discussed in the first section of this chapter, a MnSi seed layer was shown to be the best starting point for MnSi growth by co-deposition. For that Mn is deposited on the substrate below 80°C to build an amorphous Mn layer with a thickness above 1 MonoLayer (ML) of Mn [Poh13]. How the Mn flux rate and with that the necessary deposition time can be determined is described in the following chapter. If the layers are to thin this can lead to islands instead of a closed layer as described in section 3.1.

Fig. 3.6 a) shows RHEED of the 7×7 reconstruction of the buffer layer before deposition of the Mn wetting layer at about 70°C. Fig. 3.6 b) shows a RHEED picture of the amorphous Mn layer of about 7 ML, with only a weak specular spot visible. Then the substrate is heated to the desired growth temperature of about 290°C within 20 min. The determination of the growth temperature is described in the next section. At about 100°C the RHEED picture starts to change leading to the unreconstructed 1×1 displayed in Fig. 3.6 c) at about 200°C. At the growth temperature shown in Fig. 3.6 d) even a higher order streak is clearly visible as indicated by the red circle. In summary the long and thin streaks and the visibility of a higher order reflection indicate a well ordered flat MnSi surface, which is a good starting condition for the epitaxial MnSi layer growth discussed in the next section.

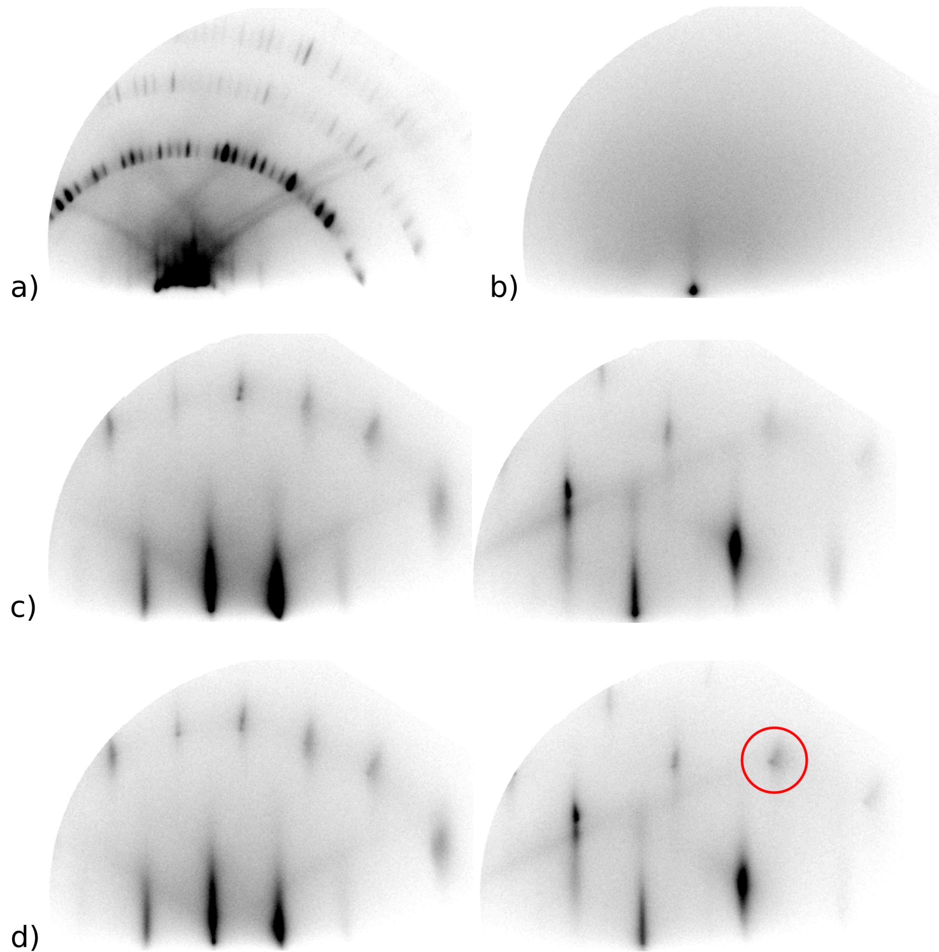

Figure 3.6: RHEED of the 7×7 reconstruction of the buffer layer at $T_{\mathrm{Sub}} \approx 70°\mathrm{C}$ in a) and after deposition of about 7 ML of Mn in b).
c) MnSi seed layer at about 200°C.
d) MnSi seed layer before layer growth at 290°C.
Lightness and contrast are adjusted for better visibility in all pictures.

3.2.3 MnSi layer and cap

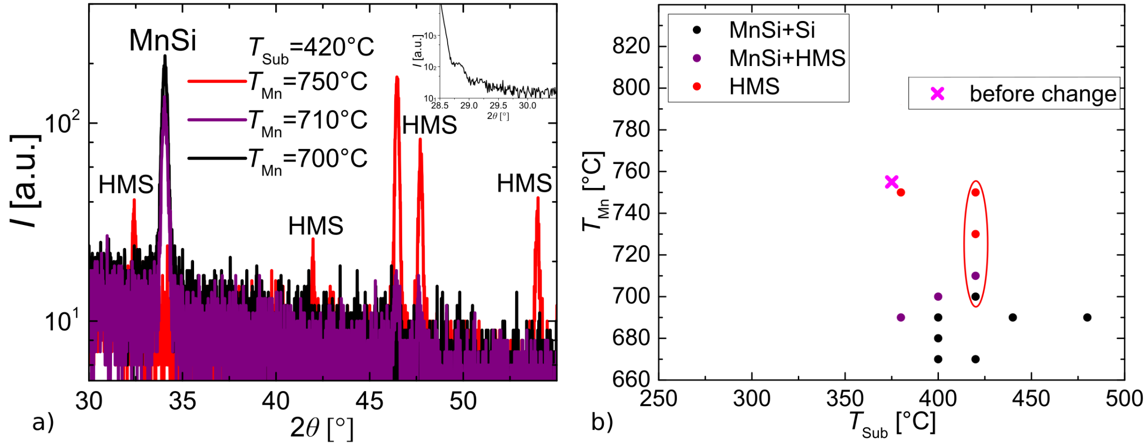

Figure 3.7: a) $2\theta - \theta$-scans for a selected sets of samples with a constant substrate temperature of $T_{\mathrm{Sub}} = 420°\mathrm{C}$ and varying Mn cell temperature T_{Mn}
b) Chemical composition overview for a calibration set depending on substrate temperature T_{Sub} and Mn evaporation cell temperature T_{Mn}. The red ellipse indicates the sample series shown in a). The cross indicates the sample series before the modifications to the chamber discussed in the text.

As mentioned in the introduction to this section, the change of the substrate heater in the main chamber and the installation of a silicon sublimation source led to a change in the relation between measured substrate temperature and actual temperature at the substrate surface. This makes recalibration necessary and a set of samples with different substrate temperatures and Mn fluxes was grown. The samples from this set are supposed to have a layer thickness of about 26 nm and an amorphous Si cap layer of about 13 nm deposited at room temperature to protect the layer against oxidization. XRD measurements as described in chapter 2.2.2 are used for identification of the appearing manganese silicide phases by matching the positions of reflexes to published data on the Mn-Si equilibrium phase diagram. The lattice parameter calculated with the Bragg relation (Eq. 2.3) is also compared to the value of a single crystal for strain determination, which will be discussed in more detail later.
The first set of samples discussed in the following is supposed to illustrate the effects of choosing an insufficient start temperature for both, the Mn cell and the substrate. As shown in Fig. 3.7 a) the first set is grown at a constant substrate temperature

of $T_{Sub} = 420°C$ with varying Mn-Si ratio by varying the Mn cell temperature. For $T_{Mn} = 750°C$ all peaks are identified as HMS reflections [ANZR12], as shown by the red curve in Fig. 3.2 b). Decreasing the Mn cell temperature to $T_{Mn} = 710°C$ leads to a mixture of MnSi and HMS as shown by the purple curve. This means a decrease in Mn flux leads to a decrease of the Si rich HMS phase, which at first seems counterintuitive. Decreasing it even further to $T_{Mn} = 700°C$ lets the HMS phase disappear completely and leaves MnSi as the only measurable phase. With a Bragg condition of the (111) reflection at $2\theta = 34.05°$ the MnSi seems almost completely relaxed with a lattice constant reduction of $< 0.1\%$ compared to the bulk parameter [JR91].
In addition thickness fringes from interference appear at the 111 Si reflection at 28.44°, as shown in the inset. These indicate an additional Si layer with a homogeneous thickness on top of the MnSi seed layer, as the Si substrate itself does not lead to thickness fringes. The RHEED picture of the layer after growth, shown in Fig. 3.8, also supports the interpretation of the crystal structure as a simultaneous occurrence of a MnSi and Si surface. The sample shown is grown with $T_{Sub} = 440°C$ and $T_{Mn} = 690°C$, as the RHEED picture is even more pronounced for the higher substrate temperatures. The RHEED picture shows long thin streaks without spots indicating a smooth, well ordered surface. But comparing this with the MnSi RHEED shown in Fig. 3.6 d), one sees additional streaks (green arrows) between the MnSi streaks(red arrows) and the higher order streaks also do not correspond to the ones observed before. The position and number of the additional streaks seems to correspond to the Si(111) 7×7 reconstruction. This becomes especially obvious in Fig. 3.8 b). The RHEED of the MnSi seed layer at $T_{Sub} = 300°C$ is overlaid with the RHEED of the Si buffer layer, which resembles the RHEED in 3.8 a) and supports the interpretation as a simultaneous occurrence of MnSi and Si surfaces.
To further investigate the layer structure, SEM and EDX measurements were done. For the SEM images a SE2 detector is used, which shows regions of different composition. This stems from back scattered electrons as their yield has a high atomic number dependency [GNJ+08].
The SEM picture is shown in Fig. 3.8 c) together with spots indicating the regions of EDX measurements which are used to analyze Si and Mn content. As expected there is Si with an atomic percentage above 97% present at both positions, because substrate, buffer and cap layer consist of Si. The cap layer is an amorphous Si layer deposited at room temperature to protect the MnSi layer against oxidization.

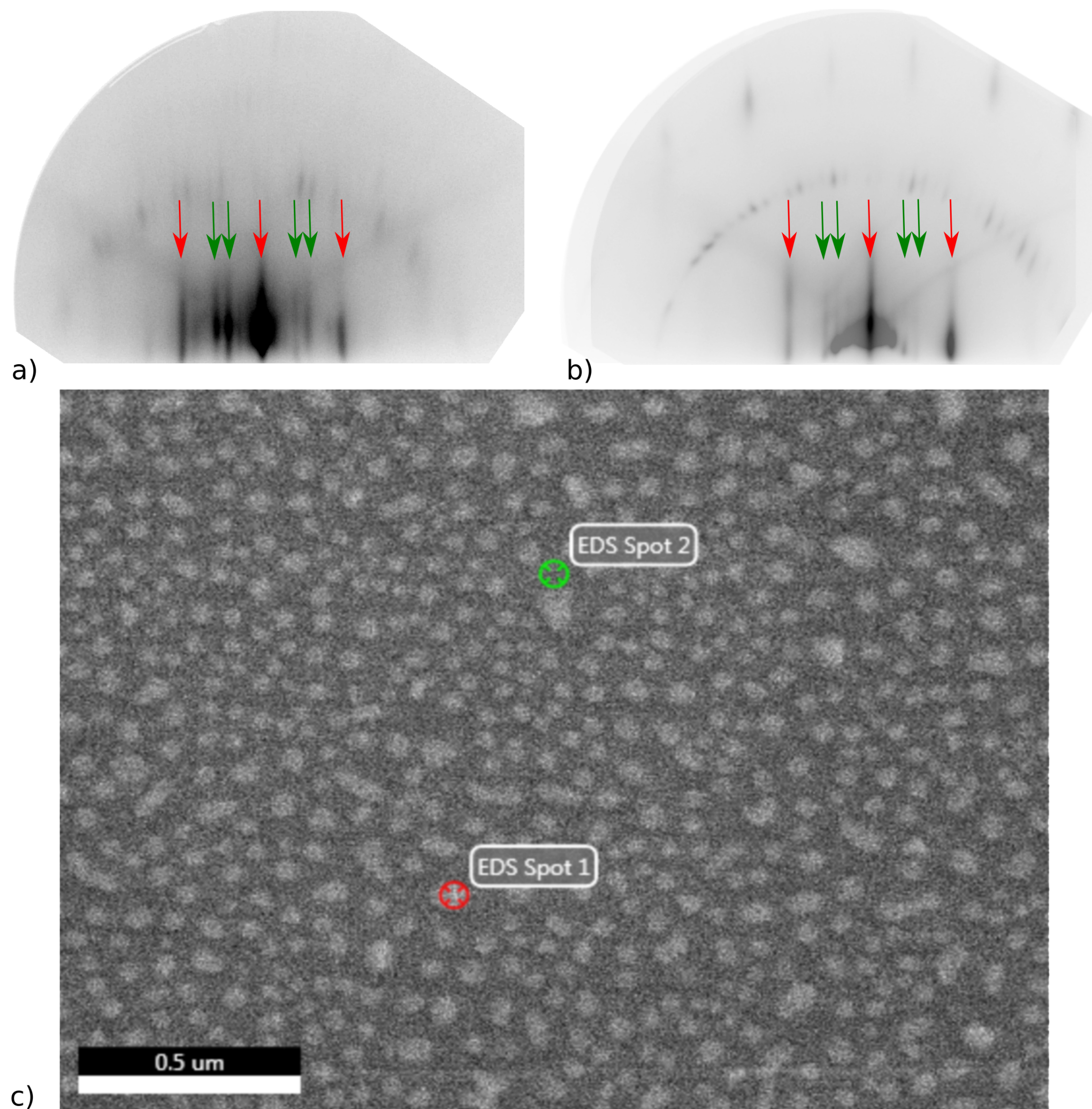

Figure 3.8: a) RHEED of the MnSi layer with $T_{\mathrm{Sub}} = 440°\mathrm{C}$ and $T_{\mathrm{Mn}} = 690°\mathrm{C}$ shown in Fig. 3.7 b) with the positions of MnSi streaks marked by the red arrows and the positions of the best visible other streaks marked with green arrows. Lightness and contrast adjusted for better visibility.
b) Overlay of the RHEED pictures from seed and buffer layer as shown before with the same arrows as in a).
c) SEM measurement of the same sample with EDX measurements at the positions indicated with a Mn atomic percent of 2.4% at spot 1 and 0.1% at spot 2 [Bor].

Mn is detected with an atomic percent of 2.4% for the bright region at spot 1 and only 0.1% for the dark region at spot 2. Together with the RHEED pictures this leads to the conclusion that in this high T_{Sub} and low T_{Mn} region MnSi islands are growing incorporated in a well order Si lattice. Fig. 3.7 b) shows the chemical composition of the discussed series encircled in red, similar samples and the measured temperature (cross) of the sample series before the modifications to the chamber to illustrate the change in conditions.
The counterintuitive behavior in the aforementioned temperature region makes it obvious that both substrate temperature and Mn cell temperature have to be calibrated together to obtain a stoichiometric MnSi film. To find a start temperature for the Mn cell, calibration samples with amorphous Mn and Si layers can be grown and analyzed by XRR measurements, as described in section 2.2.3. With the layer thickness d per growth time t, the flux density [Poh13]

$$f = \frac{d \cdot \rho \cdot N_{\mathrm{A}}}{u \cdot t} , \tag{3.2}$$

with the Avogadro constant N_{A} and the density ρ and atomic weight u of the grown material, can be calculated. For Si the used values are $\rho_{\mathrm{Si}} = 2.33$ g/cm^3 and $u_{\mathrm{Si}} = 28.085$ and for Mn $\rho_{\mathrm{Mn}} = 7.44$ g/cm^3 and $u_{\mathrm{Si}} = 54.938$ [HS04, CIA17].
While the films for calibration were grown, the Si target of the electron beam evaporator had to be exchanged which led to an offset in the Mn cell temperature to match the changed Si flux for MnSi growth. From the chemical composition a shift of $\Delta T_{\mathrm{Mn}} = -30$°C is estimated and T_{Mn} is rescaled in the following.

Fig. 3.9 a) shows the XRR measurement at a calibration sample grown after the last described change. A simulation, as discussed in 2.2.3, reveals layer thicknesses of $d_{\mathrm{Si}} = 38.2$ nm and $d_{\mathrm{Mn}} = 36.1$ nm for a growth time of $t = 1800$ s and a Mn cell temperature $T_{\mathrm{Mn}} = 795$°C. The flux densities for that, calculated with Eq. 3.2, are $f_{\mathrm{Si}} = 1.06 \times 10^{14}$ cm^{-2}s^{-1} and $f_{\mathrm{Mn}} = 1.64 \times 10^{14}$ cm^{-2}s^{-1}, so a Mn/Si ratio of about 1.5. As a T_{Mn} decrease of 20°C leads to approximately half the flux density, T_{Mn} should be about 780°C for stoichiometric growth conditions [Poh13].
Taking a substrate temperature of $T_{\mathrm{Sub}} = 280$°C and a Mn cell temperature of $T_{\mathrm{Mn}} = 780$°C, as determined by calculation of the flux densities, one gets two reflections in the $2\theta - \theta$ XRD measurements, as shown in Fig. 3.9 b). The reflection at $2\theta = 34.15°$ can be identified as MnSi 111 and the one at $2\theta = 37.38°$ as Mn_5Si_3 002 [JR91, YGC$^+$04]. This shows that the determination of the MnSi growth conditions

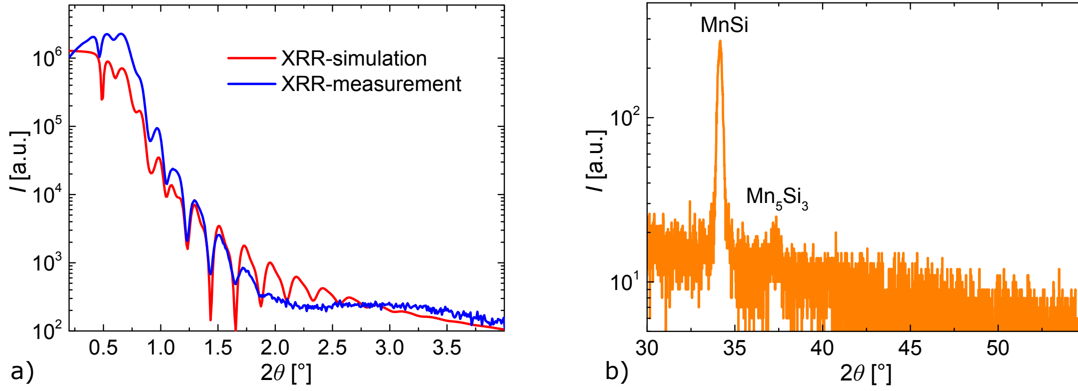

Figure 3.9: a) XRR-measurement of a calibration sample with an amorphous Mn layer and an amorphous Si cap layer with growth time $t = 1800$ s. Simulation of a 36.1 nm Mn layer with 1.3 nm roughness and a 38.2 nm cap layer of Si with 1.5 nm roughness done with [Bru].
b) $2\theta - \theta$-scan of a MnSi layer grown at $T_{\mathrm{Sub}} = 280°$ and $T_{\mathrm{Mn}} = 780°$C.

by flux densities can only be a first estimate. A broader set of samples has to be grown to identify the correct parameters for MnSi growth.
Taking a substrate temperature of $T_{\mathrm{Sub}} = 280°$C and a Mn cell temperature of $T_{\mathrm{Mn}} = 790°$C as a starting point results in two reflections in the $2\theta - \theta$ XRD measurements as shown in the orange curve in Fig. 3.10 a). The reflection at $2\theta = 34.10°$ can again be identified as MnSi 111. The lattice parameter perpendicular to the layer plane, calculated by Eq. 2.4, is about 0.2% smaller than the bulk parameter [JR91]. As mentioned in section 3.1 the MnSi grows on Si(111) with a rotation of 30° in the layer plane, which reduces the misfit from 19 % to about 3.1 %, which means the calculated lattice parameter indicates a mostly relaxed layer. For MnSi on Si(111) the lattice constant of the substrate is larger than the one of the layer. If the lattice constant of substrate and epitaxial layer do not match, the unit cell of the layer gets distorted with a increase of the in-plane lattice constant and a decrease of the out-of-plane lattice constant. A way to relax the layer is by misfit dislocations at the interface, where bonds at the interface get skipped.
The reflection at $2\theta = 37.38°$ in Fig. 3.10 a) on the other hand is again identified as Mn_5Si_3 002 with a higher volume fraction than in the sample shown in Fig. 3.9 b) estimated from the ratio of maximum intensities [YGC+04].
A higher volume of the Mn rich phase with an increase in T_{Mn} seems plausible. This

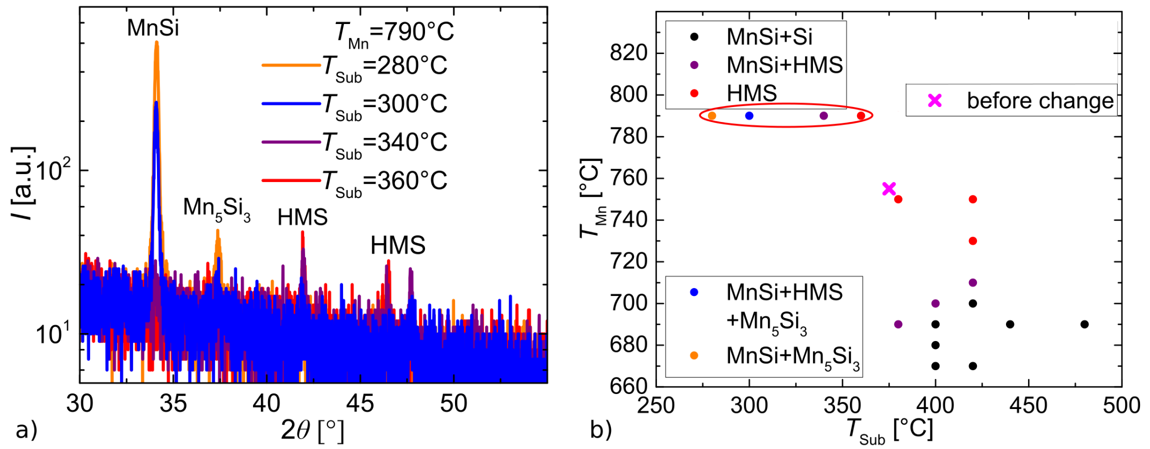

Figure 3.10: a) $2\theta - \theta$-scans for a selected sets of samples with a constant Mn cell temperature of $T_{\text{Sub}} = 790°\text{C}$ and varying substrate temperature T_{Sub} b) Chemical composition overview for a calibration set depending on substrate temperature T_{Sub} and Mn evaporation cell temperature T_{Mn}. The red ellipse indicates the sample series shown in a). The cross indicates the sample series before the modifications to the chamber discussed in the text.

can be corrected with a reduction of the Mn cell flux by decreasing the cell temperature. But also a higher substrate temperature could remove the Mn_5Si_3 phase by Mn desorption or by providing Si diffusion from the substrate.

The change by increasing the substrate temperature is displayed in Fig. 3.10 a) with a constant Mn cell temperature of $T_{\text{Mn}} = 790°\text{C}$ and an increase of T_{Sub} from 280°C to 360°C. Fig. 3.10 b) shows an overview of all samples from this calibration mentioned so far, with the discussed series encircled in red. First at $T_{\text{Sub}} = 300°\text{C}$ more reflections appear as displayed by the blue curve. While the intensities of the MnSi and Mn_5Si_3 reflections decrease with increasing substrate temperature, additional reflections addressed to the HMS phase appear at $2\theta = 41.9°$ and $2\theta = 47.7°$ [ANZR12]. Increasing the substrate temperature further to $T_{\text{Sub}} = 340°\text{C}$ leads to a complete disappearance of the Mn_5Si_3 phase and an almost complete suppression of MnSi. Instead two reflections appears at $2\theta = 42.9°$ and $2\theta = 46.5°$ that also belong to the HMS phase [ANZR12]. Increasing the substrate temperature even further to $T_{\text{Sub}} = 360°\text{C}$ leads to the HMS phase as the only measurable phase left.

From the same start temperatures of $T_{\text{Sub}} = 280°\text{C}$ and $T_{\text{Mn}} = 790°\text{C}$, lowering the

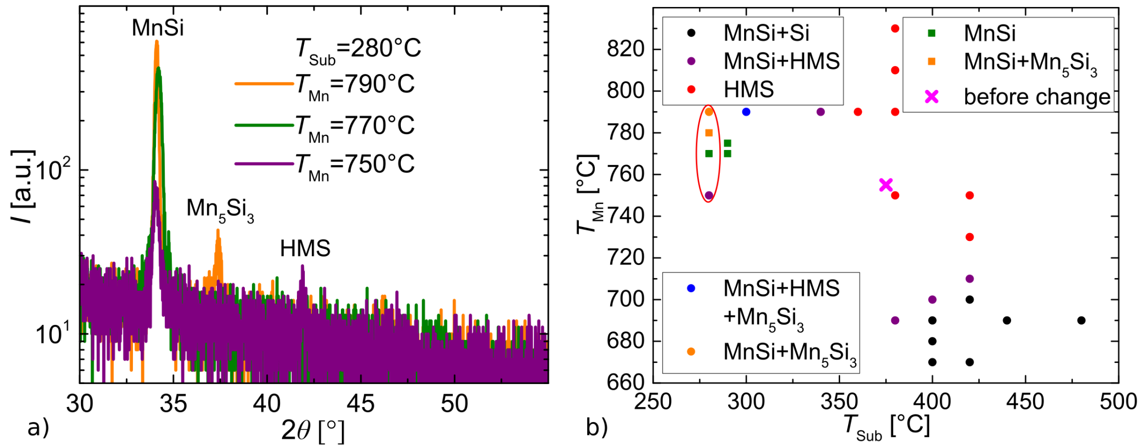

Figure 3.11: a) $2\theta - \theta$-scans for a selected sets of samples with a constant substrate temperature $T_{\text{Sub}} = 280°\text{C}$ and varying Mn cell temperature T_{Mn}.
b) Chemical composition overview for a calibration set depending on substrate temperature T_{Sub} and Mn evaporation cell temperature T_{Mn}. The red ellipse indicates the sample series shown in a). The cross indicates the sample series before the modifications to the chamber discussed in the text. The squares indicate the samples with a rescaled T_{Mn} as discussed in the test.

Mn cell temperature to $T_{\text{Mn}} = 770°\text{C}$ and the Mn flux leads to pure MnSi, as shown by the green curve in Fig. 3.11 a). Decreasing T_{Mn} further to 750°C leads back to a mixture of MnSi and the HMS phase as shown by the purple curve in Fig. 3.11 a).
Analyzing the angle of the MnSi reflections in Fig. 3.11 a) also indicates that the additional phases work as relaxation centers, as in this case a lower 2θ value means a more relaxed layer. The green curve has a reflex position of $2\theta = 34.20°$ which means a lattice spacing reduction of about 0.5 %. For the sample shown in Fig. 3.9 which is slightly away from the correct parameters the lattice spacing is reduced about 0.4% and for the orange curve with Mn excess in Fig. 3.11 a) which is further away of the correct parameters it is reduced only about 0.2%. For Si excess with the purple curve in Fig. 3.11 a) the 111 MnSi reflection is at $2\theta = 34.08°$ and with that the lattice spacing again reduced only about 0.2%. The strain relaxation in these cases probably happens at islands of the different phases. Fig. 3.11 b) shows the chemical composition of all samples from the calibration depending on Mn cell temperature T_{Mn} and substrate temperature T_{Sub}. The last discussed series is encircled in red.
Fig. 3.12 a) shows an AFM measurement of the capped 32 nm MnSi layer from the

sample series preceding the changes to the MBE chamber, described in the introduction to this section, and b) of the capped 26 nm MnSi layer grown after optimization with $T_{\mathrm{Sub}} = 290°\mathrm{C}$ and $T_{\mathrm{Mn}} = 775°\mathrm{C}$ shown in Fig. 3.11 b).

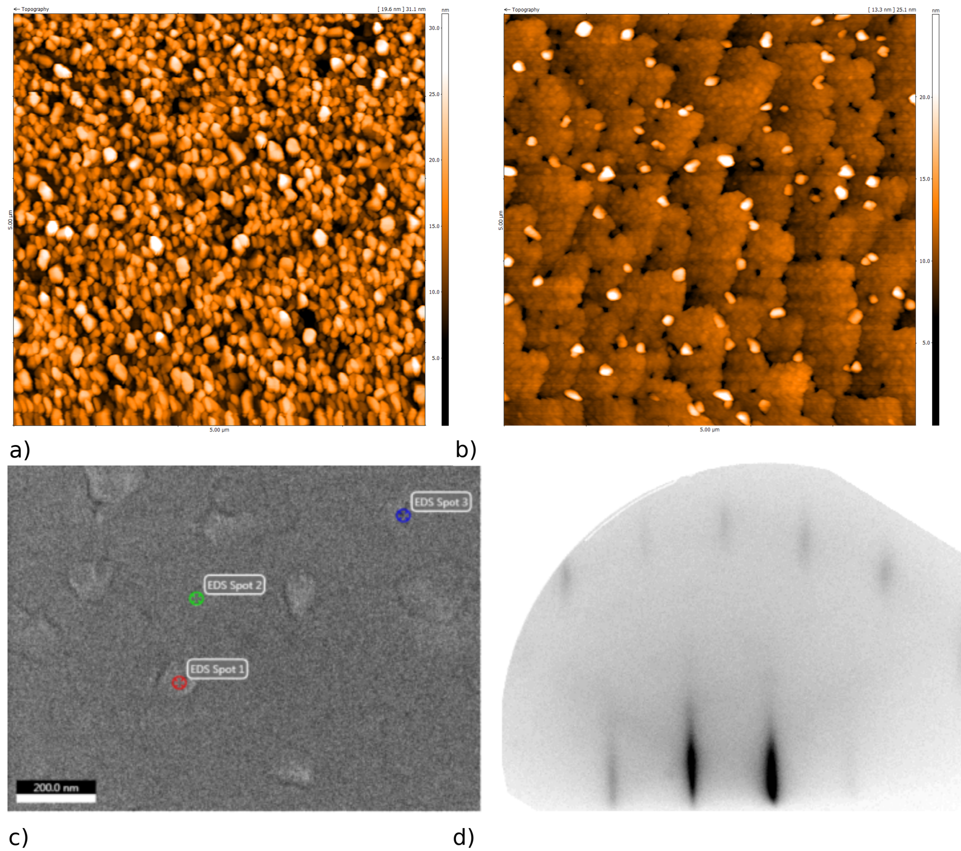

Figure 3.12: a) 5 µm × 5 µm AFM with $\Delta z = 31$ nm of the 32 nm MnSi layer from the sample series preceding the chamber changes.
b) 5 µm × 5 µm AFM with $\Delta z = 25$ nm AFM of the 26 nm MnSi layer with $T_{\mathrm{Sub}} = 290°\mathrm{C}$ and $T_{\mathrm{Mn}} = 745°\mathrm{C}$ shown in Fig. 3.11 b).
c) SEM measurement of the MnSi shown in b) with EDX measurements at the positions indicated with a Mn atomic percent of 2.1% at all three spots [Bor].
d) RHEED picture of MnSi layer shown in b) before cap layer deposition. Lightness and contrast are adjusted for better visibility.

A comparison reveals a less rough surface and terraces with steps assigned to substrate miscut for the latter, indicating the increase in quality introduced by the optimization of growth parameters after the chamber modifications. In contrast to the SEM measurement in Fig. 3.8 c), the contrast in the SEM picture shown in Fig. 3.12 c) for this layer is way less and all indicated spots measured by EDX have the same Mn atomic percent, indicating a homogeneous Mn concentration. The RHEED picture after the MnSi layer growth, shown in Fig. 3.12 d), also shows long thin streaks comparable to the wetting layer RHEED pictures from the previous section (Fig. 3.6), which again indicates a well ordered flat MnSi surface. This shows that the optimal growth parameters at the end of the recalibration and optimization are about $T_{\mathrm{Mn}} = 775°\mathrm{C}$ (before rescaling $T_{\mathrm{Mn}} = 745°\mathrm{C}$) and $T_{\mathrm{Sub}} = 290°\mathrm{C}$.
In conclusion, a way to identify the parameter range for MnSi growth has been shown by throughout examination of the growth conditions and the samples with additional Mn-rich or Mn-poor phases growing at the border to this window by XRD. XRD-measurements of samples with these additional phases indicate that they act as relaxation centers.
Investigation far outside of this growth condition window also revealed the growth of incorporated MnSi islands which could become of interest for spintronic applications as such size confinements can lead to interesting changes in the phase diagram as recently shown by Das *et al.* [DBS+18] for MnSi nanoparticles and incorporation in a Si lattice could make them more suitable for applications.
The samples grown within this growth condition window have optimal properties regarding homogeneity and surface quality and are without additional phases. Except where it is explicitly mentioned, all samples shown in the following are MnSi without additional phases. In the following, for each layer thickness on a specific substrate type the same representative sample is shown, making the thickness in combination with the substrate type a unique identifier. For the sample set shown in Fig. 3.11 b), it is the sample at $T_{\mathrm{Sub}} = 290°\mathrm{C}$ and $T_{\mathrm{Mn}} = 745°\mathrm{C}$ with a MnSi layer thickness of 26 nm. If not stated otherwise, the substrate type is always Si(111).
In the following section the principal structural characterization done at a 17 nm MnSi layer grown during the preceding work by Dr. Pohl [Poh13] will be shown. This throughout examination of the layer was done as a starting point for this work. In addition to that a layer thickness series, corresponding to the growth conditions marked by the magenta cross in Fig. 3.11 b), is examined.

3.3 Basic structural characterization

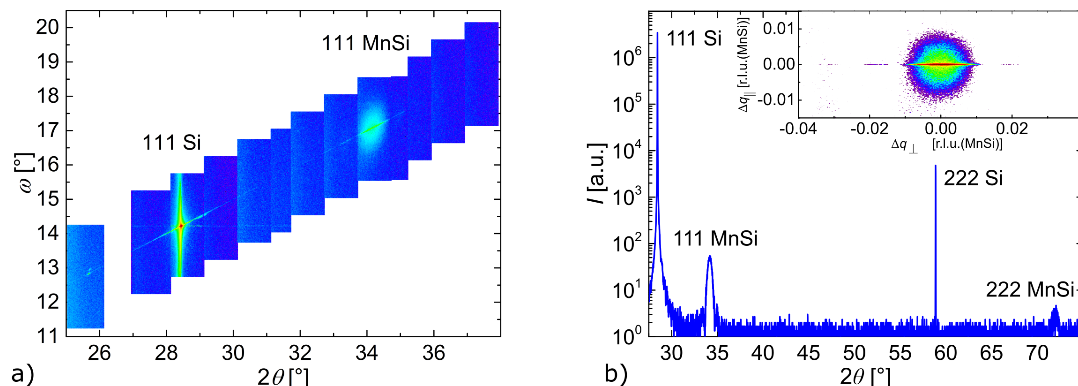

Figure 3.13: a) Real space map of the 111 Si reflection up to the 111 MnSi reflection for the 17 nm MnSi layer.
b) Corresponding $2\theta - \theta$-scan and reciprocal space map of the 111 MnSi reflection shown in a).
b) reprinted from M. Trabel, N. V. Tarakina, C. Pohl, J. A. Constantino, C. Gould, K. Brunner, and L. W. Molenkamp, Twin domains in epitaxial thin MnSi layers on Si(111), Journal of Applied Physics, 121(24):245310, 2017, https://aip.scitation.org/doi/abs/10.1063/1.4990284?journalCode=jap. [TTP+17]

As described in section 3.2.3, XRD measurements are on one hand used to identify structural phases, as their lattice parameters lead to different 2θ values owing to the Bragg relation. On the other hand they are used to determine the strain in the layer by calculating the lattice plane separation of a reflection and comparing it to the unstrained value. To get an overview of strain in the layer structures a reciprocal space map, shown in Fig. 3.13 a) was measured with a 1-D detector. Here the detector is always measuring a full line of 2θ values in parallel and for one set of measurements the corresponding ω is changed. Combining several measurements leads to fused rectangles as visible in Fig. 3.13 a). Here the horizontal and vertical lines around the 111 Si substrate reflection are resolution dependent artifacts from monochromator and analyzer [Bir06]. In addition to the standard substrate reflection at about 28.44° one sees a small peak at about 25.7° which can be explained by the Cu-$K\beta$ line of the X-Ray source, indicating that a monochromator with better resolution would be necessary but an increase in resolution would also lead to a loss in intensity.

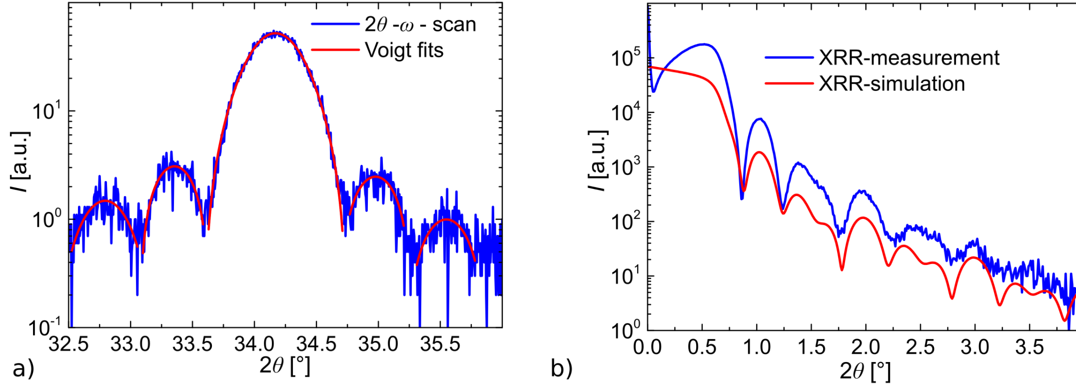

Figure 3.14: a) $2\theta - \theta$-scan of the 111 MnSi reflection of the 17 nm MnSi layer with Voigt fits for peak and fringe position determination in red.
b) XRR measurement of the same layer with a simulation for a 16.6 nm layer with 8.9 nm cap in red.

111 Si and 111 MnSi in the reciprocal space map are on the $\theta = \omega$ line with the same azimuthal angle ϕ and the same inclination angle ψ, which shows that the growth happens with Si(111) $\parallel$ MnSi(111) as expected and described in section 3.1. Fig. 3.13 b) shows a $2\theta - \theta$ scan in an even wider range to exclude additional phases as they would appear in this 2θ region comparing it with Fig. 3.7 a). The inset of Fig. 3.13 b) shows the reciprocal space map of the 111 MnSi reflection displayed in Fig. 3.13 a) in reciprocal lattice units after subtraction of a diffuse background.
The q-vector components are calculated by [Few15]

$$\begin{aligned} \Delta q_{\parallel} &= \frac{2\pi}{a_{\mathrm{MnSi}}} \left[\cos\left(\omega\right) - \cos\left(2\theta - \omega\right)\right] \\ \Delta q_{\perp} &= \frac{2\pi}{a_{\mathrm{MnSi}}} \left[\sin\left(\omega\right) + \sin\left(2\theta - \omega\right)\right] \ , \end{aligned} \tag{3.3}$$

in reciprocal lattice units $2\pi/a_{\mathrm{MnSi}}$. From the inset additional information can be gathered regarding the MnSi layer quality. Thickness fringes are visible next to the layer reflection which indicates a homogeneous layer thickness.
To calculate the thickness a $2\theta - \theta$ scan of the 111 MnSi is measured in higher resolution as shown in Fig. 3.14 a) and the fringe position determined by Voigt-fits. From the

position of the fringes the layer thickness d can be calculated with [Few15]

$$d = \frac{\lambda\,(n-m)}{2\,[\sin(\omega_m) - \sin(\omega_n)]}\ . \tag{3.4}$$

λ is the used wavelength CuKα_1 of the X-Ray source and n/m the fringe order. For the two fringes on the left side of the peak this leads to a layer thickness of $d = 16.7$ nm. Calculating the thickness from the two fringes at the right side of the peak results in a thickness of $d = 16.2$ nm. Even if the rightmost fringe is not that well defined the calculated value is the same as for the other fringes within an error of 0.5 nm.
Another way to determine the thickness of the layer is by XRR measurements, as explained in the previous section. Fig. 3.14 b) shows the XRR-measurement together with a simulation for which instrumental resolution and roughness of the layers are ignored [Bru]. The simulation with a cap layer thickness of $d_{\text{cap}} = 8.9$ nm and a MnSi layer thickness of $d = 16.6$ nm corresponds quite well to the actual XRR measurement. Within the aforementioned error it is also the same as the thickness values calculated with the XRD fringes. This indicates that both methods work well and lead to the same result, if well defined fringes are used to calculate the thickness.
What is also interesting here is that this is the same sample as the one presented by Dr. Pohl [Poh13], where he measured a layer thickness of about 20 nm, just closer to the edge of the wafer. This difference highlights one of the problems with the growth on such big wafers as well as the chamber geometry as it is shown in Fig. 3.3 b). Because the flux from the evaporation cells and the electron beam evaporator originate from such different positions, the substrate position has to be chosen in a way to accommodate both as well as to allow RHEED analysis. These difficulties can easily account for the difference in layer thickness, but what is remarkable here is that the layer quality is not influenced and no other phases are introduced. From the 111 MnSi position $2\theta = 34.17°$ in Fig. 3.14 a) one also can calculate the lattice spacing $d_{111} = 2.62$ Å with Eq. 2.3 and Eq. 2.4, which is only 0.4% smaller than the bulk value. Comparing this with the misfit of 3.1% calculated with Eq. 3.1, as discussed in section 3.2.3, indicates that the layer is mostly relaxed.
The reciprocal space map in the inset of Fig. 3.13 b) shows that the sharp layer peak is accompanied by a circular diffusive background which can be assigned to local strain fields due to misfit dislocations at the interface between substrate and layer [KKS+97].

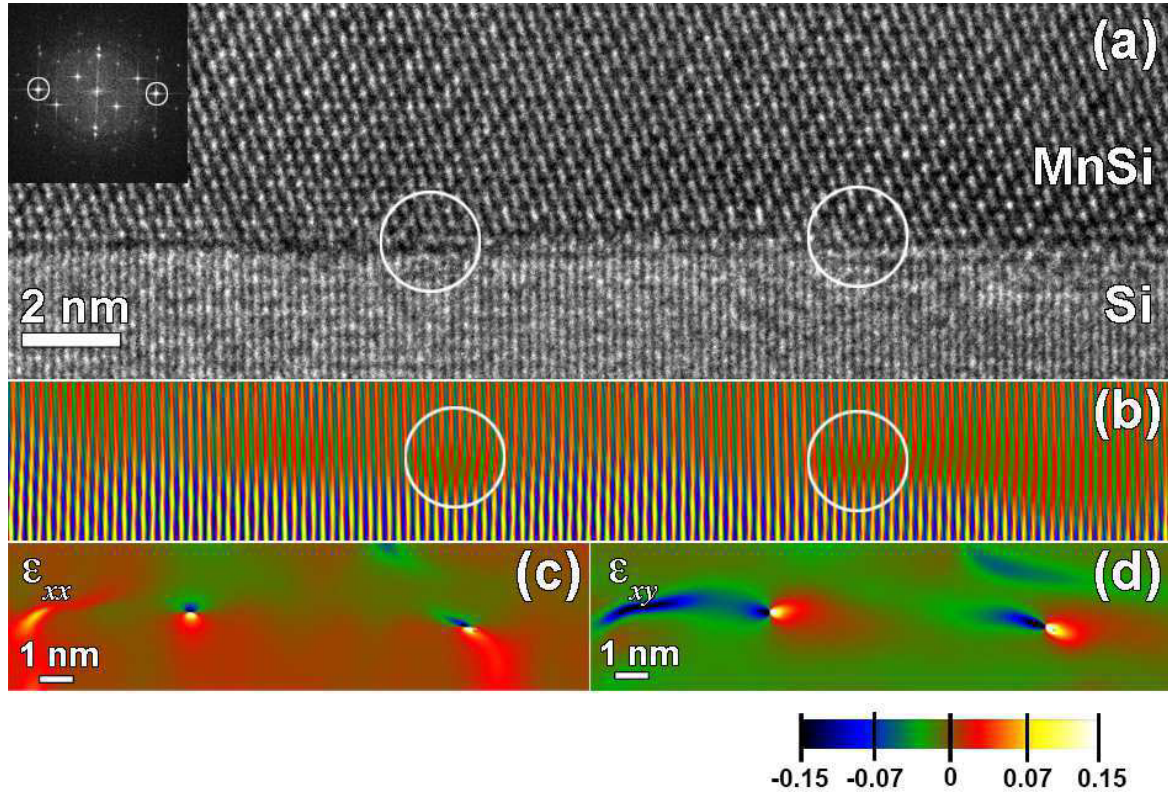

Figure 3.15: a) High resolution TEM of the substrate layer interface of the 17 nm MnSi layer along the Si[$\bar{1}\bar{1}2$] direction and the corresponding Fast Fourier transformation in the inset with $\bar{2}11$ and $\bar{1}\bar{2}1$ reflections encircled.
b) False-color Bragg filtered image created with these reflections and with misfit dislocation cores pointed out by circles here and in a).
c) Lateral and d) shear component of the strain tensor ϵ from geometrical phase analysis.
Reprinted from M. Trabel, N. V. Tarakina, C. Pohl, J. A. Constantino, C. Gould, K. Brunner, and L. W. Molenkamp, Twin domains in epitaxial thin MnSi layers on Si(111), Journal of Applied Physics, 121(24):245310, 2017, https://aip.scitation.org/doi/abs/10.1063/1.4990284?journalCode=jap. [TTP+17] and [Tar].

Fig. 3.15 a) shows a high resolution TEM image of this interface along the Si$[\bar{1}\bar{1}2]$ direction [Tar]. Encircled are two misfit dislocation cores visible at the atomically abrupt interface. The inset shows a Fast-Fourier transformation of the image with the $\bar{2}11$ and $\bar{1}\bar{2}1$ reflections encircled. These are used to create the false-color Bragg filtered image shown in Fig. 3.15 b) where the two dislocation cores, again encircled, are clearly visible. The lateral and shear component of the strain tensor ϵ shown in Fig. 3.15 c) and d) show a local strain field at the dislocation cores of up to ±15% over a range of about 2 nm [TTP+17].

Fig. 3.16 shows an ω-scan of the 111 MnSi reflection with a cumulative Voigt fit to separate the actual reflection from the diffusive background. The Full Width Half Maximum (FWHM) of the diffuse background is about 0.8° and that of the Bragg reflection is about 0.02°, which indicates a good alignment of the corresponding lattice planes.

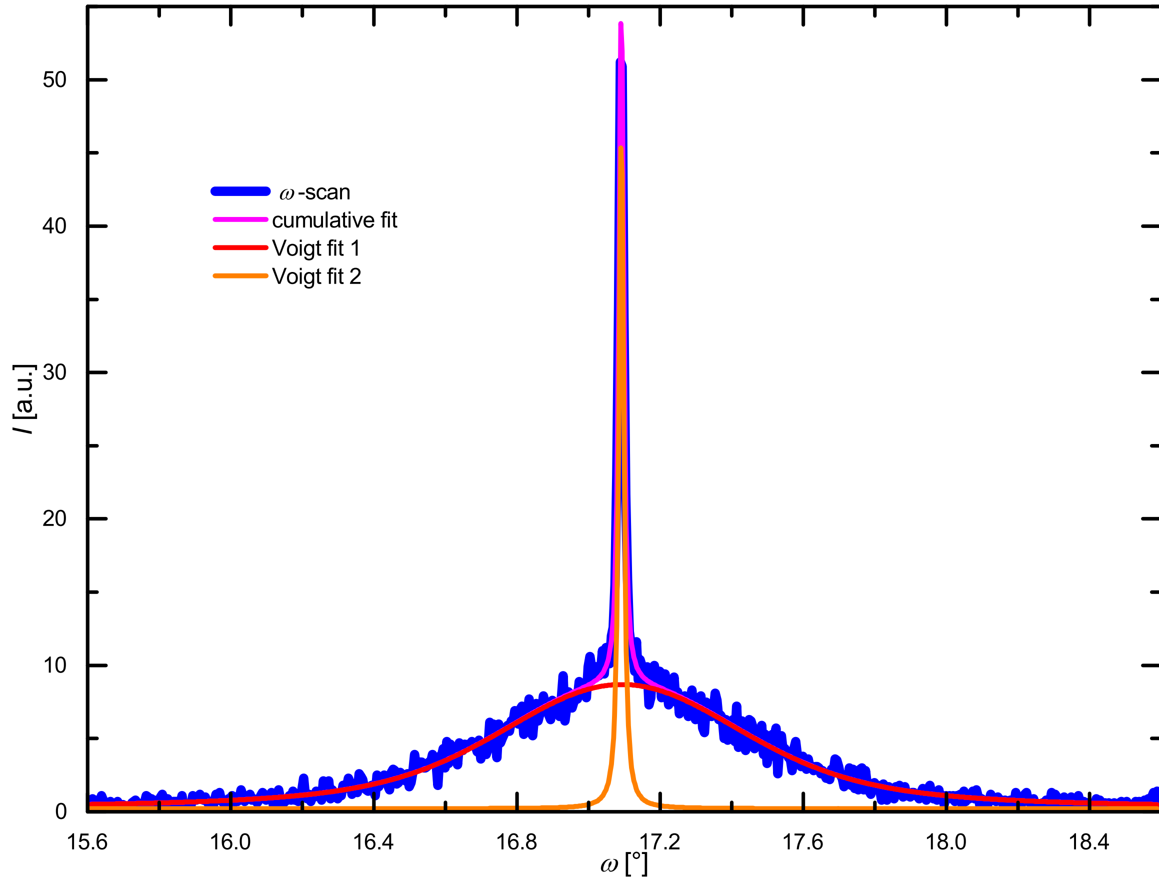

Figure 3.16: ω-scan of the 111 MnSi reflection of the 17 nm MnSi layer with a cumulative fit of two Voigt fits.

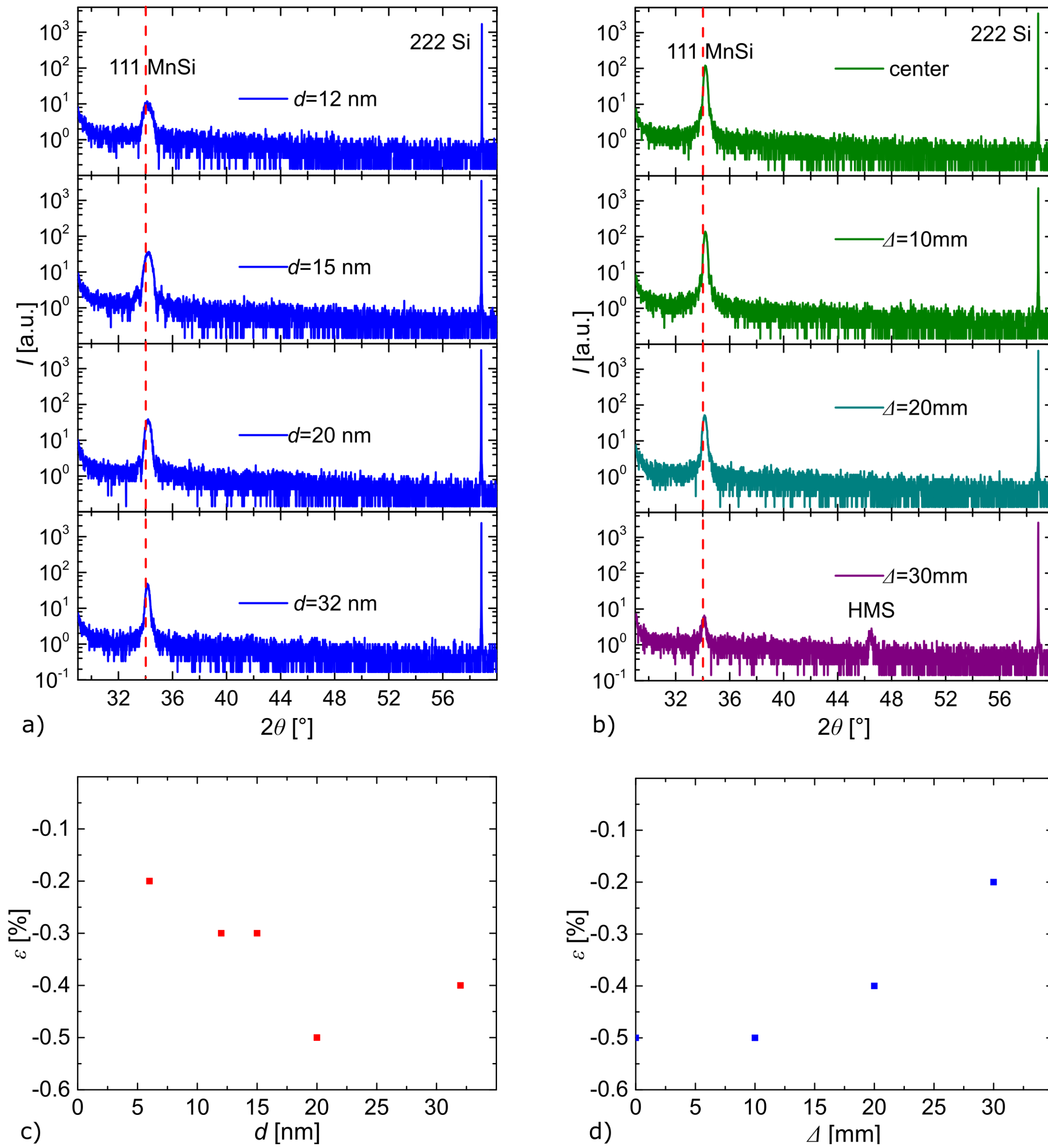

Figure 3.17: a) $\theta - 2\theta$-scans of a thickness dependent sample series with the thickness indicated by the labels.
b) $\theta - 2\theta$-scans of different positions on the 32 nm layer shown in a) with the distance Δ to the wafer center indicated by the labels.
In both graphs the bulk value for the 111 Mnsi reflection is indicated by the red dashed line.
c) Residual perpendicular strain dependence on layer thickness d
d) and on distance to the wafer center Δ.

Fig. 3.17 a) shows $\theta - 2\theta$ scans for a series of samples with different layer thicknesses and with no additional reflections in a wide 2θ range indicating that it is only manganese monosilicide. The 2θ position of the 111 MnSi reflection in comparison to the literature value indicated by the dashed red line gives a reduction of the vertical lattice parameter by about -0.4% for the 32 nm down to about -0.3% for the 12 nm layer, as shown in Fig. 3.17 b).
The corresponding $2\theta - \theta$ scan of the 111 MnSi reflection for the thinnest layer grown in this series, which is nominally 5 nm and according to XRR-measurements about 5.6 nm, is shown in Fig. 3.18 a). Because of the XRR result it is called the 6 nm layer in the following. Here the 2θ value of the reflection reveals a reduction of 0.2%. This dependence on display in Fig. 3.17 c) shows a similar trend to the values obtained by Karhu *et al.* [KRB$^+$12] for MBE grown samples with the minimum strain value for the lowest thickness. Comparing all values indicates a residual strain within the experimental accuracy of $\pm0.2\%$ for the measurement series in Fig. 3.17 and a critical thickness for relaxation below the thinnest layer thickness grown. This corresponds well to the work by Kumar *et al.* [KTH$^+$04] where a dislocation network is already seen for a seed layer from annealing 5 ML Mn.

The thickness of the layers can vary over the range of the 3 in wafer, as mentioned in the beginning of the section. Fig. 3.17 b), measured on the 32 nm layer shown in a), shows what happens to strain and crystal quality depending on the distance to the wafer center. The measurements at the center and at a distance of $\Delta = 10$ mm to the center show practically no difference and both 2θ values of the 111 MnSi reflection indicate a residual strain of about -0.4%. At a distance of $\Delta = 20$ mm the intensity as well as the residual strain is slightly decreased, as also shown in Fig. 3.17 d). The decrease in intensity could come from the misalignment in XRD, as the alignment of the wafer within the diffractometer is done by measuring the substrate reflection at the wafer center. The slight decrease in strain could also be explained by the measurement error, but it could also indicate a small decrease in crystal quality, as discussed in section 3.2.3. For this reason sample pieces for further processing are normally taken from $\Delta < 20$ mm. At $\Delta = 30$ mm Fig. 3.17 b) shows the appearance of HMS, which is reasonable as this measurement includes the region where the wafer is clamped and the Mn flux is partially shadowed.

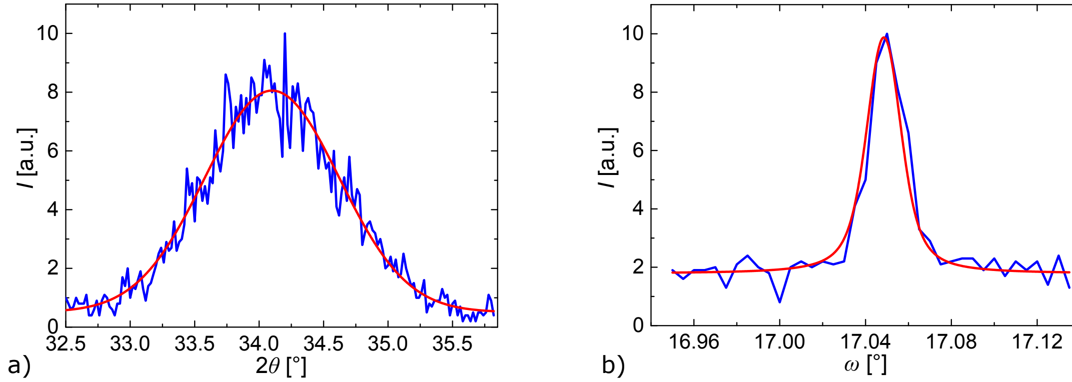

Figure 3.18: a) $2\theta - \theta$-scan of the 111 MnSi reflection for the 6 nm layer with Voigt fit in red to determine the reflection position.
b) $\omega-$scan corresponding to a) with Voigt fit in red to determine the FWHM.

For the 111 MnSi reflection of the 6 nm film an ω-scan is shown in Fig. 3.18 b) again revealing a small FWHM of about 0.02° which indicates the well aligned lattice planes. For the in-plane strain the reciprocal lattice vector for a corresponding asymmetric reflection is calculated with

$$q_{\|} = \sin(\psi)\,\frac{2\sin(\theta)}{\lambda}\ , \tag{3.5}$$

according to [Poh13] based on [War90], and the inclination angle ψ between the corresponding plane and (111). Fig. 3.19 a) shows the azimuthal ϕ-scan of the 211 MnSi reflection. The sample is tilted by the inclination angle between the corresponding plane and (111) and rotated around the surface with the azimuthal angle ϕ, as shown in Fig. 2.3. For this measurements a tilt stage was available, with which the rotation axis can be aligned to the (111) axis. This means that the sample alignment is relatively equal for all ϕ values, which can be seen from the comparable amplitudes.
Fig. 3.19 b) shows the corresponding $2\theta - \omega$-scan in $\omega+$ geometry for the reflection at $\phi \approx 120°$. For this measurement, the inclination angle between the corresponding plane and (111) is added to the nominal ω value. The in-plane reciprocal lattice vector calculated from the peak position of $2\theta = 49.04°$ is 0.3% larger than the corresponding bulk value.
Fig. 3.20 a) shows the corresponding azimuthal ϕ-scan of the 211 MnSi reflections for the 6 nm layer and Fig. 3.20 b) the corresponding 2θ-scan in $\omega+$ geometry for the

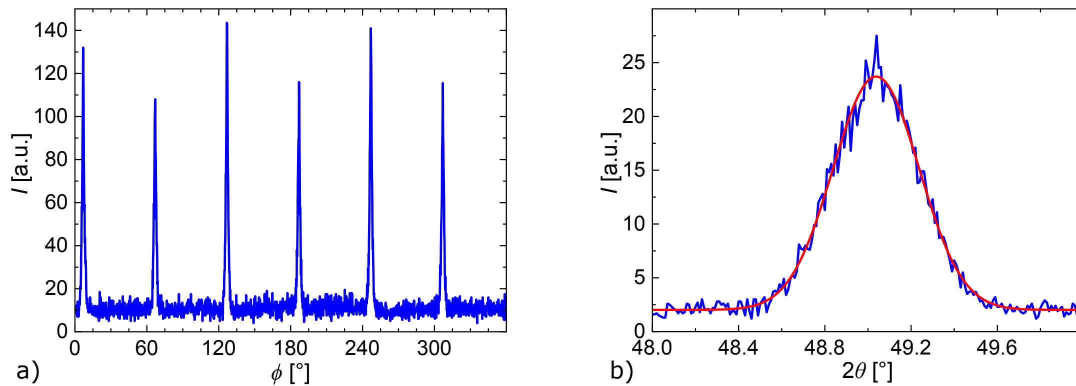

Figure 3.19: a) Azimuthal ϕ-scan for the MnSi {211} reflections of the 17 nm layer shown in Fig. 3.13 and 3.14.
b) $2\theta - \omega$-scan in ω+-geometry for the reflection in a) at about 120° with Voigt fit in red for reflection position determination.

reflection at $\phi \approx 210°$. Here the calculation reveals a reciprocal lattice vector about 0.2% larger than the bulk value, again indicating a small tensile in-plane strain and a critical thickness below the layer thickness.

Looking at the peaks in Fig. 3.19 a) as well as Fig. 3.20 a) one sees six instead of three peaks expected for the MnSi {211} reflections. This is a clear sign for twinning in the layers which will be discussed in the following section.

In summary the MnSi layers show a good crystal quality over a broad area of the 3 inch wafer. The layers are mostly relaxed and the relaxation mechanism is identified as misfit dislocations at the interface between substrate and layer.

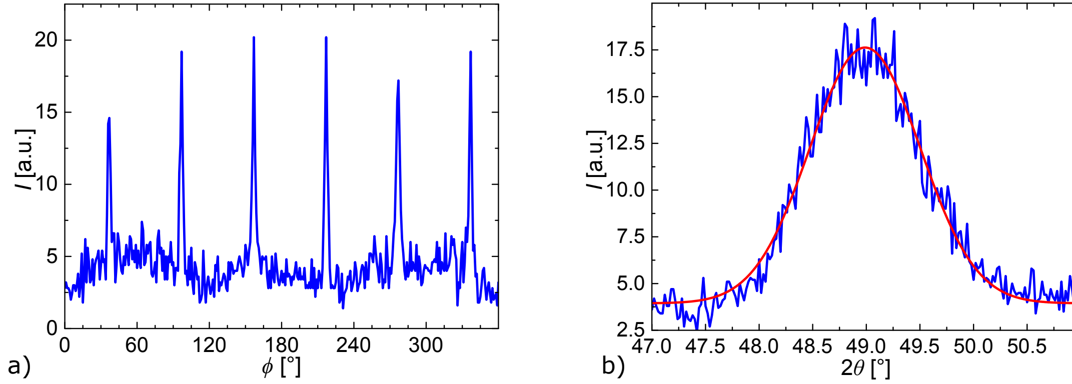

Figure 3.20: a) Azimuthal ϕ-scan for the MnSi {211} reflections of the 6 nm layer shown in Fig. 3.18.
b) $2\theta - \omega$-scan in $\omega+$-geometry for the reflection in a) at about 210° with Voigt fit in red for reflection position determination.

3.4 Structural characterization of twin domains

To determine the in plane orientation of MnSi to Si and to get more information on the twinning mechanism, more azimuthal ϕ-scans of layer reflections as well as the substrate of the 17 nm layer previously discussed are analyzed.

Fig. 3.21 a) shows an azimuthal ϕ-scan of the asymmetric Si {400} reflections with three peaks, meaning 400 Si, 040 Si and 004 Si, as expected for the threefold symmetry of Si(111). The corresponding measurement of MnSi, as shown in Fig. 3.21 b) reveals six instead of the expected three peaks from the threefold symmetry of MnSi(111). Taking only these two measurements into account one could assume rotational twinning as the reason for MnSi domains with one domain rotated +30° around the surface normal with respect to the Si direction, labeled 1 in Fig. 3.21 b), and the other domain rotated −30°, labeled 2. From the averaged area of Voigt-fits to the peaks, shown in Fig. 3.21 b), one gets a intensity ratio of about 1.2 between the two domains, indicating an equal volume fraction within the accuracy of the measurement. The variation could be caused by sample misalignment and different tilt for the different twin domains.

Additional measurements of asymmetric reflections reveal a more complex relation between the twin domains. Fig. 3.22 a) shows the azimuthal ϕ-scan of the asymmetric MnSi {210} reflections with six peaks, as expected for this reflection family, with the 210 MnSi, 201 MnSi, 120 MnSi, 102 MnSi, 012 MnSi and 021 MnSi reflections.

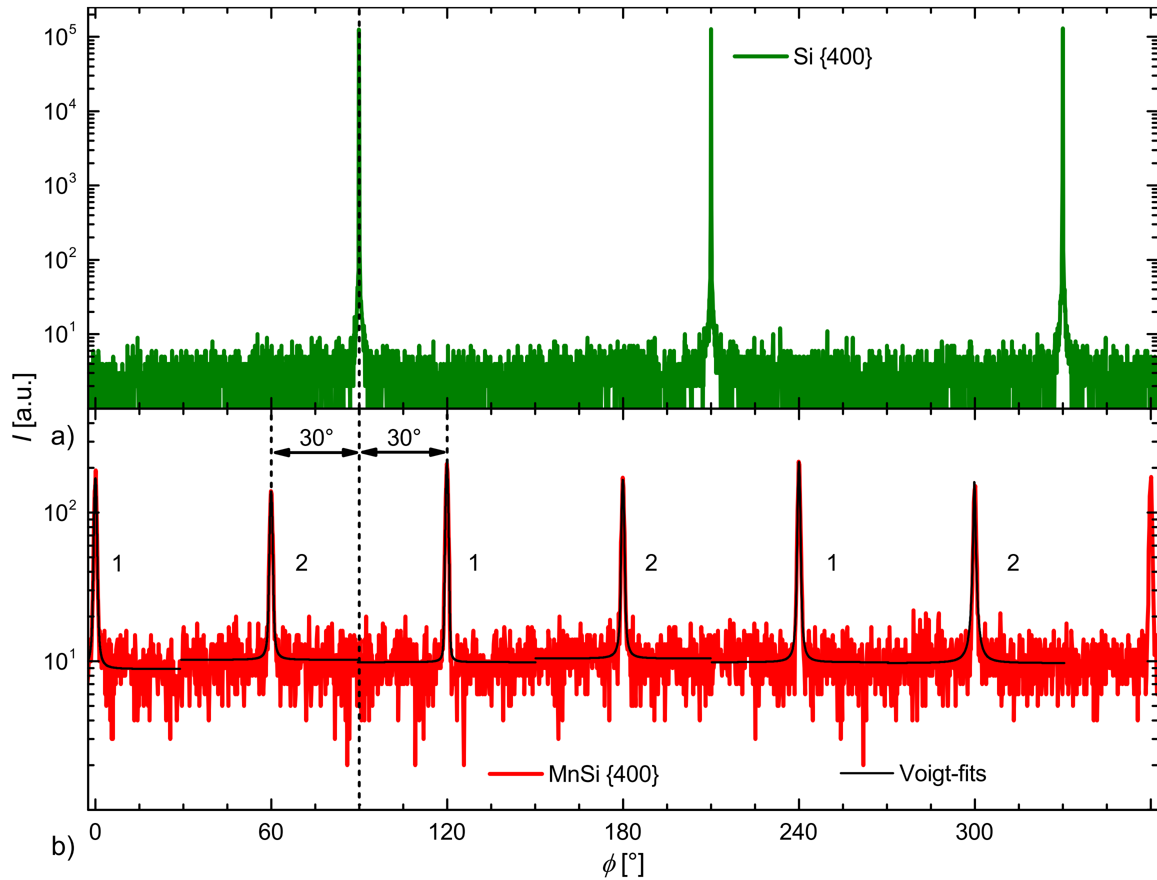

Figure 3.21: Azimuthal ϕ-scans for the family of a) Si {400} and b) MnSi {400} reflections of the 17 nm layer with $\phi = 0°$ defined as the Si $[\bar{1}10]$ direction and the Si $[\bar{1}\bar{1}2]$ direction indicated by the dashed line. Different MnSi domains are labeled as 1 and 2.
Reprinted with changed layout and additional fits from M. Trabel, N. V. Tarakina, C. Pohl, J. A. Constantino, C. Gould, K. Brunner, and L. W. Molenkamp, Twin domains in epitaxial thin MnSi layers on Si(111), Journal of Applied Physics, 121(24):245310, 2017, https://aip.scitation.org/doi/abs/10.1063/1.4990284?journalCode=jap. [TTP+17]

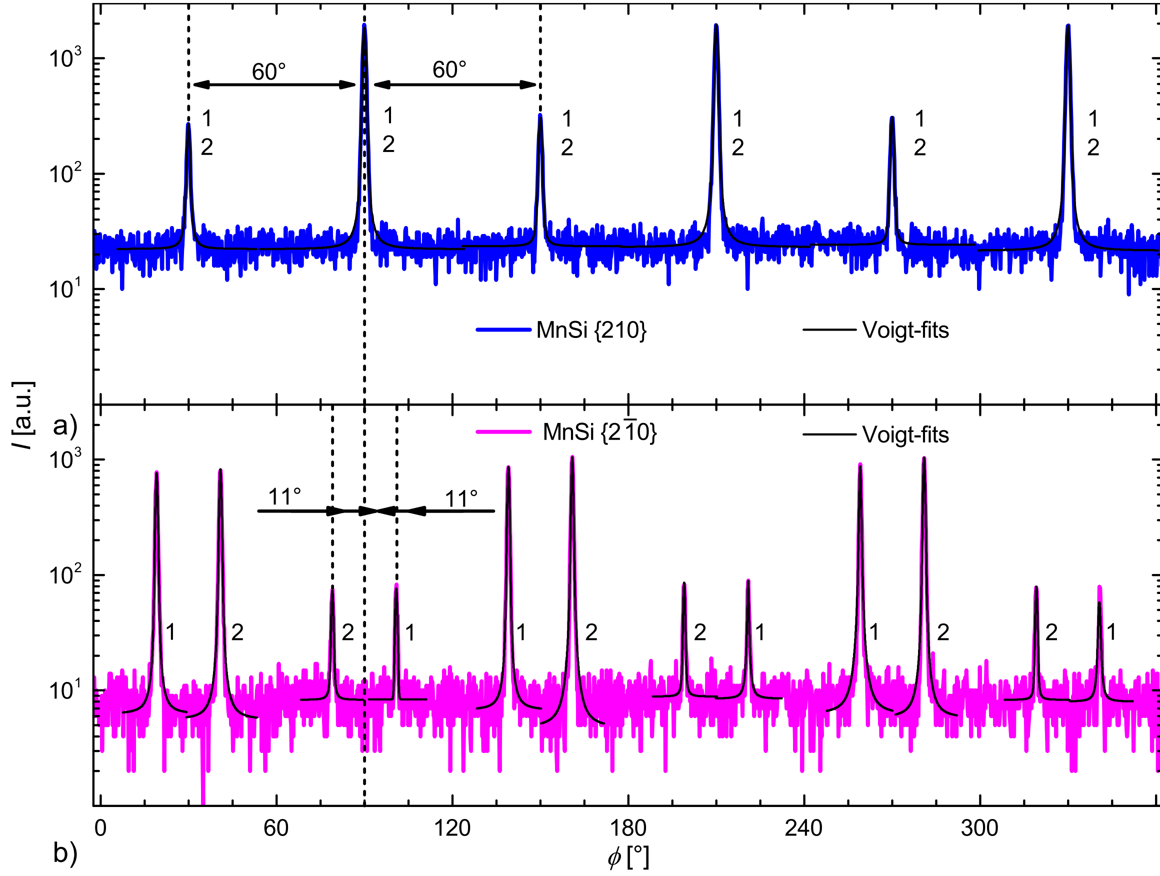

Figure 3.22: Azimuthal ϕ-scans for the family of a) MnSi {210} and b) MnSi {2$\bar{1}$0} reflections of the 17 nm layer with $\phi = 0°$ defined as the Si [$\bar{1}$10] direction and the Si [$\bar{1}\bar{1}$2] direction indicated by the dashed line. Different MnSi domains are labeled as 1 and 2.
Reprinted with changed layout and additional fits from M. Trabel, N. V. Tarakina, C. Pohl, J. A. Constantino, C. Gould, K. Brunner, and L. W. Molenkamp, Twin domains in epitaxial thin MnSi layers on Si(111), Journal of Applied Physics, 121(24):245310, 2017, https://aip.scitation.org/doi/abs/10.1063/1.4990284?journalCode=jap. [TTP+17]

There are two sets of intensities for the reflections as explained in chapter 2.2.2. From the averaged area of Voigt-fits to the peaks, shown in Fig. 3.22 a), one gets an intensity ratio of about 7 between the high and low intensity peaks, which agrees well with the expected value of $|F(210)|^2/|F(120)|^2 \approx 9.6$, considering the high uncertainty of the determination method as a result of misalignment and inconstant lit wafer area. So this measurement alone indicates a single crystal without twinning. It even contradicts the rotational twinning deduced from MnSi $\{400\}$ reflections as an explanation, as $\pm 30°$ rotations would superimpose a weak intensity peak of one twin domain onto a high intensity peak of the other domain. Taking the equal volume fraction into account this would lead to six peaks of equal intensities.
What can explain both measurements of the MnSi $\{400\}$ and $\{210\}$ reflections is a change in chirality accompanied by a $\pm 30°$ rotation with respect to the substrate. As discussed in chapter 2.2.2, the change of chirality from right- to left-handed MnSi by a mirror operation at the $(\bar{1}10)$ plane changes nothing for the MnSi $\{400\}$ reflections shown in Fig. 3.21 a), as all h, k, l are even. For the MnSi $\{210\}$ reflections shown in Fig. 3.22 b), this switches high and low intensities between the reflections of one and the other twin domain. Together with the $\pm 30°$ rotation this results in a superposition of a high intensity peak of one domain and a high intensity peak of the other domain and the same for the weak intensity peaks, which is exactly what the measurement shows.
Taking a suitable MnSi reflection one can even visualize the structural relation between the domains within one azimuthal ϕ-scan. Such a reflection is MnSi $\{2\bar{1}0\}$, shown in Fig. 3.22 b). Expected for this reflection of a single crystal are again six peaks with two sets of intensities and a ratio of $|F(2\bar{1}0)|^2/|F(\bar{1}20)|^2 \approx 9.6$, the same as for MnSi $\{210\}$. Instead we see 12 peaks with two sets of intensities that have a ratio of about 13 for the averaged area of Voigt-fits to the peaks, shown in Fig. 3.22 b). With the ratio for MnSi $\{210\}$ this gives on average about the expected ratio from the calculations. The big difference again indicates the uncertainty of the determination method.
If one gets a superposition of peaks for the twin domains as for MnSi $\{210\}$ or separated peak positions as for MnSi $\{400\}$ or MnSi $\{2\bar{1}0\}$, depends on the in-plane angle ϕ_m of the vector hkl with respect to the mirror plane $(\bar{1}10)$ given by Eq. 2.6 and 2.7. If $\phi_m = 0° \pm n \times 120°$, with integer n, the direction is within the mirror plane or an equivalent one, meaning the mirror operation maps the twin reflection on the original reflection.

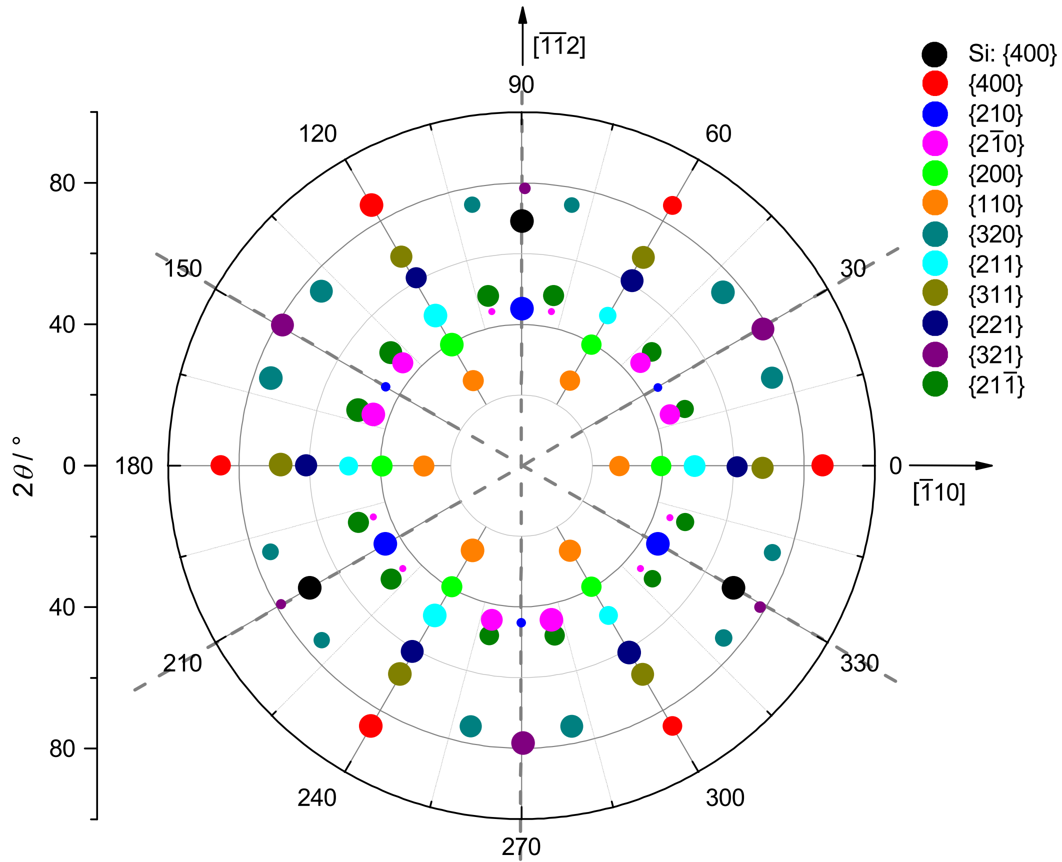

Figure 3.23: Polar plot representation of azimuthal ϕ-scans Si {400} as reference and different MnSi reflections of the 17 nm layer with the Si [$\bar{1}10$] Si [$\bar{1}\bar{1}2$] directions indicated by the arrows. Si ($\bar{1}10$) planes are indicated by the dashed lines. The dot diameter corresponds to the maximum intensity of the peak normalized to the maximum intensity within each reflection family. Reprinted from M. Trabel, N. V. Tarakina, C. Pohl, J. A. Constantino, C. Gould, K. Brunner, and L. W. Molenkamp, Twin domains in epitaxial thin MnSi layers on Si(111), Journal of Applied Physics, 121(24):245310, 2017, https://aip.scitation.org/doi/abs/10.1063/1.4990284?journalCode=jap. [TTP+17]

With the ±30° rotation the position $\phi(hkl)$ of each reflection can be calculated with [TTP+17]

$$\begin{aligned} \phi(hkl) =& \phi_m(hkl) \pm 30^\circ \text{ for } (2l-k-h) \geq 0 \\ \phi(hkl) =& 360^\circ - \phi_m(hkl) \pm 30^\circ \text{ for } (2l-k-h) < 0 \end{aligned} \tag{3.6}$$

for each twin domain.
Fig. 3.23 shows a polar plot of azimuthal ϕ-scans with the calculated diffraction angle 2θ as the distance to the center for many families of MnSi reflections together with Si {400} as a reference reflection.

The intensity, normalized within each family of reflections as $\sqrt{I/I_{\max}}$ is represented by the dot diameter and in agreement with the discussed twinning mechanism. This Laue-like diffraction pattern has three mirror planes, corresponding to the $\{\bar{1}10\}$ planes of the Si substrate, as expected for the discussed mirror twinning.
XRD measurements average over a big volume of the investigated layer, which is why further TEM-measurements are applied to get a real picture of the twin domains.
Fig. 3.24 a) shows a Selected Area Electron Diffraction (SAED) pattern taken along the Si $[\bar{1}\bar{1}2]$ direction with Si reflections marked with white labels and the MnSi reflections with colored labels. This shows the crystallographic orientation of layer to substrate with [111] MnSi || [111] Si and $\langle\bar{1}01\rangle$ MnSi || $\langle\bar{1}\bar{1}2\rangle$ Si which agrees with the orientation expected from literature discussed in section 3.1 [TTP+17].
For the MnSi reflections two sets of reflections, labeled in red and blue, are visible. This is expected for the twinned system instead of a single crystal and reflections belonging to one twin domain are labeled in red and the others in blue. The positions can again be explained by a mirror operation at the $(\bar{1}10)$ plane and the resulting surface cells for right- and left-handed MnSi are shown in Fig. 3.25 together with the Si surface cell.
Another possibility to explain TEM and XRD measurements is an upside-down turn of the crystal structure in the sense of a 180° rotation about Si $\langle\bar{1}\bar{1}2\rangle$. Both possibilities can not be distinguished in the XRD measurements and within the resolution of our TEM measurements. What can be excluded is an inversion operation, in the sense of a combination of 180° rotation and mirror operation, as this is the same as a sign change of all Miller indices which does not change the intensities as $|F^{\mathrm{R}}(hkl)| = |F^{\mathrm{R}}(\bar{h}\bar{k}\bar{l})|$ [IEM+85].

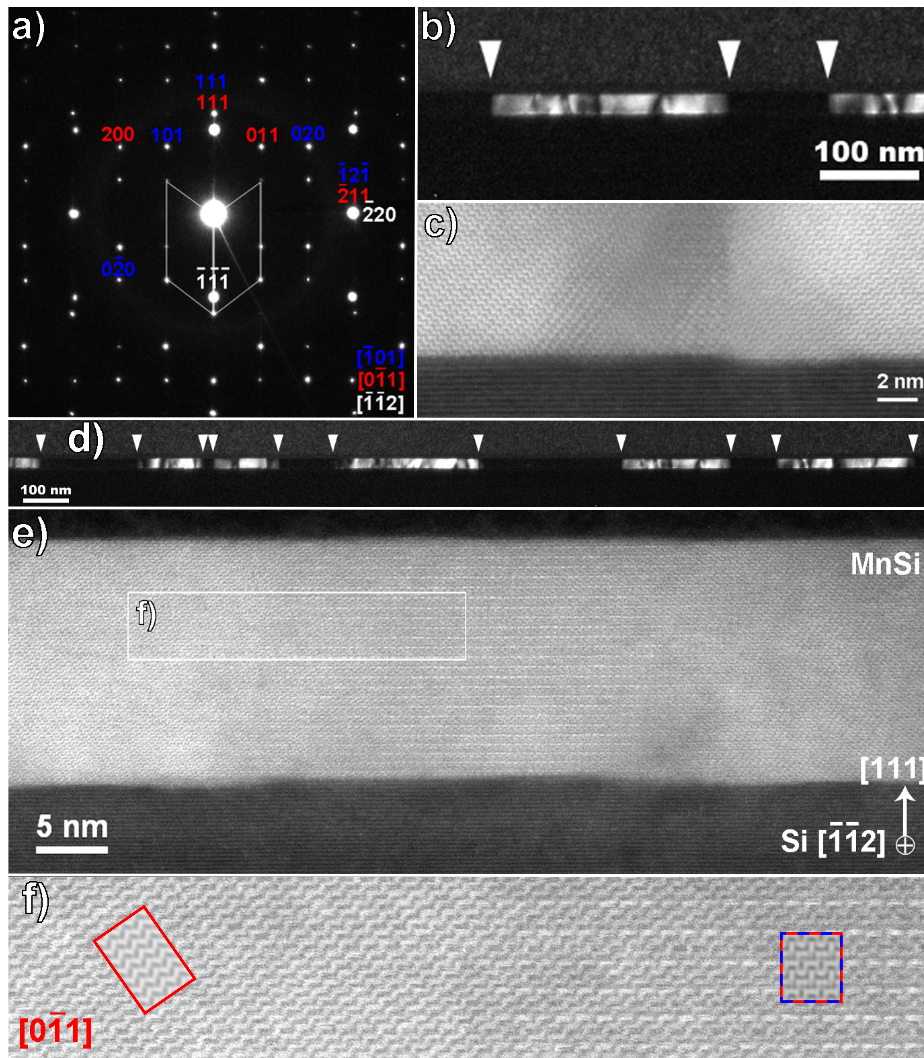

Figure 3.24: a) SAED of the 17 nm MnSi layer along the Si $[\bar{1}\bar{1}2]$ direction with the labels for Si reflections in white and for the MnSi twin reflections in red and blue.
b) Dark field TEM for the 200 MnSi reflection in a)
c) High angle annular dark field scanning TEM (HAADF-STEM) along the Si $[\bar{1}\bar{1}2]$ direction with a grain boundary between two twin domains.
d) Wide range of b).
e) HAADF-STEM of a). f) Enlargement of e) with overlapping twins (red/blue) and single domain regions (red) and simulations within the colored rectangles.
Reprinted from M. Trabel, N. V. Tarakina, C. Pohl, J. A. Constantino, C. Gould, K. Brunner, and L. W. Molenkamp, Twin domains in epitaxial thin MnSi layers on Si(111), Journal of Applied Physics, 121(24):245310, 2017, https://aip.scitation.org/doi/abs/10.1063/1.4990284?journalCode=jap. [TTP$^+$17] and [Tar].

Under the assumption that magnetic and crystal handedness are linked, as described in section 2.3, and that twinned MnSi layers have both types of magnetic handedness, as shown by Karhu *et al.* [KKR+11], only the mirror operation can be realized. An upside down turn does not change the handedness of the crystal structure so it would not change the magnetic handedness.
The TEM measurements shown in Fig. 3.24 can also give information about the size of the domains and the domain boundaries between them. Fig. 3.24 b) shows a dark field TEM image from the 200 reflection (red) in Fig. 3.24 a), which means it is bright when there is intensity at the position of reflection 200 and otherwise dark.

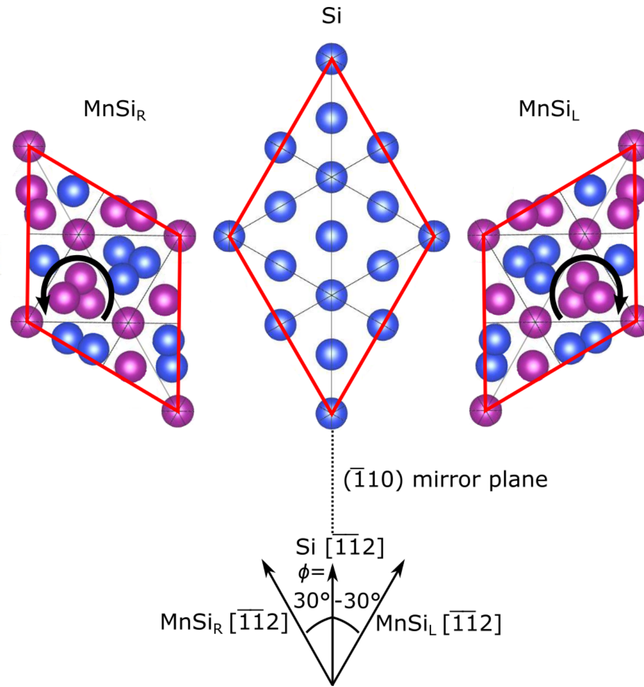

Figure 3.25: Surface cells in red of Si in the middle and right- and left-handed MnSi on the left and right with ±30° rotation with respect to Si. Si atoms are blue and Mn atoms are purple. The handedness is indicated by the circle arrows and the crystal directions are indicated by the straight arrows as well as the mirror plane ($\bar{1}$10) by a dashed line.
Reprinted from M. Trabel, N. V. Tarakina, C. Pohl, J. A. Constantino, C. Gould, K. Brunner, and L. W. Molenkamp, Twin domains in epitaxial thin MnSi layers on Si(111), Journal of Applied Physics, 121(24):245310, 2017, https://aip.scitation.org/doi/abs/10.1063/1.4990284?journalCode=jap, pictures of the crystal structures produced with Vesta 3 [MI11]. [TTP+17]

This is a direct measurement of the twin distribution, as one twin domain has a reflection at this position of the SAED pattern and the other domain not. From a wide range of the same measurement, shown in Fig. 3.24 d), one can estimate a lateral domain size of about 200 nm. [TTP+17]
Fig. 3.24 c) shows the HAADF-STEM measurement of a rather narrow grain boundary at the $(\bar{1}10)$ plane between two twin domains. The Si $\langle\bar{1}\bar{1}2\rangle$ direction is within the boundary plane, so measurements along this direction can reveal narrow grain boundaries and overlapping domains with boundaries inclined by 120°. The latter is shown in Fig. 3.24 e) and in an enlargement of the relevant region in f). Here a single domain is visible on the left, as well as an overlap of both twin domains on the right. Simulation with the JEMS package [Sta87], shown within the rectangles where the red color indicates a single domain and the red/blue color a domain overlap, agree well with the TEM image and show that the domains are mirrored without translational shift. [TTP+17]
In conclusion our XRD and TEM measurements are well explained by mirror twin domains of equal volume fraction with a $(\bar{1}10)$ mirror plane and a $\pm 30°$ rotation around [111]. We cannot exclude 180° rotations, but the observation of left and right handed magnetic domains in the literature contradicts this possibility.
In the following section possible ways to suppress twinning by growth on special Si substrates will be discussed.

3.5 Suppression of twin domains

In the following sections two approaches to suppress twinning will be discussed. Both are based on the assumption that the interface of the substrate can be used to suppress one of the twins. The first method is the growth on substrates miscut with an off angle to the Si(111) plane. The second method is the growth on chiral high index substrates.

3.5.1 Growth on Si(111) substrate with miscut

The growth on Si (111) miscut with an off angle of 2° to the Si(111) plane in different directions, leads to different step edge configurations. The idea is that the dangling bond configuration at these edges energetically favors one type of twin domain.
Growth on miscut substrates has successfully been used for twin suppression on other material systems, for example recently for $B_{12}P_2$ on 4H-SiC, where different miscut leads to different step etching which results in twin suppression, or for GaP on miscut Si(111) [FSP+18, KPS+16].
Fig. 3.26 shows the 2° off angle as well as the different tilt directions. The Si(111) plane of a step is indicated in top- and side-views with the step edges marked by the black dashed lines. The terrace width is a result of the miscut angle.
As the growth on these substrates, except for one, happened directly after the calibration series shown in Fig. 3.11 b) the growth parameters are $T_{\mathrm{Sub}} = 290$°C and $T_{\mathrm{Mn}} = 775$°C (or $T_{\mathrm{Mn}} = 745$°C before rescaling).
The upper two off angle directions in Fig. 3.26 are in principle equivalent, which means one can be taken as reference for the other. Comparing their step edge configuration with the other two reveals three very distinct cases, making a different influence on the growth quite plausible.
To measure if twin suppression occurs, azimuthal XRD ϕ-scans of the MnSi $\{2\bar{1}0\}$ reflection family are used as described in section 3.4. The wafer orientation within the coordinate system of the X-Ray Diffractometer is adjusted to the Si 111 reflection at $\phi = 0°$. Because of the miscut of the substrate this results in a misalignment at other ϕ positions, but as a $20\bar{1}$ reflection from one twin domain is always close to one for the other domain, geometrical correction factors are similar and their intensities can still be compared. For that Voigt-functions are fitted and their areas compared.

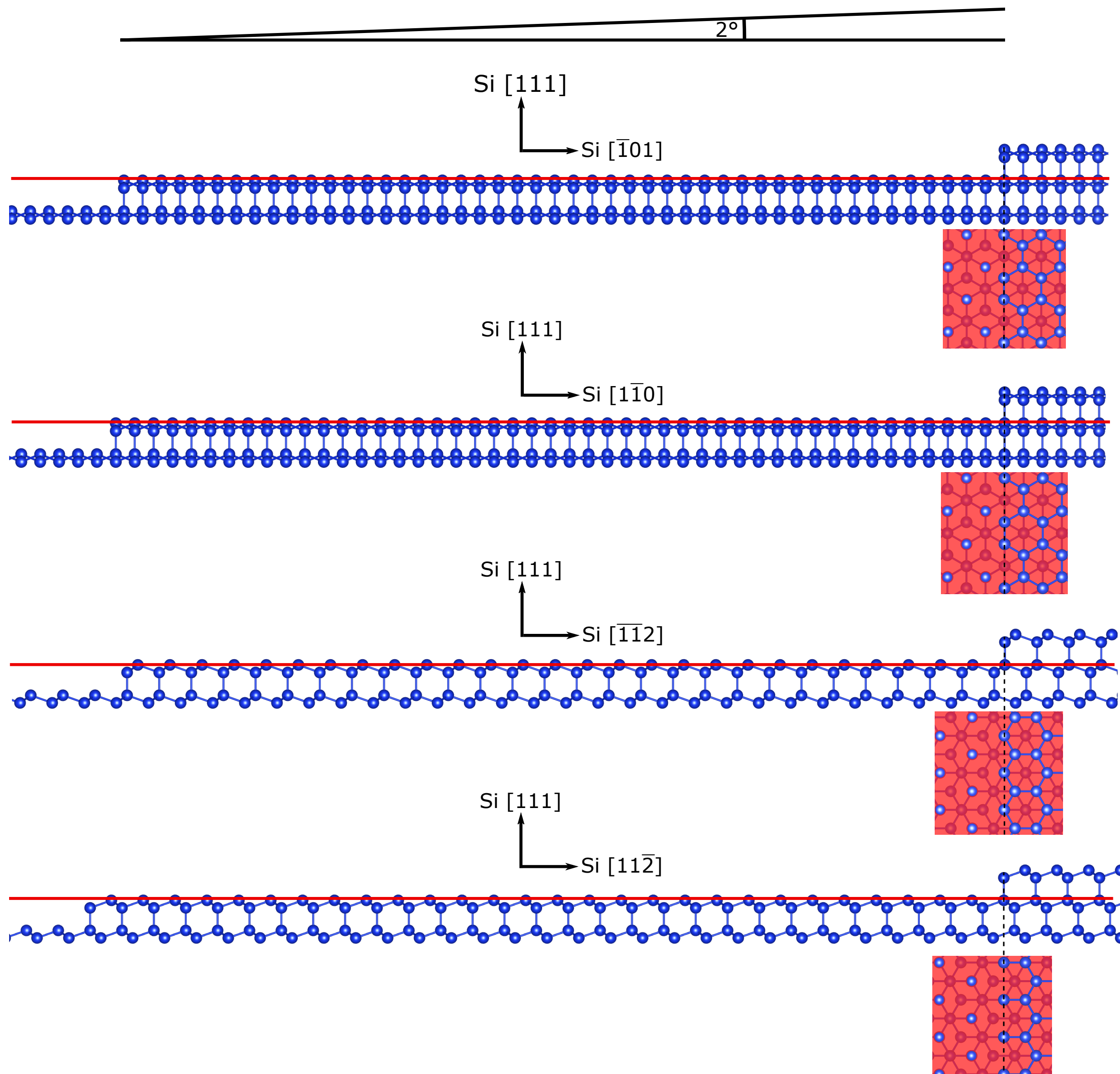

Figure 3.26: Side- and top-view on different inclinated substrates with a cut off angle of 2° to the Si (111) surface. The cutoff directions are indicated by the Si direction arrows and the Si (111) surface by the red plane.
Pictures of the crystal structures have been produced with Vesta 3 [MI11].

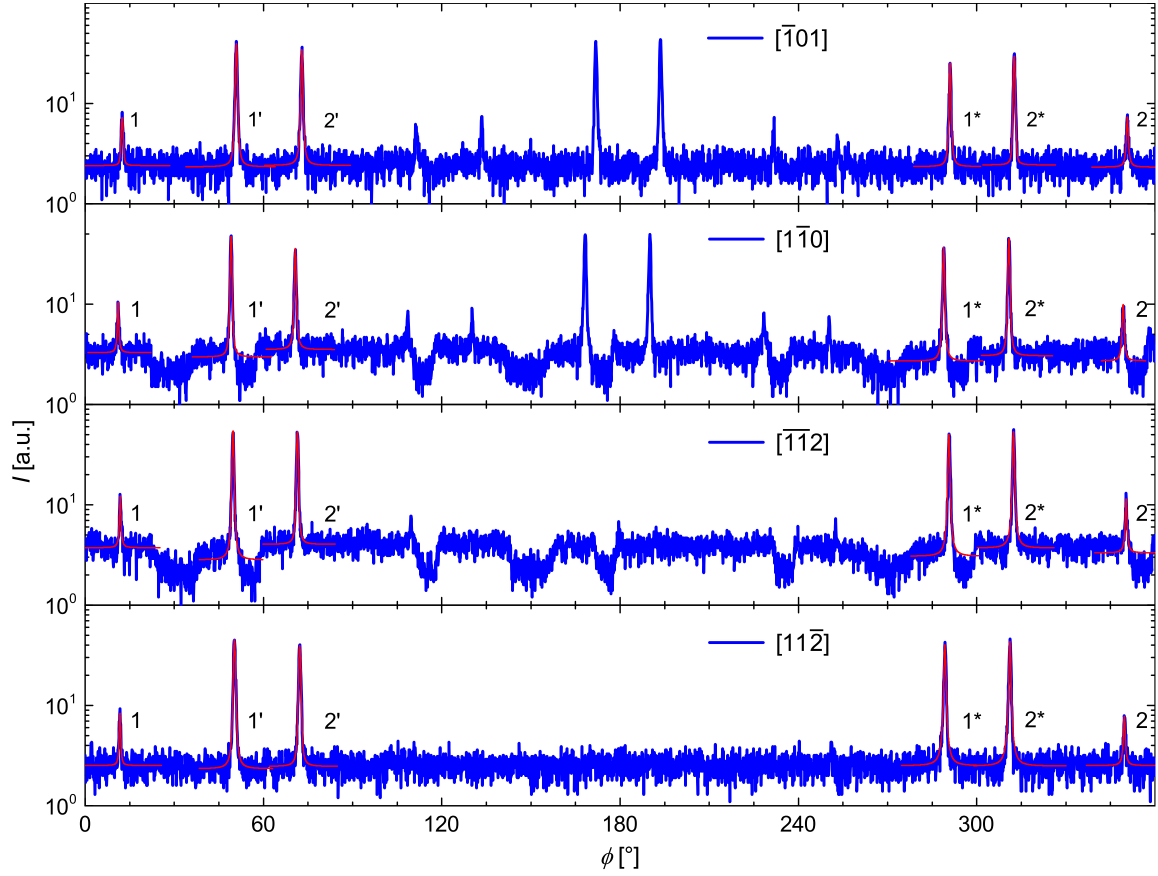

Figure 3.27: Azimuthal ϕ-scans for the family of MnSi $\{2\bar{1}0\}$ reflections of different inclinated substrates with each miscut direction indicated by the label. Different MnSi domains are marked as 1 and 2 with the stars and slashes indicating corresponding pairs of reflections.

The percentage difference of the corresponding reflections R from domain 1 and 2 shown in Fig. 3.27, meaning by what percentage the area of R_2 is smaller or bigger than the area of R_1, are displayed in Tab. 3.1. From the low values and variation in sign it is obvious that there is no significant suppression of twinning. The reason for that lies probably in the wide terrace area of the steps. The oncoming atoms are not interacting with the steps in a relevant number but instead with the normal Si(111) surface on a step terrace, which has to high symmetry making both twin domains energetically equally favorable.

This could be improved by a higher miscut angle, which leads to smaller terraces. This is closely related to the other approach discussed in the following section, which is the growth on chiral high indexed Si surfaces.

off direction	$(R_2 - R_1)/R_1$ %	$(R_{2'} - R_{1'})/R_{1'}$ %	$(R_{2^*} - R_{1^*})/R_{1^*}$ %
Si[$\bar{1}$01]	+10	-16	+23
Si[1$\bar{1}$0]	+39	-23	+20
Si[$\bar{1}\bar{1}$2]	+19	-6	+8
Si[11$\bar{2}$]	+17	-12	+10

Table 3.1: Percentage differences for the Voigt fit areas for the different reflections R shown in Fig. 3.27.

3.5.2 Growth on chiral Si surfaces

The interaction of chiral organic molecules, called enantiomers, with other chiral objects depends on the handedness of both and methods to determine or select the chirality are an ongoing field of research in chemistry and especially in pharmacy to achieve a specific interaction [Zae17]. In this field certain fcc surfaces were found to be chiral and tested for enantioselectivity. With the chiral Pt(531) surface a selection excess of $\sim$ 80% was reached quite soon after the first proposal [MCG96, AAFR99]. The idea is to impose the existing chirality of the substrate surface on the MnSi layer and by that suppressing one of the twin domains. There are a lot of different chiral surfaces with a main rule by Ahmadi *et al.* [AAFR99], that for a fcc lattice the absolute Miller indices of a chiral surface have to be unequal and non zero [JP07]. How to determine the chirality of a surface is explained in detail in the work by Pratt *et al.* [PJK05] and Jenkins *et al.* [JP07]. For epitaxial growth on the surface, it is not only important that the surface is chiral but also that it builds a stable surface. The existence of different high index Si surfaces was shown by Liu *et al.* [LT87] with field ion microscopy. The Si(135) and Si(123) surfaces (equivalent to Si(531) and Si(321)) in this work are discussed by Jenkins *et al.* [JP07] to have the possibility of {111} microfacets which we think could make the growth of MnSi possible.

Fig. 3.28 shows a side- and top-view on the [111] direction of a Si(531) substrate. The Si(531) surface is indicated by the magenta plane and the Si(111) surface by the red plane with an inclination angle of $\psi = 28.6°$ in between. The terrace edges are indicated by the different black lines and a MnSi(111) surface unit cell just fits on such a Si(111) terrace. In the same way the Si(321) substrate is shown in Fig. 3.29 with the Si(321) plane in magenta which has a $\psi = 22.2°$ angle to the Si(111) plane in red. The terraces are about 34% wider in this case.

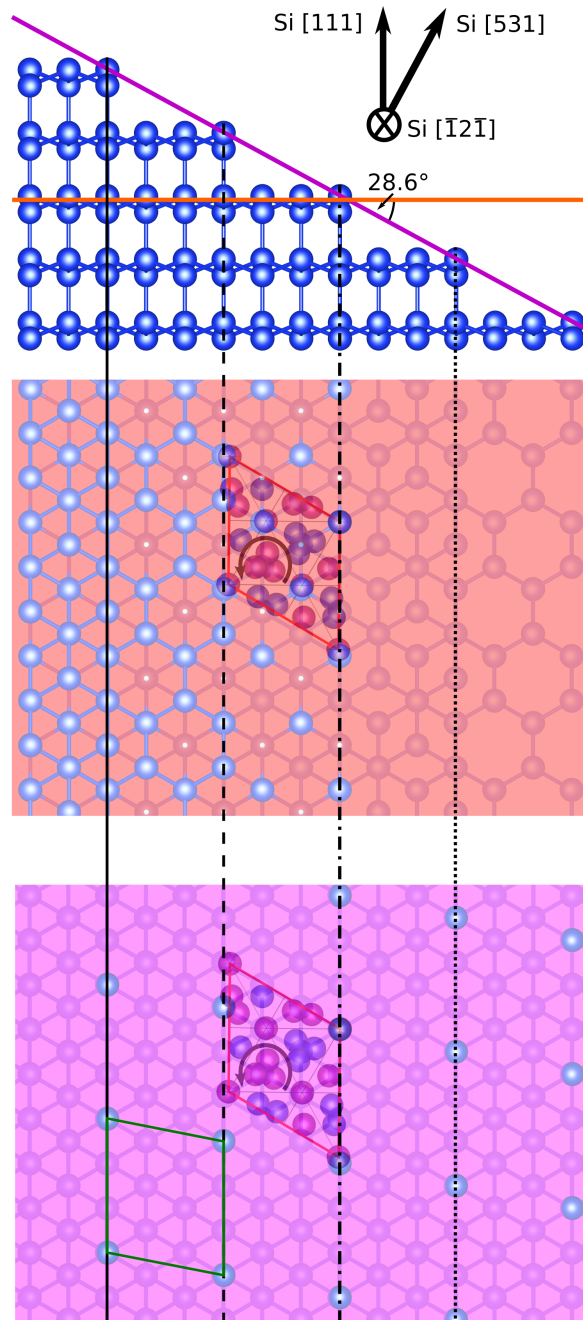

Figure 3.28: Side- and Top-view in [111] direction of Si (531) substrate. The Si (111) surface is indicated by the red plane. The Si (531) surface is indicated by the magenta plane. The Si (531) surface unit cell is indicated by the green lines. Right handed MnSi (111) surface unit cells are added as reference. Pictures of the crystal structures have been produced with Vesta 3 [MI11].

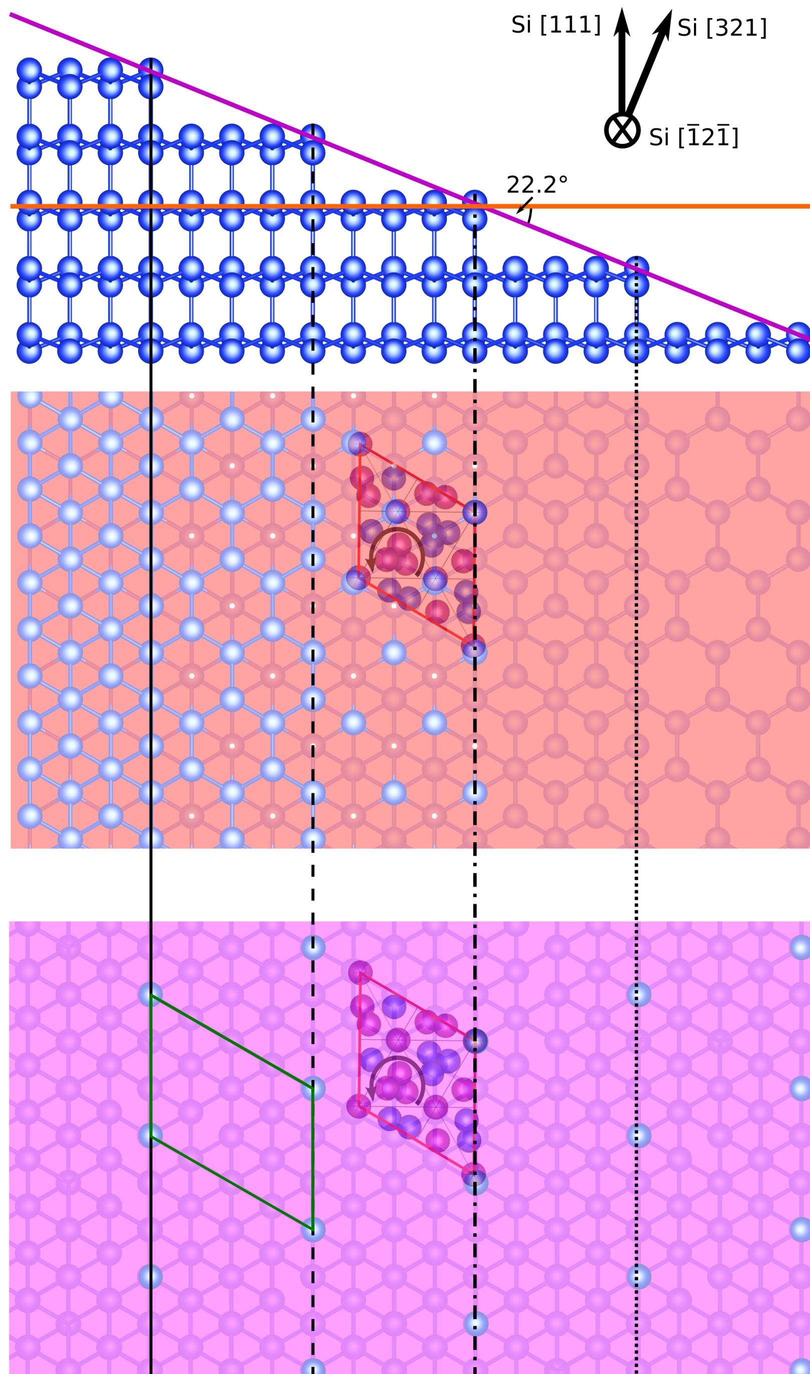

Figure 3.29: Side- and Top-view on the [111] direction of Si (321) substrate. The Si (111) surface is indicated by the red plane. The Si (321) surface is indicated by the magenta plane. The Si (321) surface unit cell is indicated by the green lines. Right handed MnSi (111) surface unit cells are added as reference.
Pictures of the crystal structures have been produced with Vesta 3 [MI11].

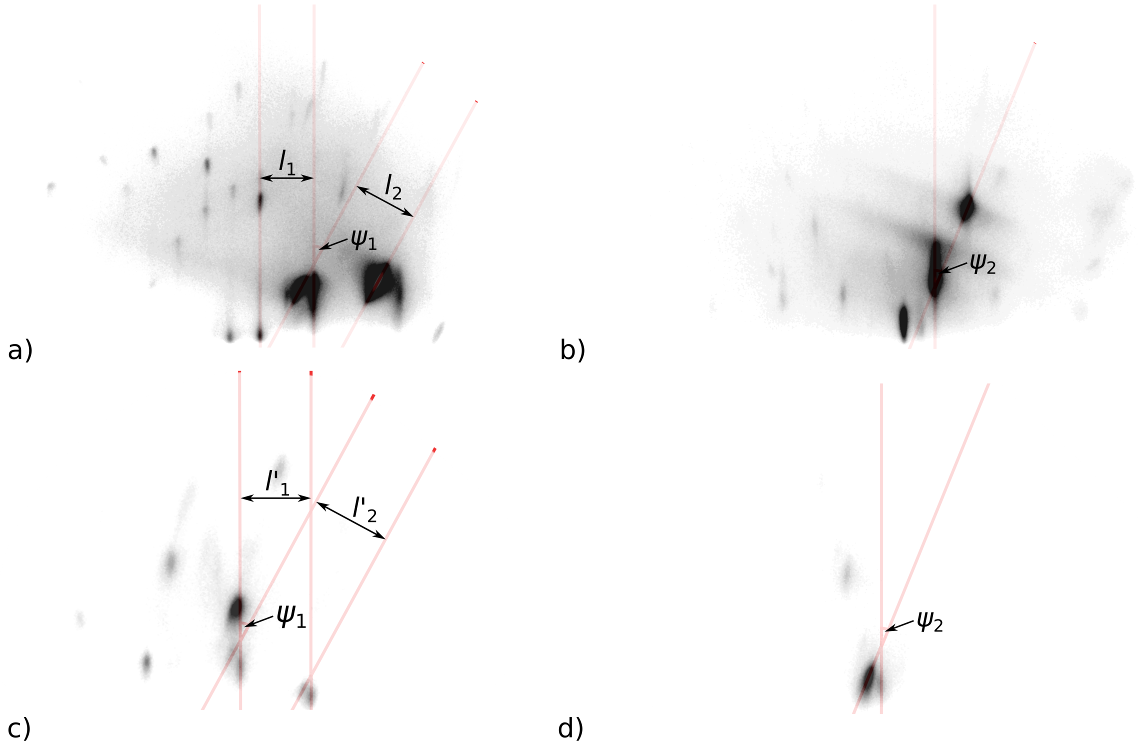

Figure 3.30: RHEED picture of the Si buffer layer on a) a Si(531) substrate and b) a Si(321) substrate.
RHEED of the MnSi layer on c) a Si(531) substrate and d) a Si(321) substrate.
Distances and angles between different reflections are indicated by the red lines. Lightness and contrast are adjusted for better visibility.

The MnSi layers are grown on these substrates with the same procedure as discussed in section 3.2 for Si(111)- with slight temperature adjustments owing to changes in the flux measured with the flux gauge. The used temperatures are $T_{\mathrm{Sub}} = 280°\mathrm{C}$ and $T_{\mathrm{Mn}} = 780°\mathrm{C}$ ($T_{\mathrm{Mn}} = 750°\mathrm{C}$ before rescaling), aiming for a MnSi layer thickness of about 26 nm and a cap layer of about 13 nm.
Fig. 3.30 a) shows the RHEED picture of the Si buffer layer on a Si(531) substrate. There are two reflections under an angle of $\psi_1 = 28.6°$, as indicated by the red lines. This indicates the existence of two surfaces and the angle is exactly the inclination angle between the Si(531) surface and the Si(111) surface. The ratio l_2/l_1 of the distance between both reflections is 1.2, which is the reciprocal ratio of the surface unit cell lattice constants of Si(111) ($a_{111} = \sqrt{2}a_{\mathrm{Si}} = 7.68\text{Å}$) and Si(531) ($a_{531} = 6.65\text{Å}$). This fits well with the expected occurrence of Si(111) terraces as displayed in Fig. 3.28.

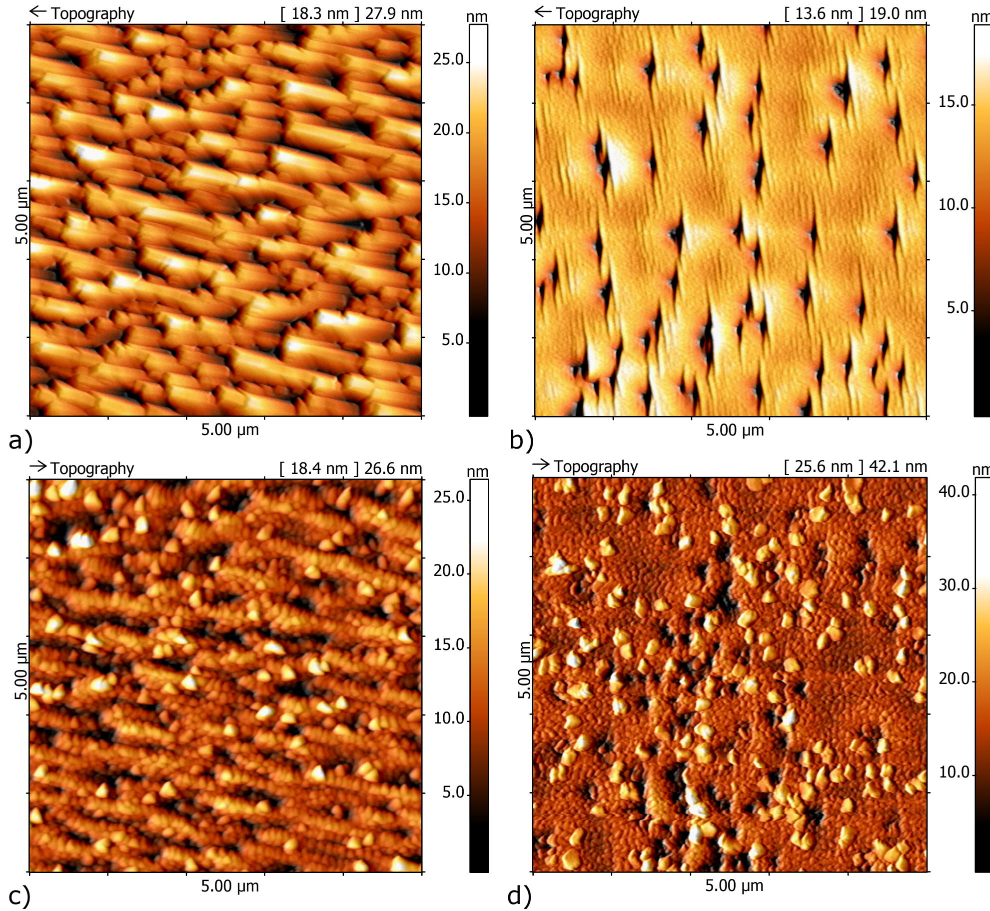

Figure 3.31: AFM of the Si buffer layer on a) a Si(531) substrate and b) a Si(321) substrate.
AFM of the MnSi layer with amorphous Si cap on c) a Si(531) substrate and d) a Si(321) substrate.

Fig. 3.30 c) shows the RHEED picture after growth of the 26 nm MnSi layer. The angle between the reflections is still $\psi_1 = 28.6°$ and the ratio of the distances is now $l'_2/l'_1 = 1.1$, almost the same as for the Si buffer shown in Fig. 3.30 a). The bigger distance in reciprocal space, as shown by the RHEED picture in Fig. 3.30 c) compared to a) could also be expected from the mismatch between Si and MnSi.
The RHEED picture of a Si buffer on Si(321) substrate is shown in Fig. 3.30 b) where the reflections appear under the expected angle of $\psi_2 = 22.2°$ between the Si(321) surface and the Si(111) surface, as indicated by the red lines. Unfortunately no two reflection pairs are visible at the same time in contrast to a), making a complete analysis as for Si(531) impossible.

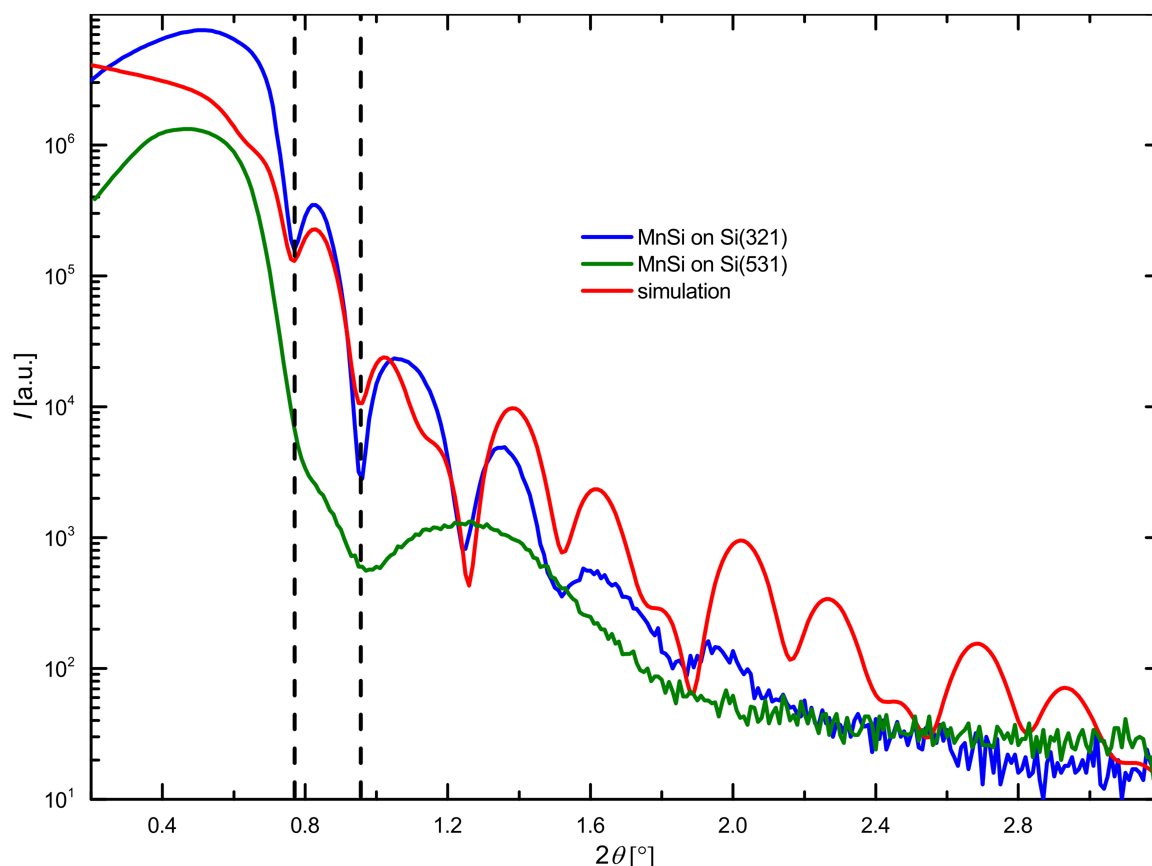

Figure 3.32: XRR measurements of the MnSi layers on Si(531) and Si(321) substrate shown in Fig. 3.31 c) and d).
XRR-simulation in red for a 25.7 nm MnSi layer with 12.9 nm Si cap layer with instrumental function and roughness ignored.

The same is true for the MnSi layer on Si(321), shown in Fig. 3.30 d) which shows the same angle between reflections. That the reflections appear under the expected angle indicates the occurrence of Si(111) terraces as displayed in Fig. 3.29.
Fig. 3.31 a) shows an AFM measurement of the Si buffer layer on a Si(531) substrate. A lot of different facet orientations are visible, but the expected angle of 28.6° between the Si(531) surface and Si(111) terraces can not be identified. There are different possible explanations. The terraces could be so small that they are not resolved, owing to a AFM tip radius of up to 10 nm, and the measured terraces are a sum of a lot of smaller ones, changing the expected terrace structure. Another possibility is the occurrence of a surface reconstruction. As the RHEED measurement resolves not only the surface but also some layers beneath the surface this could explain why the ex-

pected angle appears in the RHEED measurement but not in the AFM measurement. The AFM measurement of a MnSi layer with amorphous Si cap on a Si(531) substrate is shown in Fig. 3.31 c). The same facet structure as for the Si buffer layer shown in Fig. 3.31 a) is visible even with the amorphous cap layer, indicating that the faceting does not appear because of influences outside the chamber.
Fig. 3.31 b) shows an AFM measurement of a Si buffer on a Si(321) substrate. Here only one surface is visible together with deep trenches and as before, the expected angle of 22.2° between the Si(321) surface and Si(111) terraces can not be identified. The explanation is probably the same as for the Si(531) substrate, as the topography is also visible after MnSi layer and amorphous Si cap growth. This is shown in Fig. 3.31 d) where the deep trenches are visible again.
To determine the layer thickness XRR measurements and simulations, as discussed in chapter 2.2.3, are used. For the MnSi layer on Si(321) substrate the measurement and simulation fit quite well, as shown in Fig. 3.32. The layer thickness of about 26 nm determined by the XRR-simulation is the same as for a previously grown layer on Si(111) with the same growth time, which proofs the same growth rates on Si(111) and Si(321) substrates. For the MnSi layer on Si(531) substrate, shown as the green line in Fig. 3.32, one fringe corresponding to the same layer thickness of 26 nm is visible, as indicated by the dashed black lines. As the growth conditions and time are the same for both layers the same thickness will be used for further analysis, assuming that the growth rate is the same on Si(111), Si(321) and Si(531). The difficulties on Si(531) probably result from the stepped and tilted surface of the layer in comparison to Si(321) as shown by the AFM measurements in Fig. 3.31.
Structural characterization by XRD measurements is difficult for both of these substrates. For the Si(531) substrate the symmetric 531 MnSi reflection is not measurable as the diffraction angle 2θ is 175.7° which is not reachable. For the Si(321) substrate the symmetric 321 Si reflection has no intensity as the structure factor, as given in Eq. 2.8, is zero because of the mixed even and odd Miller indices.
Because of that, XRD characterization is focused on twin identification via azimuthal ϕ-scans. As the different reflections of a family like {210} do not have the same inclination angle to the Si(321) and Si(531) surface in contrast to Si(111), the inclination angle ψ has to be varied as well.

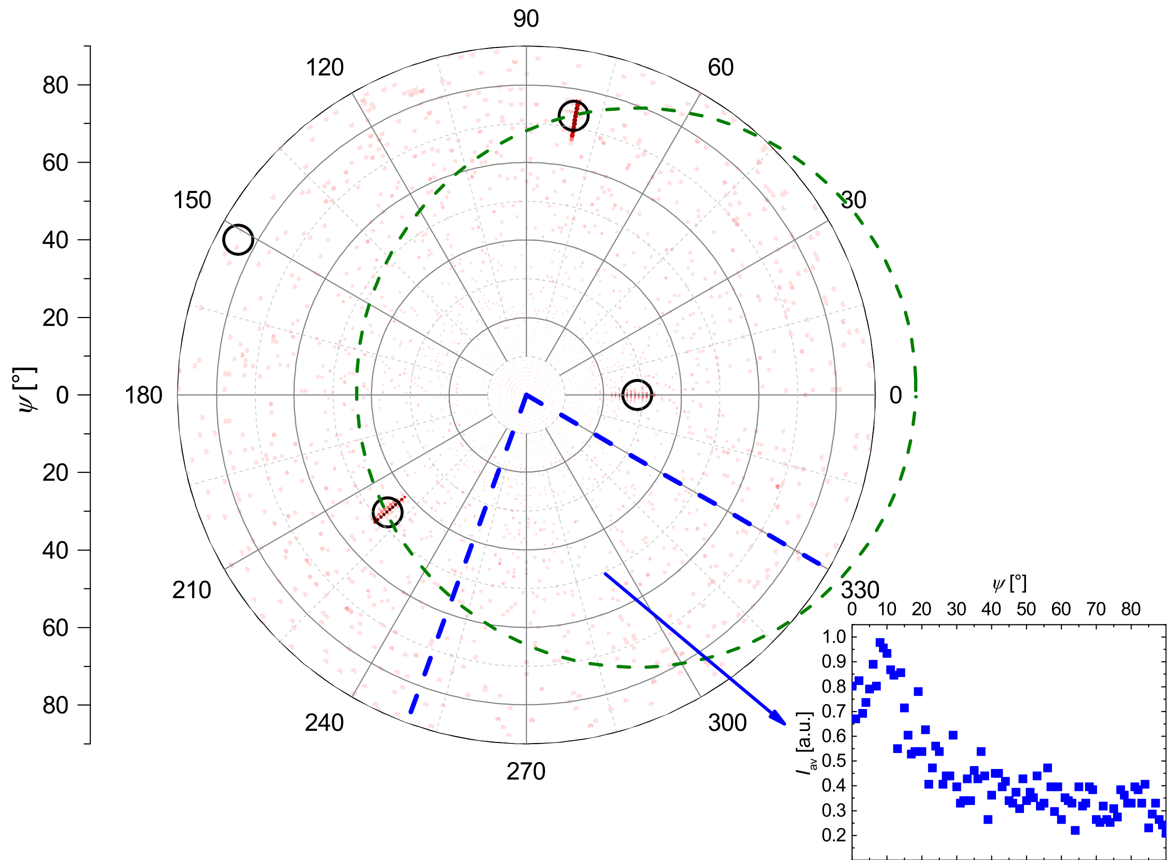

Figure 3.33: Polar plot of azimuthal ϕ-scans for varied inclination angle ψ of the Si $\{111\}$ reflections on Si(531) substrate. A darker red corresponds to a higher intensity. $\phi = 0°$ as the direction of the 111 reflection. The black circles indicate the nominal positions of reflections. The dashed green circle connects reflections from planes with the same inclination angle with respect to the Si 111 plane. The inset shows the intensity of the diffuse background depending on inclination angle ψ averaged over the indicated slice in ϕ by the dashed blue lines.

Fig. 3.33 a) shows the polar plot of azimuthal ϕ-scans for varied inclination angle ψ of the Si {111} reflections on Si(531) substrate. Three peaks are visible, with a darker red corresponding to a higher intensity . At $\phi = 0°$ is the Si 111 reflection and this orientation is used for all further polar plots. The green dashed circle connects the reflections $1\bar{1}1$ at $\phi \approx 80°$ and $11\bar{1}$ at $\phi \approx 220°$ from planes with the same inclination angle with respect to the Si 111 plane. The black circles show nominal reflection positions with the ψ positions calculated according to Eq. 2.5 with surface normal $[mno] = [531]$ and the ϕ positions calculated according to Eq. 2.6 and Eq. 2.7 with the projection of $[abc] = [111]$ on the surface as the reference direction. This results in another expected reflection at $\phi \approx 152°$ and $\psi \approx 84°$, as shown in Fig. 3.33, which is not visible. A possible explanation for that is the decrease of intensity with increasing ψ, as shown in Fig. 3.33. Here the background intensity is averaged in ϕ over the slice indicated by the dashed blue lines in Fig. 3.33, showing a decrease with increasing ψ. This shows that it is important to compare intensities of reflections with similar ψ values. The other nominal reflections match the experimental peak positions quite well with a smear out of intensity along the psi direction that probably comes from the measurement geometry and setup.
Fig. 3.34 a) shows the same measurement as Fig. 3.33 but for the MnSi {111} reflections. Here black circle and blue cross mark the nominal positions for twin domain 1 and 2 calculated with Eq. 2.5, 2.7 and 2.6 after applying a $\pm 30°$ rotation around the [111] direction and for one of the domains a mirror operation at the $(\bar{1}10)$ plane. This means the connection between the twin domain is the same as described in section 3.4 for Si(111) substrates. The labels next to the nominal positions mark the maximum intensity found in this ϕ/ψ area. Because the intensities in comparison to the background are very low, proper Voigt-fits to determine the peak area can not be applied. This makes this measurement difficult to use for comparison of the volumes of the twin domains. The measurement nevertheless can be used to show that the measured peaks are at the positions expected from calculations. The intensity is again reduced with higher ψ.
Fig. 3.37 b) shows the measurement for the MnSi {210} reflections. Here the reflections have different calculated intensities indicated by the size of the black circles and blue crosses. The smaller green dashed circle connects the {210} reflections, where a high intensity reflection from one twin is at the same position as a high intensity reflection of the other twin and the same for the low intensity reflections.

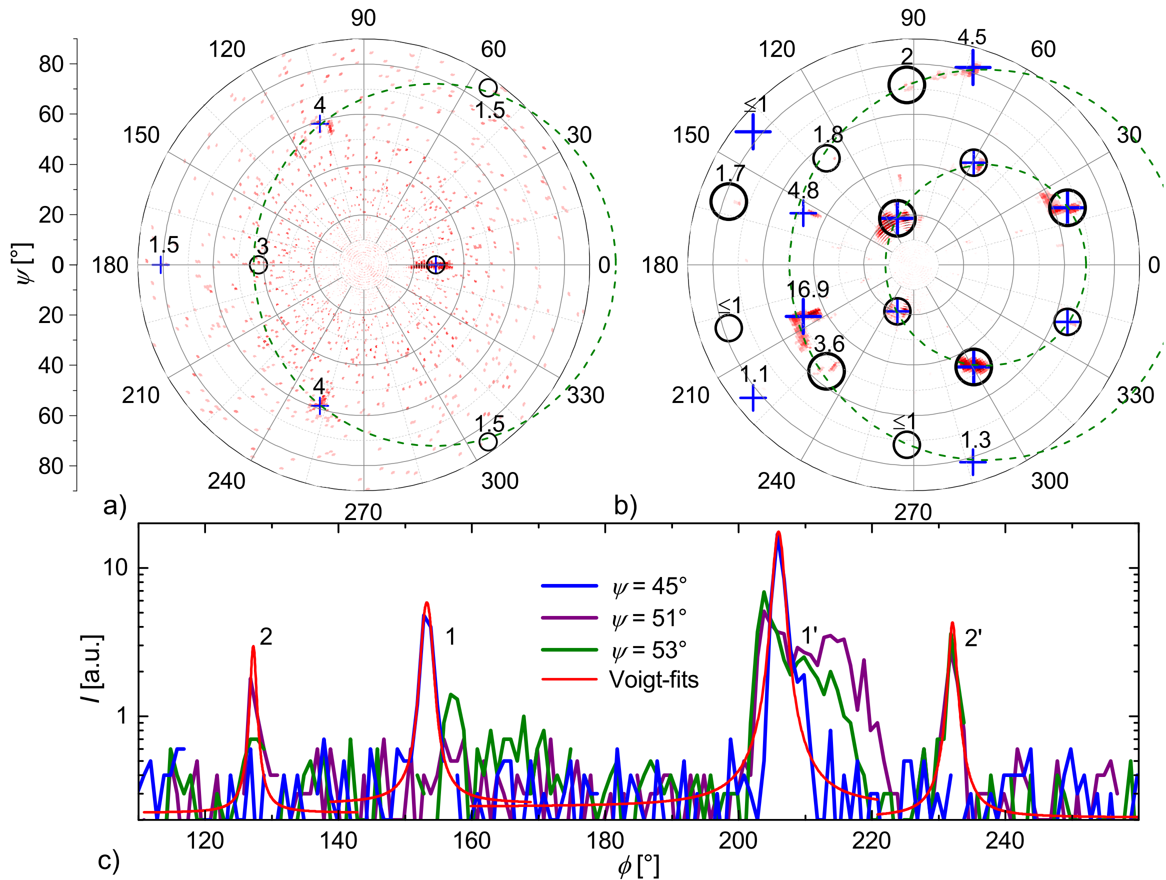

Figure 3.34: Polar plot of azimuthal ϕ-scans for different ψ of a) the MnSi {111} reflections and b) the MnSi {210} reflections of an MnSi layer on Si(531) substrate. A darker red corresponds to a higher intensity. $\phi = 0°$ as the direction of the 111 reflection. The black circles and blue crosses indicate the nominal positions of reflections and twin reflections. The labels at the reflections indicate the maximum intensity. The dashed green circles connects reflections from planes with the same inclination angle with respect to the 111 plane.
c) Azimuthal ϕ-scans for three ψ values from b) with Voigt fits.

The bigger green dashed circle connects the $\{2\bar{1}0\}$ reflections, where the reflections from each twin are at different positions. Some of the reflections are pretty close in ψ and ϕ which makes them perfect to compare the volume fraction. The peak intensities are high in comparison to the background and Voigt fits are used to determine the peak area, as shown in Fig. 3.34 c). From the peak areas a percentage difference of $(R_2 - R_1)/R_1 \approx -69\%$ and -81% for reflection $R_{2'}$ to $R_{1'}$ can be determined, meaning that the area of $R_{2'}$ is 81% smaller than the area of $R_{1'}$. Considering the uncertainty caused by the low intensities of R_1 and R_2, a high twin suppression of about 81% can be assumed.

The polar plot in Fig. 3.34 b) also shows broadening and sometimes even more than one peak in ϕ and ψ. This indicates strong mocaicity twist and tilt of the twin domains. XRD instrumental broadening can be excluded because the Si reflections are well defined.

Fig. 3.35 a) shows a polar plot of the Si{111} reflections on Si(321) substrate. The nominal positions shown by the black circles are again calculated according to Eq. 2.5, Eq. 2.6 and Eq. 2.7 with the $\pm 30°$ rotation and $(\bar{1}10)$ mirror plane and fit well with the observed positions.

Fig. 3.35 b) shows the corresponding MnSi{111} reflections. Again the black circle and the blue cross represent the calculated positions and reflections at high ψ seem to be suppressed by the instrumental effect shown in the inset of Fig. 3.33. The agreement between nominal and experimental positions shows that the twinning mechanism is the same as described in section 3.4. The green dashed line connects reflections from planes with the same inclination to the (111) plane and the reflections at $\phi \approx 110°$, $\phi \approx 180°$ and $\phi \approx 250°$ can be used to compare the volume fraction of the two twin domains.

Fig. 3.35 c) shows the corresponding azimuthal ϕ-scans for these peaks with Voigt-fits to determine the peak area. The peak area of reflection R_2 is about 81% smaller than the average peak area of reflection R_1 and $R_{1'}$, indicating a strong suppression.

Fig. 3.36 a) shows the polar plot of azimuthal ϕ-scans for different ψ of the Si {220} reflections of an MnSi layer on Si(321) substrate. The calculated positions marked by the black circles correspond pretty well to the measured peaks. This is also true for Fig. 3.36 b) which shows the corresponding measurement of the MnSi reflections. As the ψ values for the equivalent reflections on the smaller green dashed ring are quite different, it is difficult to compare them directly.

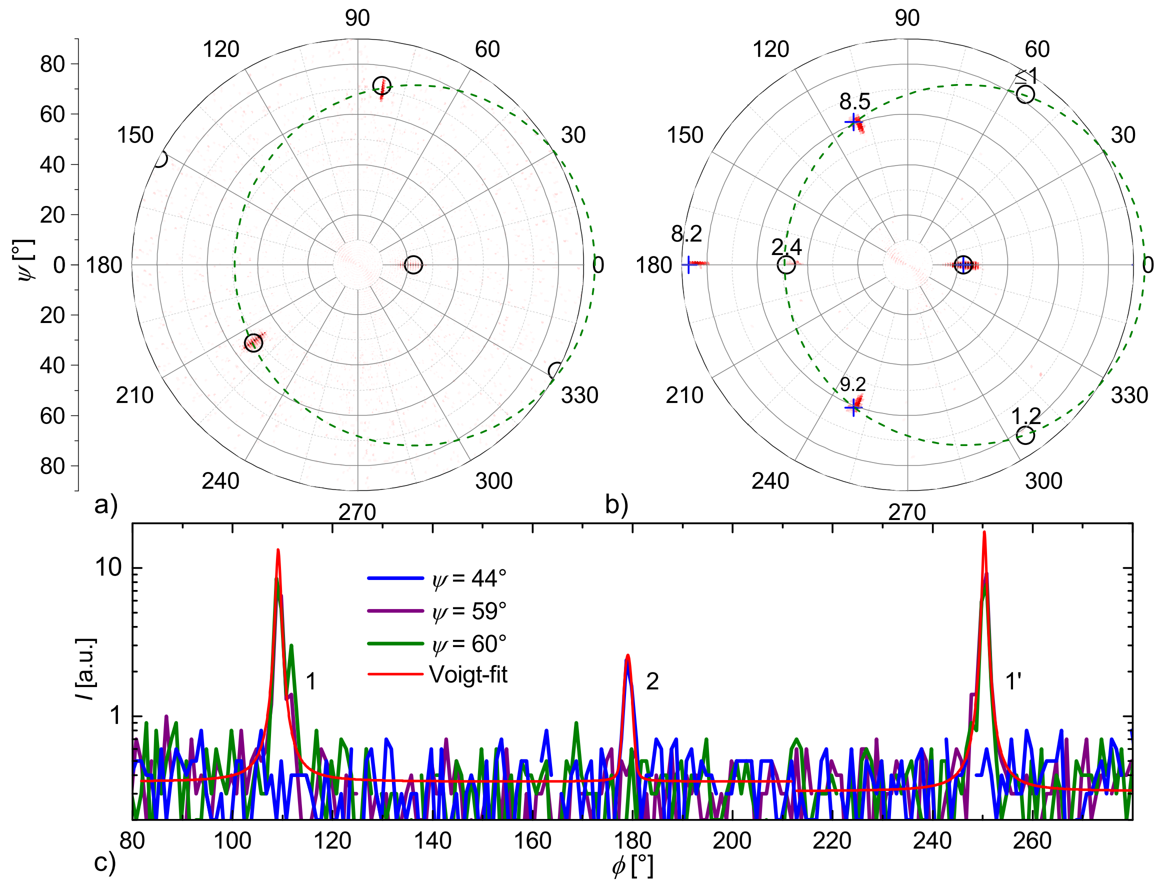

Figure 3.35: Polar plot of azimuthal ϕ-scans for different ψ of a) the Si {111} reflections and b) the MnSi {111} reflections of an MnSi layer on Si(321) substrate. A darker red corresponds to a higher intensity. $\phi = 0°$ as the direction of the 111 reflection. The black circles and blue crosses indicate the nominal positions of reflections and twin reflections. The labels at the reflections indicate the maximum intensity. The dashed green circles connect reflections from planes with the same inclination angle to the 111 plane.
c) Azimuthal ϕ-scans for three ψ values from b) with Voigt-fits.

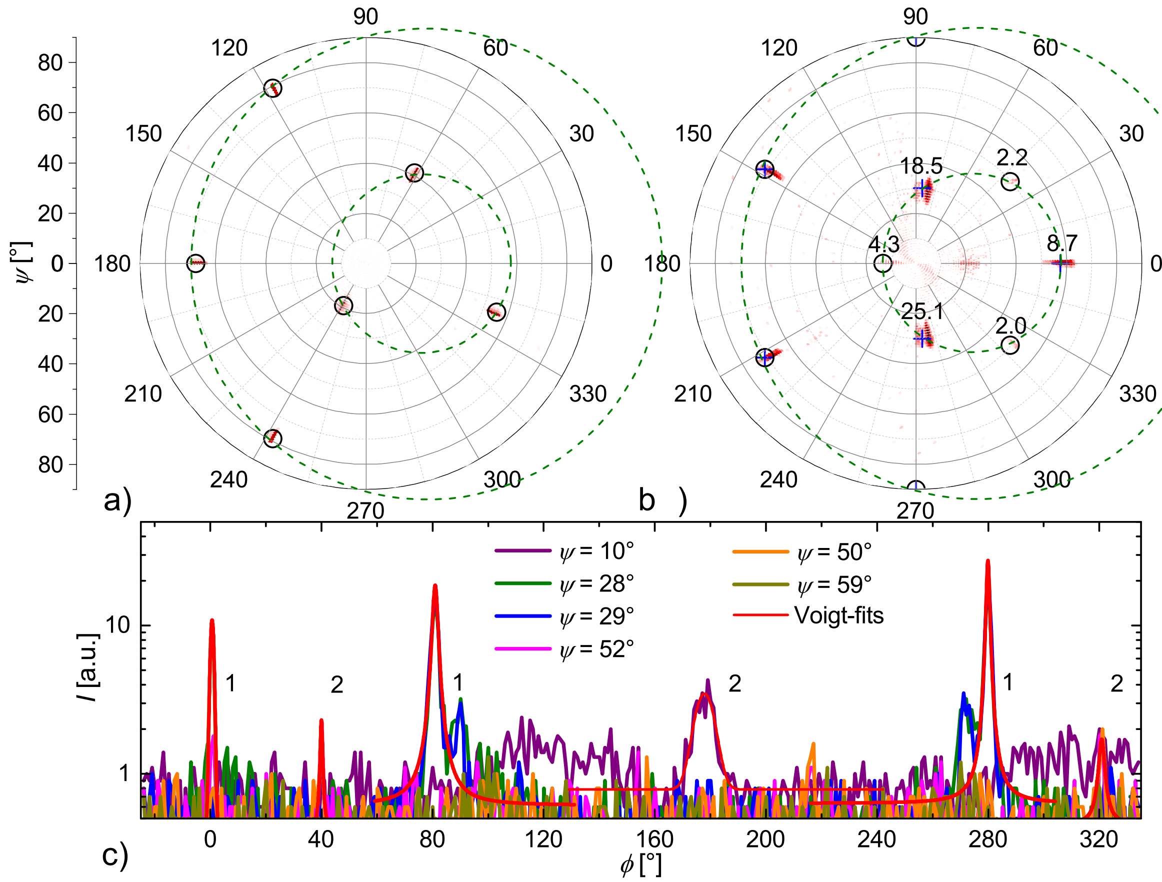

Figure 3.36: Polar plot of azimuthal ϕ-scans for different ψ of a) the Si {220} reflections and b) the MnSi {220} reflections of an MnSi layer on Si(321) substrate. A darker red corresponds to a higher intensity. $\phi = 0°$ as the direction of the 111 reflection. The black circles and blue crosses indicate the nominal positions of reflections and twin reflections. The labels at the reflections indicate the maximum intensity. The dashed green circles connect reflections from planes with the same inclination angle to the 111 plane.
c) azimuthal ϕ-scans for six ψ values from b) with Voigt-fits.

Instead the average of the low intensity twin reflections, marked by the black circles, is compared to the average of the high intensity twin reflections, marked by the blue crosses. The azimuthal ϕ-scans together with the Voigt-fits used to determine the peak area are shown in Fig. 3.36 c). The average peak area of the low intensity twin reflections is about 78% smaller than the average peak area of the high intensity twin reflections. This is consistent with the 81% determined by the 111 reflections. Fig. 3.37 a) shows a polar plot of the MnSi{210} reflections on Si(321) substrate.

The reflections used to compare the peak areas with azimuthal ϕ-scans and Voigt fits are shown in Fig. 3.37 b). Here the area of peak R_2 is about 93% smaller than the area of peak R_1 and the area of peak $R_{2'}$ about 89% smaller than the area of peak $R_{1'}$. The polar plot in Fig. 3.37 a) also shows broadening and sometimes even more than one peak in ϕ and ψ, but way less pronounced than for Si(531) substrate. This is consistent with the smoother surface of MnSi layers on Si(321) substrate, as observed in AFM measurements (Fig. 3.31).

In conclusion, chiral Si(531) and Si(321) substrates show a broadening in ϕ and ψ indicating mocaicity twist and tilt. The twinning of the MnSi layers happens with the same $\pm 30°$ rotation and mirror operation at the $(\bar{1}10)$ plane as on Si(111), but a high twin suppression is demonstrated. For the (531) substrate the twin suppression is in the range of 69% to 81% and for the (321) substrate in the range of 78% to 93%.
The following chapter will discuss the magnetic characteristics of MnSi layers on Si(111) and also compare them to the twin suppressed layers on chiral substrates.

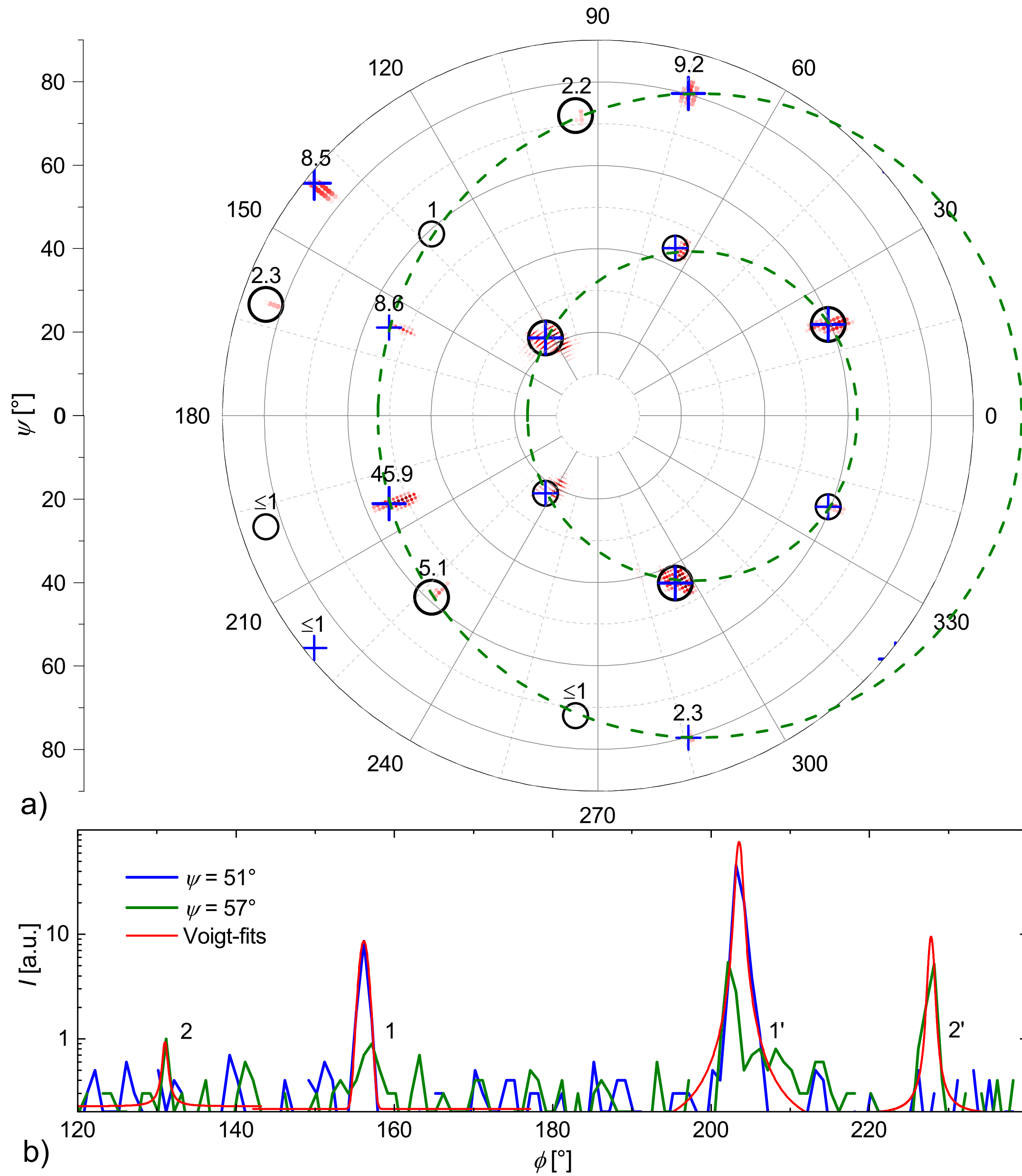

Figure 3.37: a) Polar plot of azimuthal ϕ-scans for different ψ of the MnSi {210} reflections of an MnSi layer on Si(321) substrate. A darker red corresponds to a higher intensity. $\phi = 0°$ as the direction of the 111 reflection. The black circles and blue crosses indicate the nominal positions of reflections and twin reflections. The labels at the reflections indicate the maximum intensity. The dashed green circles connect reflections from planes with the same inclination angle with respect to the 111 plane.
b) Azimuthal ϕ-scans for two ψ values from a) with Voigt-fits.

4 Magnetic characterization of MnSi

As discussed in section 2.3, MnSi exhibits an interesting and rich magnetic phase diagram with critical magnetic field and temperature boundaries to a field-polarized or paramagnetic region. The basic characterization of these magnetic properties is done especially to determine this critical boundaries and to search for influence of the twinning on transport properties. In the following section the magnetic properties determined by SQUID magnetometer measurements will be explained, followed by a section on the magnetotransport properties.

4.1 Magnetometry

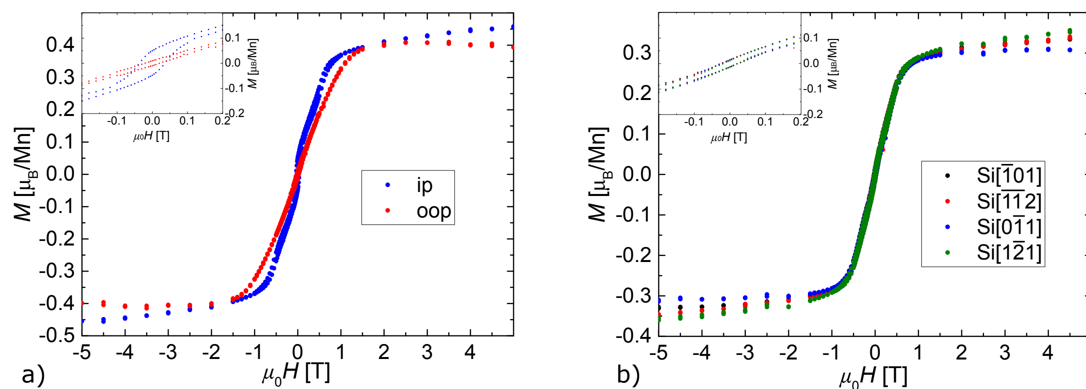

Figure 4.1: a) Magnetization of the 20 nm layer at $T = 1.8$ K for a magnetic field in the layer plane and perpendicular to the layer plane. The inset shows the remanent magnetization region.
b) Magnetization of the 32 nm layer at $T = 1.8$ K for the in plane magnetic field along different Si directions. The inset shows again the remanent magnetization region.

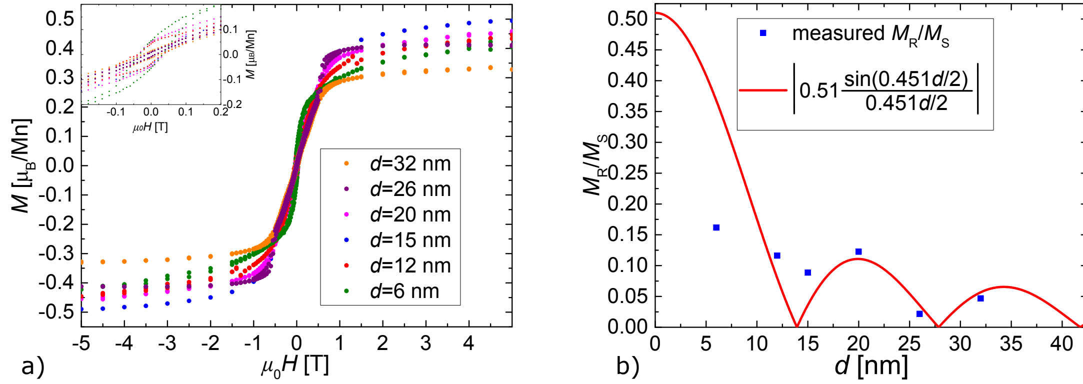

Figure 4.2: b) Magnetization of layers with different thickness at $T = 1.8$ K for in plane magnetic field. The inset shows the remanent magnetization region. b) Remanent versus saturation magnetization from a) with a simulated behavior according to Karhu *et al.* [KKM+10, KKR+11]

Fig. 4.1 a) shows hysteresis measurements at $T = 1.8$ K of the 20 nm thick layer. Red dots shows the measurement with the magnetic field perpendicular to the layer plane, and blue dots in the layer plane. From the unexpected difference above $\mu_0 H =$ 1 T one can see the problem in determining absolute values correctly, as discussed in section 2.4.1. The inset shows the measurement around zero magnetic field where the in plane measurement shows a clear remanent magnetization. Both curves have a similar form to what was shown before for SPE and MBE grown layers, which is explained by an in plane helical spin spiral propagation vector perpendicular to the layer plane [KKM+10, KKR+11]. The remanent magnetization in the perpendicular measurement stems probably from an in plane magnetic field caused by misalignment. Fig. 4.1 b) shows the magnetic moment of the 32 nm layer discussed in section 3.3 for an in plane magnetic field aligned along different Si crystal directions in steps of 30°. In Fig. 4.1 b) the remanent magnetization region is again displayed in the inset. Compared to the difference between magnetic field in the layer plane and perpendicular to it, the difference between the curves here can all be explained by the error in background determination. The remanent magnetization compared with Fig. 4.1 a) is smaller, indicating a thickness dependence, which would be expected for a spin helix propagating perpendicular in layers with varying thickness [KKM+10, KKR+11].

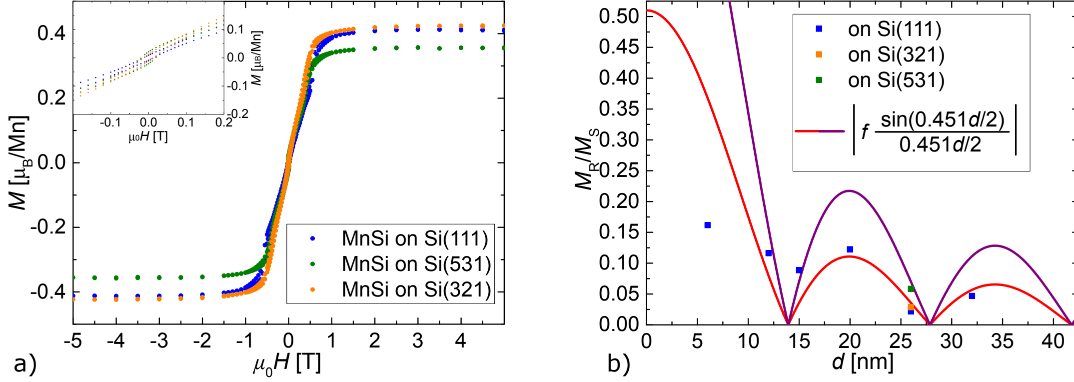

Figure 4.3: b) Magnetization of about 26 nm MnSi layers on different substrates at $T = 1.8$ K for an in plane magnetic field. The inset shows the remanent magnetization region.
b) Remanent versus saturation magnetization from a) and Fig. 4.2 a) with a simulated behavior according to Karhu *et al.* [KKM+10, KKR+11]. $f = 0.51$ for the red curve and $f = 1$ for the purple curve.

Fig. 4.2 a) shows the in plane measurements for the thickness series discussed in section 3.3 and the 26 nm layer from the sample series discussed in 3.2.3, with the remanent magnetization region displayed in the inset. The saturation magnetization, determined by a linear fit to the $\mu_0 H = 3 - 5$ T region as described by Karhu *et al.* [KKM+10], fluctuates around 0.4 μ_B/Mn, which is the spontaneous magnetization expected from bulk MnSi [WWSW66].
Fig. 4.2 b) shows the ratio of remanent magnetization M_R, taken at $\mu_0 H = 0$ T and decreasing field, and saturation magnetization M_S from a) as blue squares depending on layer thickness. The red curve is a simulation describing the remanent magnetization behavior of a helical magnet with pitch vector Q perpendicular to layers with thickness d [KKM+10, KKR+11]

$$\frac{M_R}{M_S} = |f \frac{\sin(Qd/2)}{Qd/2}| \tag{4.1}$$

where the scaling factor f represents magnetic domains with $f = 1$ for a single domain. As the thickness series has not enough samples to fit this equation the simulation is done with the values from Karhu *et al.* [KKR+11] which are not contradicted by the measurement. The pitch vector corresponds to a wavelength of $2\pi/Q = 13.9$ nm and the scaling factor $f = 0.51$ to a system with two magnetic domains, which is expected

from the mirror twinning discussed in the previous chapter.
This analysis could then be used to verify the twin suppression discussed in section 3.5.2. To compare the magnetic behavior of MnSi on Si(111) substrate to the one on Si(531) and Si(321), their magnetization measurements at $T = 1.8$ K, adjusted in the same way as discussed before, are shown in Fig. 4.3 a). The MnSi on Si(111) measurement is from the 26 nm layer also shown in Fig. 4.2 and the MnSi on Si(531) and MnSi on Si(321) are the 26 nm layers discussed in section 3.5.2.
The magnetization curves shown in Fig. 4.3 a) are similar but vary in M_S and M_R, as expected from Eq. 4.1 for a different f by twin suppression. The $M_\mathrm{R}/M_\mathrm{S}$ ratio of these layers together with the previous results is shown in Fig. 4.3 b). Additionally simulation of Eq. 4.1 with a scaling factor $f = 1$ according to full twin suppression is shown in purple. Both layers on the chiral substrates show a increase of the $M_\mathrm{R}/M_\mathrm{S}$ ratio as expected. Curiously the increase for the MnSi on Si(531) layer is bigger even if that layer is showing slightly less twin suppression in the XRD measurements. In conclusion this measurement method could be used as an additional method to prove the twin suppression.
Magnetization measurements can also be used to determine the critical field to saturate the layer. As most transport measurements shown in later sections are done at $T = 4.2$ K, Fig. 4.4 a) shows the magnetization measurement of the 32 nm layer in blue with an in plane magnetic field applied in regular steps at this temperature. The inset shows the full curve with some dips at around $\pm\mu_0 H = 3$ T. This is where the measurement without background adjustment goes trough zero and is an artifact from the way the SQUID software is trying to fit an almost nonexistent measurement signal [SSN11]. The minimum in the second derivative, shown in red for decreasing magnetic fields, is used to determine a critical field of about $\mu_0 H_\mathrm{c1} = 0.6$ T, which is the same as the bulk value and slightly below the 0.8 T value for a 36 nm layer in literature [WWSW66, KRB+12].
So far all magnetization measurements concerning MnSi were shown below the Curie temperature T_C, above which the layers become paramagnetic. To determine this temperature, the temperature dependent static susceptibility $\chi = M/H$ for a magnetic field $\mu_0 H = 0.4$ T is used, as shown in Fig. 4.4 b) for the same 32 nm layer adjusted with Eq. 2.14.

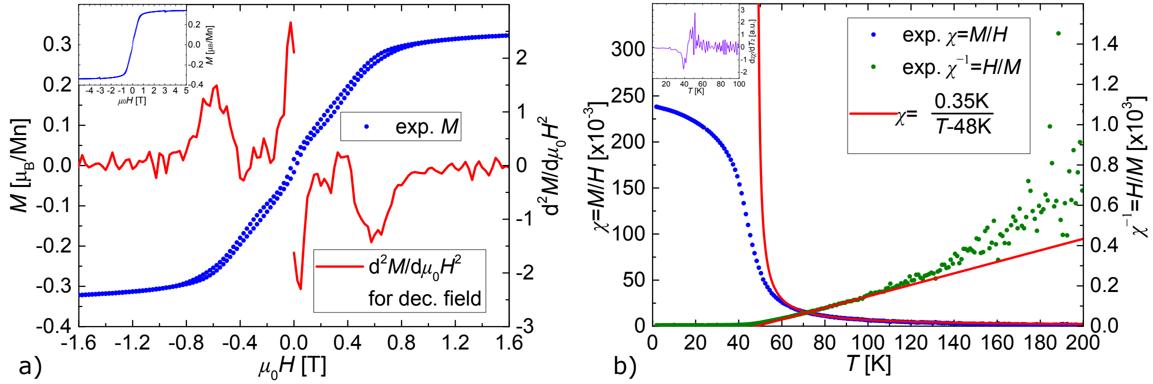

Figure 4.4: a) Magnetization of the 32 nm layer at $T = 4.2$ K for an in plane magnetic field in blue together with the second derivative in red. The inset shows the full hysteresis curve.
b) Temperature dependent static susceptibility $\chi = M/H$ and inverse static susceptibility $\chi^{-}1 = H/M$ at $\mu_0 H = 0.4$ T for the same layer as shown in a). Fit of Eq. 4.2 in red to the inverse susceptibility between $T = 70$ K and $T = 100$ K. The inset shows the second derivative of the interpolated susceptibility.

Above the Curie-Weiss temperature θ_p the susceptibility is expected to follow the Curie-Weiss law [Coe10]

$$\chi = \frac{C}{T - \theta_p} \tag{4.2}$$

with the Curie constant C.
The Curie-Weiss law is used to fit the inverse susceptibility between $T = 70$ K and $T = 100$ K, where it shows a linear dependence and is below the temperature region where thermal fluctuations dominate the measurement as can be seen in Fig. 4.4 b). At higher temperatures the susceptibility approaches zero and the inverse susceptibility fluctuates strongly. Nevertheless a systematic shift to higher values than the linear fit is visible, which could indicate that the Curie-Weiss temperature is even higher than the one from the fit. The Curie-Weiss temperature $\theta_p = 48$ K from the fit is considerably above the 30 K of bulk MnSi [WWSW66]. This increase could be induced by the residual strain, as previously pointed out by Karhu *et al.* [KKM+10] and is slightly above the $T_C \approx 40$ K determined by them with power law fits to the low temperature region of SPE grown 10 nm to 20 nm MnSi layers. Another method, commonly used in Geophysics to determine the Curie temperature, is the point of

maximum curvature in the magnetization [FSM13].
This can be determined by the maximum in the second derivative of the static susceptibility, shown in the inset of Fig. 4.4 b) and gives about $T_{c1} = 49$ K, so about the same value as θ_p. The minimum in the second derivative would be equivalent to the crude determination of the Curie temperature of MnSi by Dhital *et al.* [DKS$^+$17], who propose T_c to be the midpoint of the decreasing first derivative of the susceptibility. This gives a critical temperature of about $T_{c2} = 39$ K, consistent with the aforementioned results determined from the low temperature region.
The Curie constant C from the fit of Eq. 4.2 can be used to determine an effective moment m_{eff} with [Coe10]

$$C = \frac{\mu_0 n m_{\text{eff}}^2}{3k_{\text{B}}} \tag{4.3}$$

and the number n of Mn atoms per unit cell volume. With $C = 0.35$ K and the CODATA recommended constants this results in $m_{\text{eff}} = 1.8\ \mu_{\text{B}}/\text{Mn}$ [MNT16]. To compare it to the saturation moment of $q_s \approx 0.33\ \mu_{\text{B}}/\text{Mn}$ determined by the intercept of a linear fit to the $3.5 - 5$ T region for decreasing field in Fig. 4.4 a) it has to be recalculated with [Woh78]

$$m_{\text{eff}}^2 = q_c\,(q_c + 2)\ \ . \tag{4.4}$$

This results in $q_c = 1.0\ \mu_{\text{B}}/\text{Mn}$, which is comparable to the bulk value of $1.4\ \mu_{\text{B}}/\text{Mn}$ [WWSW66]. That q_c is bigger than q_s is a result of the conical spin structure below T_{C} [Woh78].
Fig. 4.5 a) shows the magnetization at $T = 4.2$ K for the 26 nm MnSi layer on Si(531) substrate and the second derivative of decreasing field measurements. The first minimum in the derivative again indicates a critical field $\mu_0 H_{c1}$ of about 0.6 T. Fig. 4.5 b) shows the temperature dependence for the magnetization of the same layer as in a) at $\mu_0 H = 0.4$ T, so just below the critical field. The fit of the Curie Weiss law shown in red reveals a Curie constant of $C = 0.34$ K and a Curie-Weiss temperature of $\theta_p = 47$ K, both almost the same as for the sample on Si(111) substrate shown before. The inset again shows the second derivative from which the critical temperatures can be estimated to about $T_{c1} = 46$ K and $T_{c2} = 36$ K.
Fig. 4.5 c) shows the magnetization at $T = 4.2$ K for the 26 nm MnSi layer on Si(321) substrate as well as the second derivative to the decreasing field measurements. The first minimum in the derivative indicates a critical field $\mu_0 H_{c1}$ of about 0.5 T, close to the previously determined critical fields. Fig. 4.5 d) shows the temperature

dependence for the magnetization of the same layer as in c) at $\mu_0 H = 0.4$ T, again just below the critical field. The bump at around $T = 50$ K could be explained by a difference in measured temperature and actual temperature at the sample. The fit of the Curie Weiss law shown in red reveals a Curie constant of $C = 0.41$ K and a Curie-Weiss temperature of $\theta_p = 48$ K again similar to the values determined before.

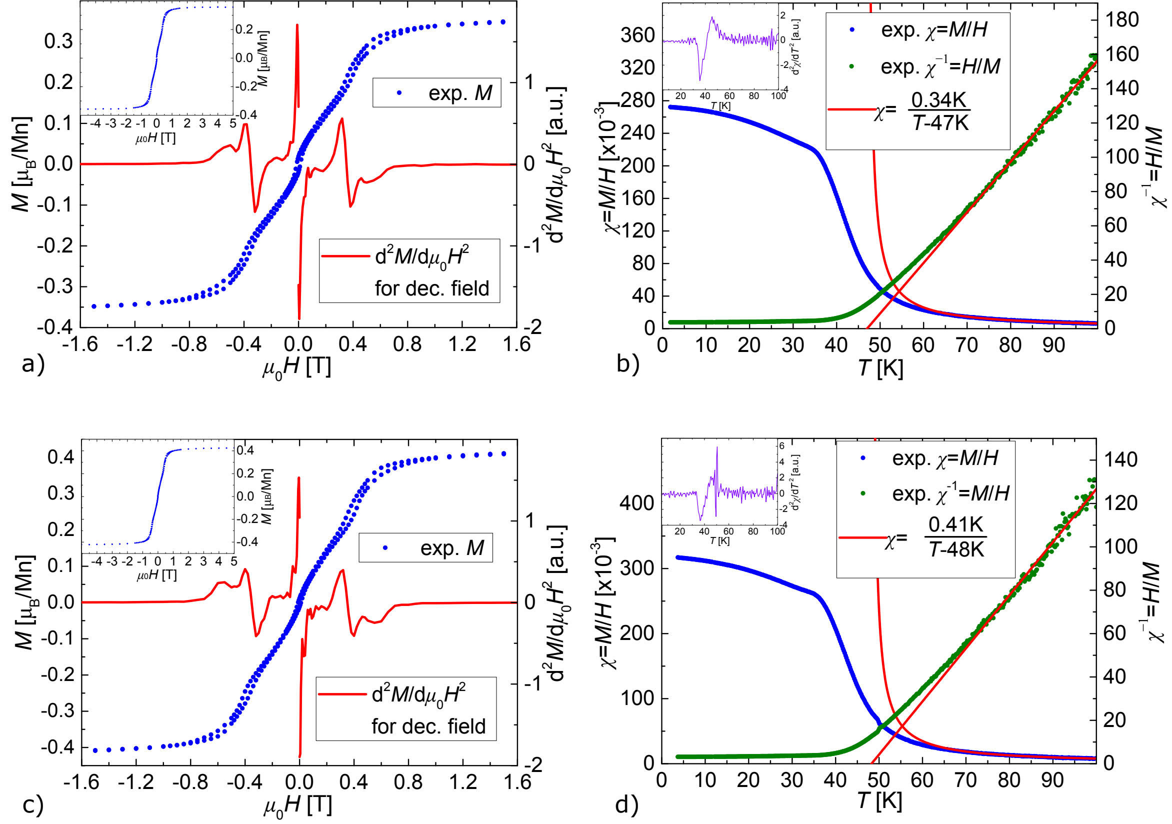

Figure 4.5: a) Magnetization of the 26 nm MnSi layer on Si(531) substrate at $T = 4.2$ K for an in plane magnetic field in blue together with the second derivative in red. The inset shows the full hysteresis curve.
b) Temperature dependent static susceptibility $\chi = M/H$ and inverse static susceptibility $\chi^-1 = H/M$ at $\mu_0 H = 0.4$ T for the same layer as shown in a). Fit of Eq. 4.2 in red to the inverse susceptibility between $T = 70$ K and $T = 100$ K. The inset shows the second derivative of the interpolated susceptibility.
c)/d) Same as a)/b) for the 26 nm MnSi layer on Si(321) substrate.

The inset shows the second derivative and the critical temperatures estimated from it are about $T_{c1} = 47$ K and $T_{c2} = 37$ K.
In conclusion, the magnetization measurements can be used to determine critical magnetic field and temperature boundaries of the layers. They also show the occurrence of twin domains and indicate twin suppression on chiral substrates. For a detailed analysis of the twin suppression, a thickness series on chiral substrates would be needed. The critical parameters determined by magnetometry measurements are reflected in magnetotransport properties, which will be shown in the following sections.

4.2 Magneto- and Hall-resistivity

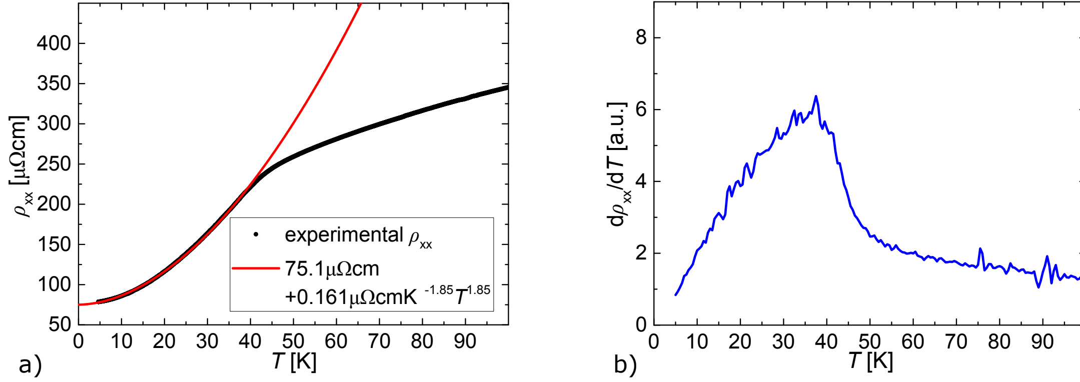

Figure 4.6: a) Temperature dependent magnetoresistivity of the 17 nm layer together with a fit for the low temperature region in red.
b) First derivative of the interpolated resistivity from a).
a) Reprinted with changed layout from M. Trabel, N. V. Tarakina, C. Pohl, J. A. Constantino, C. Gould, K. Brunner, and L. W. Molenkamp, Twin domains in epitaxial thin MnSi layers on Si(111), Journal of Applied Physics, 121(24):245310, 2017, https://aip.scitation.org/doi/abs/10.1063/1.4990284?journalCode=jap. [TTP+17]

An alternative to the SQUID measurements in the previous section to determine the critical parameters and the magnetic structure of MnSi layers are magnetotransport and Hall measurements. The corresponding measurement method and underlying physical effects are explained in chapter 2.4.2.
Fig. 4.6 a) shows the longitudinal resistivity ρ_{xx} of the 17 nm layer. From the maximum in the derivative of the interpolated resistivity, shown in Fig. 4.6 b), a critical temperature of about $T_{\mathrm{c3}} = 38$ K can be estimated. For temperatures below T_{c3}, the curve exhibits a $\rho_{\mathrm{xx,0}} + AT^c$ behavior with a residual resistivity of $\rho_{\mathrm{xx,0}} = 75.1$ µΩcm and a power law of $T^{1.85}$ which corresponds well to the T^2 behavior shown for bulk MnSi and expected from spin fluctuations [KOD82, UM75].
Fig. 4.7 a) shows the same measurement for the 32 nm layer. From the maximum in the derivative of the interpolated resistivity a critical temperature of about $T_{\mathrm{c3}} = 39$ K can be estimated. This is the same as $T_{\mathrm{c2}} = 39$ K from the previous section. For temperatures below, the curve exhibits a $\rho_{\mathrm{xx,0}} + AT^c$ behavior with a residual resistivity of $\rho_{\mathrm{xx,0}} = 20.6$ µΩcm and a power law of $T^{1.63}$ which is comparable to the T dependence

shown in Fig. 4.6 a). The difference in the exponent shows the uncertainty in this method, which probably stems from the temperature measurement.
Fig. 4.7 b) shows the same measurement for the 26 nm MnSi layer on Si(321). The critical temperature, determined by the derivative shown in the inset, is again about 40 K and comparable to $T_{c2} = 37$ K from the previous section. The temperature dependence is the expected T^2 behavior and the residual resistivity of $\rho_{xx,0} = 8.2$ μΩ is even lower than for the layers shown before. This reduced scattering could be resulting from the lower number of domain boundaries, as the twinning is strongly suppressed. For a conclusion, measurements of samples with differing twin suppression would be needed.
Fig. 4.8 a) shows a hysteresis loop of the magnetoresistivity as well as the Hall-resistivity for the 17 nm layer discussed before. The critical field can be determined by the change of slope in measurements of the magnetoresistivity so the second derivative, shown in the inset, is used to determine the critical magnetic field. Taking the maximum in the second derivative results in a critical field of about $\mu_0 H_{c2} = 1.1$ T.
For the 32 nm layer the hysteresis loops are shown in Fig. 4.8 c). Here the derivative indicates a critical field of about $\mu_0 H_{c2} = 1.2$ T, which is two times the $\mu_0 H_{c1} = 0.6$ T determined by SQUID in the previous section.

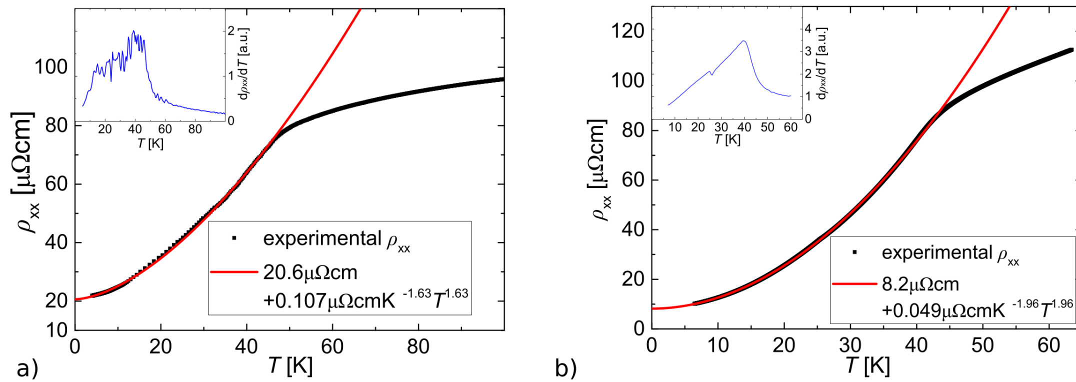

Figure 4.7: a) Temperature dependent magnetoresistivity of the 32 nm layer together with a fit for the low temperature region in red. The inset shows the first derivative of the interpolated resistivity.
b) Temperature dependent magnetoresistivity of the 26 nm layer on Si(321) substrate previously discussed together with a fit for the low temperature region in red. The inset shows the first derivative of the interpolated resistivity.

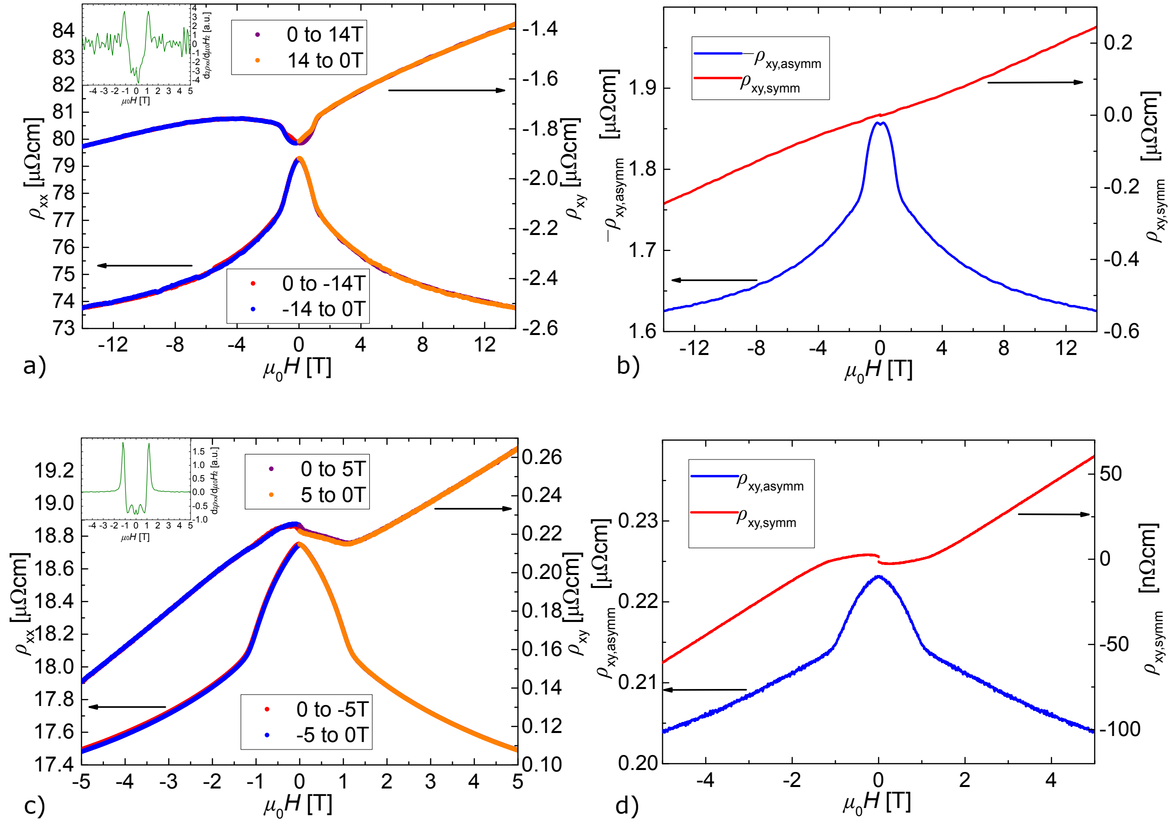

Figure 4.8: a) Magneto- and Hall-resistivity hysteresis loop at $T = 4.2$ K of the 17 nm MnSi layer. The inset shows the second derivative of the interpolated longitudinal resistivity.
b) Symmetric and antisymmetric part of the Hall-resistivity from a).
c) Magneto- and Hall-resistivity hysteresis loop at $T = 4.2$ K of the 32 nm MnSi layer. The inset shows the second derivative of the interpolated longitudinal resistivity [Har].
d) Symmetric and antisymmetric part of the Hall-resistivity from c).

This shows that both SQUID as well as magnetotransport can be used to determine critical magnetic field and temperature boundaries for their respective parameters. But as the measurement method, measured parameter and the measurement circumstances are quite different, the resulting values are differing as well.
The Hall-resistivities of the 17 nm layer in Fig. 4.8 a) is quite asymmetric in shape and has a hysteretic behavior below the critical magnetic field. The low magnetic field region would be interesting for the discussions regarding skyrmion physics mentioned in section 2.3, but the hysteresis makes symmetrization and further analysis difficult. For that reason the following concentrates on the high magnetic field region. The symmetric and asymmetric parts calculated from the interpolated Hall-resistivity for decreasing magnetic field are shown in Fig. 4.8 b). Here the shape of the asymmetric contribution is basically the same as for the magnetoresistivity. This indicates that magnetoresistivity contributes, with about 2% at $\mu_0 H = 0$ T, to the measured Hall-resistivity. This could for example be by misalignment of the Hallbar contacts.
Fig. 4.8 c) shows the Hall-resistivities for the 32 nm layer and the symmetric and asymmetric parts calculated from the interpolated Hall-resistivity for decreasing magnetic field in Fig. 4.8 d). The shape of the asymmetric contribution is again basically the same as the shape of the magnetoresistivity but only about 1% of the magnetoresistivity. The Hallbar for the measurement shown in Fig. 4.8 c) was done after the aforementioned optimization of the lithographic process, as compared to the Hallbar for the measurement shown in a). The lower misalignment influence indicates the success of the optimization.
Under the assumption that the slope at high magnetic fields well above $\mu_0 H_\mathrm{c}$ is only determined by the normal Hall effect and other contributions can be neglected, it can be used to determine the charge carrier density. Assuming only one carrier contribution the charge carrier concentration n can be calculated from the slope R_H with

$$n = \frac{1}{R_\mathrm{H} e} \ . \tag{4.5}$$

For the measurement of the 17 nm layer shown in Fig. 4.8 b) the $7-14$ T region leads to $n = 3.2 \times 10^{22}$ cm^{-3} and for the 32 nm layer shown in d) the $2-5$ T region leads to $n = 3.9 \times 10^{22}$ cm^{-3}. So the behavior is metal like with about three to four charge carriers per MnSi unit cell.

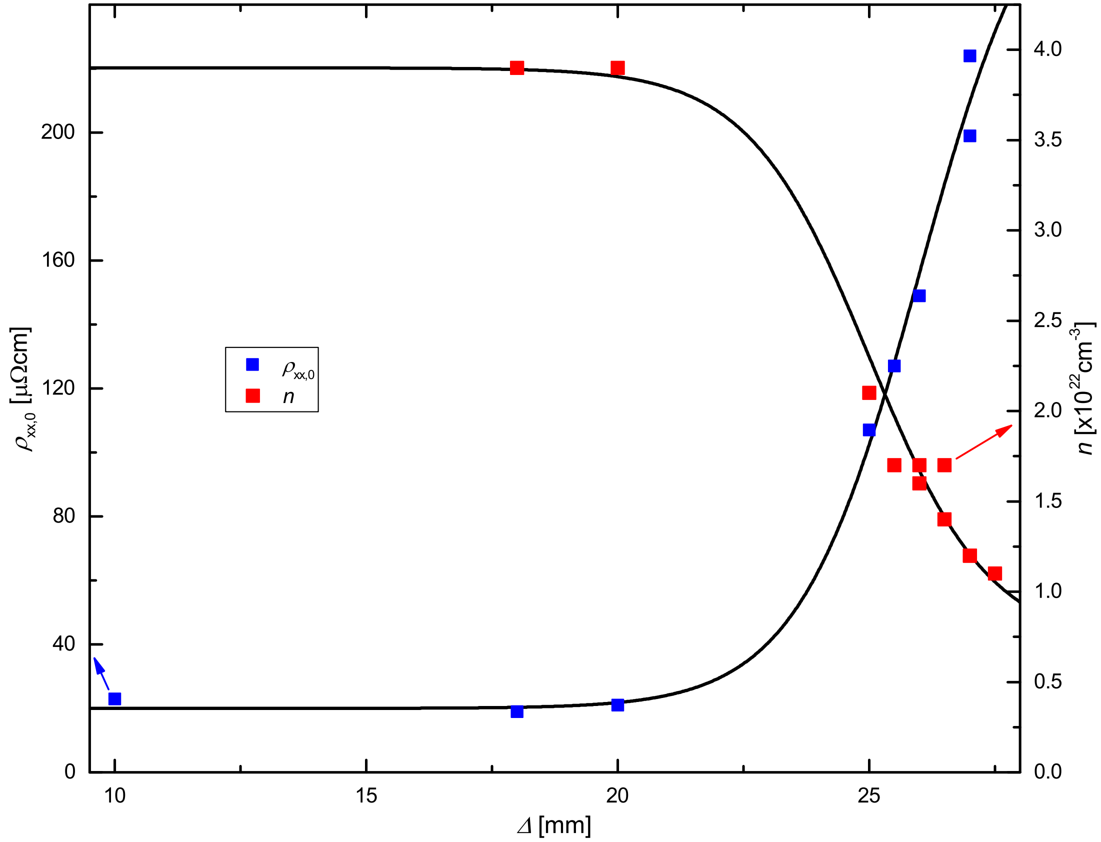

Figure 4.9: Residual resistivity $\rho_{\mathrm{xx},0}$ and charge carrier density n versus estimated distance Δ to the wafer center of the 32 nm layer. The black lines are a guide to the eye.

For the 32 nm layer magnetoresistance- and Hall-measurements are performed at samples from different positions on the 3 inch wafer, similar to the XRD measurements at different positions shown in Fig. 3.17 b) for the same layer. The resulting residual resistivity $\rho_{\mathrm{xx},0}$ as well as the charge carrier density n is shown in Fig. 4.9. The distance Δ to the wafer center is only a rough estimate from cleaving notes but it nevertheless shows a behavior as expected from the aforementioned XRD measurements. Density and resistivity are constant up to about 20 mm distance. Then the resistivity increases rapidly by about an order of magnitude, indicating a decrease in crystal quality. At the same distance the density is also decreasing by a factor of about 4.

In conclusion, magnetoresistance and Hall-resistance measurements can be used to determine the critical magnetic field and temperature boundaries and the charge car-

rier density. The latter and the residual resistivity $\rho_{\mathrm{xx},0}$ characterize also the crystal quality on a wafer. Taking only the residual resistivity $\rho_{\mathrm{xx},0}$ as an indicator, reveals an increased crystal quality for the MnSi layer on Si(321) in comparison to the one on Si(111) and could indicate the reduced domain boundaries by twin suppression.
How magneto- and Hall-resistance behave under an in plane magnetic field with changing orientation of the field direction with regard to the crystal axis will be shown in the following section. In addition the influence in the change of crystal quality demonstrated in this section on the in plane behavior will be investigated.

4.3 AMR and Planar Hall Effect (PHE)

In this section, the anisotropic response of transversal and longitudinal resistivity of epitaxial MnSi layers to electric current and magnetic field direction will be discussed. This was proposed as a tool to identify in plane skyrmions by Yokouchi *et al.* [YKT+15].
The first publication regarding AMR was 1857 by Thomson [Tho57], in which he describes a resistance difference for Nickel with a magnetic field applied either parallel or perpendicular to current flowing through the metal. The principles of this effect have since been widely used in commercial applications as sensors to detect the orientation of magnetic fields, as the resistance has a specific dependence on the exact angle between magnetic field and current direction. [JKK+15]
In the following section the exact angle dependence for MnSi will be discussed, based on the explanations given in chapter 2.4.3.

4.3.1 AMR and PHE in the field polarized phase

As discussed in previous sections, the B20 crystal structure of MnSi has a drastically reduced symmetry in comparison to other crystal structures. Its space group is $P2_13$ with P_3 projected along the [111] direction, meaning the C_3 point group in the (111) plane [Hah95]. Fig. 4.10 shows the hexagonal surface cell of left- and right-handed MnSi along the [111] direction with the handedness indicated by the circle arrow. The 120° rotation symmetry of the C_3 point group is indicated by the thick black lines showing equivalent directions. The Si(111) surface, which has the C_{3v} point group meaning an additional mirror symmetry, is shown next to it with the ±30° rotation between Si and MnSi indicated by the different direction arrows. The left- and right-handed twin are linked by the $(\bar{1}10)$ mirror plane, which would manifest itself in the same way as the earlier discussed reflection matrix V in Eq. 2.25 taking the mirror plane as the x-axis [RAM+17]. This leads to a C_{3v} point group for the twinned system instead of C_3. Taking the single crystal point group C_3, the relevant transformation matrix is

$$U = \begin{pmatrix} -\frac{1}{2} & -\frac{\sqrt{3}}{2} \\ \frac{\sqrt{3}}{2} & -\frac{1}{2} \end{pmatrix} \tag{4.6}$$

for a 120° rotation.

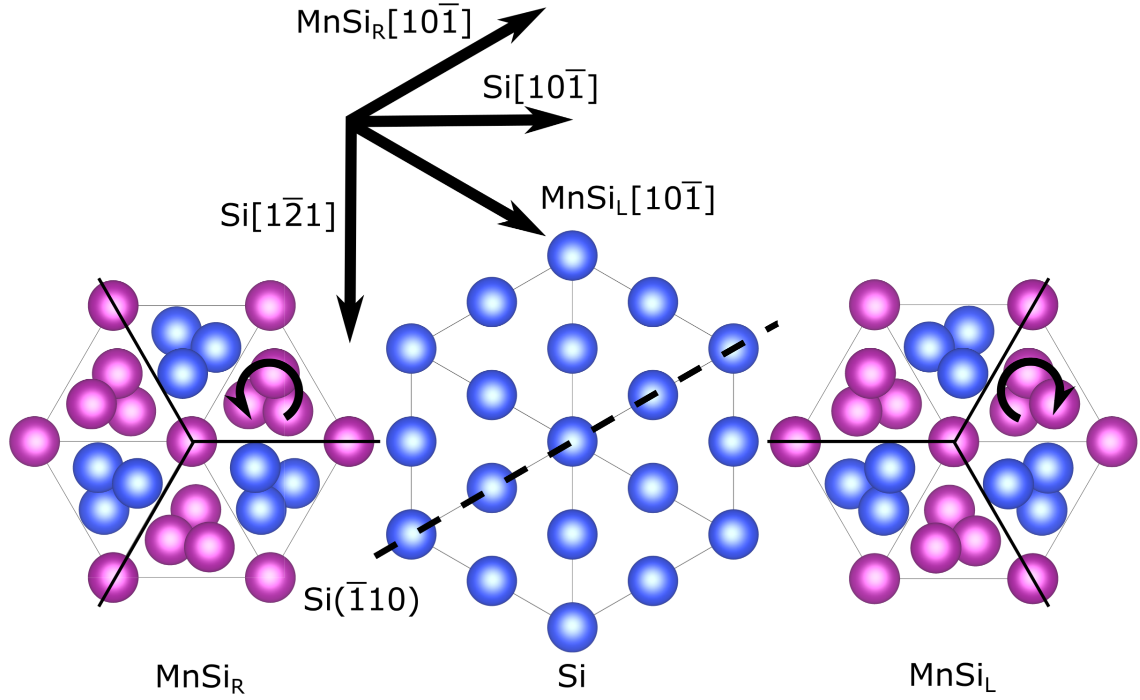

Figure 4.10: Hexagonal surface cells of Si(111) and right- and left-handed MnSi with the handedness indicated by the circle arrow and equivalent directions by the thick black lines. The ($\bar{1}$10) mirror plane connecting left- and right-handed MnSi is indicated by the dashed line and the ±30° between MnSi and Si by the labeled direction arrows. Pictures of the crystal structures have been produced with Vesta 3 [MI11].

This results in a longitudinal resistivity of

$$\begin{aligned}\rho_{\mathrm{xx}} = C_0 &+ C_2{}^* \cos(2\theta - 2\phi) + C_2{}^{*\prime} \sin(2\theta - 2\phi) \\ &+ C_4{}^* \cos(4\theta + 2\phi) + C_4{}^{*\prime} \sin(4\theta + 2\phi) \\ &+ C_6{}^* \cos(6\theta) + C_6{}^{*\prime} \sin(6\theta)\end{aligned} \tag{4.7}$$

with

$$
\begin{aligned}
C_0 =& a_{1,1} + \frac{1}{2}a_{1,1,1,1} + \frac{1}{2}a_{1,1,2,2} + \frac{3}{2}a_{1,1,1,1,1,1} + 3a_{1,1,2,2,1,1} - \frac{3}{2}a_{2,2,2,2,2,2} \\
&+ \frac{1}{2}a_{1,1,1,1,1,1,2,2} + a_{1,2,2,2,2,2,1,2} + \frac{1}{6}a_{2,2,2,2,2,2,1,1} + \frac{1}{3}a_{2,2,2,2,2,2,2,2} \\
C_2{*} =& \frac{1}{2}a_{1,1,1,1} - \frac{1}{2}a_{1,1,2,2} - a_{1,1,1,1,1,1} - 3a_{1,1,2,2,1,1} + 2a_{2,2,2,2,2,2} \\
&+ a_{1,2,2,2,2,2,2,2} - \frac{1}{3}a_{2,2,2,2,2,2,1,1} + \frac{1}{3}a_{2,2,2,2,2,2,2,2} \\
C_4{*} =& \frac{1}{2}a_{1,1,1,1,1,1} - \frac{1}{2}a_{2,2,2,2,2,2} + a_{1,2,2,2,2,2,1,2} + \frac{1}{6}a_{2,2,2,2,2,2,1,1} \\
&- \frac{1}{6}a_{2,2,2,2,2,2,2,2} \\
C_6{*} =& \frac{1}{2}a_{1,1,1,1,1,1,2,2} + a_{1,2,2,2,2,2,1,2} - \frac{1}{3}a_{2,2,2,2,2,2,1,1} - \frac{1}{6}a_{2,2,2,2,2,2,2,2}
\end{aligned}
\tag{4.8}
$$

and

$$
\begin{aligned}
C_2{*}' =& a_{2,2,1,2} - \frac{1}{2}a_{1,1,1,1,1,2} + \frac{1}{2}a_{2,2,2,2,1,2} - \frac{3}{2}a_{1,1,1,1,1,2,2,2} + \frac{3}{2}a_{1,2,2,2,2,2,1,1} \\
C_4{*}' =& \frac{1}{2}a_{1,1,1,1,1,2} + \frac{1}{2}a_{2,2,2,2,1,2} - \frac{3}{4}a_{1,1,1,1,1,2,2,2} + \frac{3}{4}a_{1,2,2,2,2,2,2,2} \\
C_6{*}' =& \frac{1}{2}a_{1,2,2,2,2,2,1,1} + \frac{1}{2}a_{1,2,2,2,2,2,2,2} \ .
\end{aligned}
\tag{4.9}
$$

A more conventional form is $\rho_{\mathrm{AMR}} = (\rho_{\mathrm{xx}} - \rho_{\mathrm{xx,av}})/\rho_{\mathrm{xx,av}}$ with $\rho_{\mathrm{xx,av}} = C_0$ [RAM+17], so

$$
\begin{aligned}
\rho_{\mathrm{AMR}} =& C_2\cos(2\theta - 2\phi) + C_2'\sin(2\theta - 2\phi) \\
&+ C_4\cos(4\theta + 2\phi) + C_4'\sin(4\theta + 2\phi) \\
&+ C_6\cos(6\theta) + C_6'\sin(6\theta) \ ,
\end{aligned}
\tag{4.10}
$$

with $C_2 = C_2{*}/C_0$, $C_4 = C_4{*}/C_0$ etc.

Considering the occurrence of a twin domain structure in this material one could assume that only the non crystalline C_2 and C_2' terms should appear. These terms depend only on the difference between current and magnetic field direction and also appear in polycrystalline material. If the twins would be randomly oriented to each other one would indeed only measure the C_2 and C_2' terms. Because of the well defined 60° angle between left- and right-handed MnSi, as shown in Fig. 4.10, this is not what to expect here. As mentioned the C_2 and C_2' terms are obviously invariant under a

rotation of the crystal structure. But the C_4, C'_4 and C_6, C'_6 terms are also invariant under a 60° rotation as all terms depend on sums of six angles and $6 \times 60° = 360°$. Taking the C_{3v} point group for the whole twinned system instead of C_3 of the single B20 crystal layer, Eq. 4.10 becomes [RAM+17]

$$\begin{aligned}\rho_{\mathrm{AMR}} =& C_2 \cos(2\theta - 2\phi) \\ &+ C_4 \cos(4\theta + 2\phi) \\ &+ C_6 \cos(6\theta) \ .\end{aligned} \tag{4.11}$$

For the PHE only taking rotational symmetries into account leads to

$$\begin{aligned}\rho_{\mathrm{PHE}} =& C_2 \sin(2\theta - 2\phi) - C'_2 \cos(2\theta - 2\phi) \\ &- C_4 \sin(4\theta + 2\phi) + C'_4 \cos(4\theta + 2\phi) \ ,\end{aligned} \tag{4.12}$$

with $\rho_{\mathrm{PHE}} = \rho_{\mathrm{xy}}/\rho_{\mathrm{xx,av}}$ and the same coefficients as in Eq. 4.8.
If one takes also the mirror symmetry into account, the dashed coefficients vanish and for the twinned layer (C_{3v}) follows [RAM+17]

$$\begin{aligned}\rho_{\mathrm{PHE}} =& C_2 \sin(2\theta - 2\phi) \\ &- C_4 \sin(4\theta + 2\phi) \ ,\end{aligned} \tag{4.13}$$

as for ρ_{AMR} before.
To measure AMR and PHE, the 32 nm MnSi layer on Si(111) is used.
The measurements discussed in this section are done at $\mu_0 H = 2$ T, well above the critical field $\mu_0 H_{\mathrm{c}}$ determined in chapter 4.1. The layer is in the field polarized phase so the magnetization is assumed to be in the same direction as the magnetic field. Fig. 4.12 a) shows such an AMR measurement at the rightmost Hallbar of Fig. 4.11 a), which is approximately aligned to the Si$[10\bar{1}]-120°$ direction. Fig. 4.12 b) shows AMR at the central Hallbar with an angle difference of 30°.

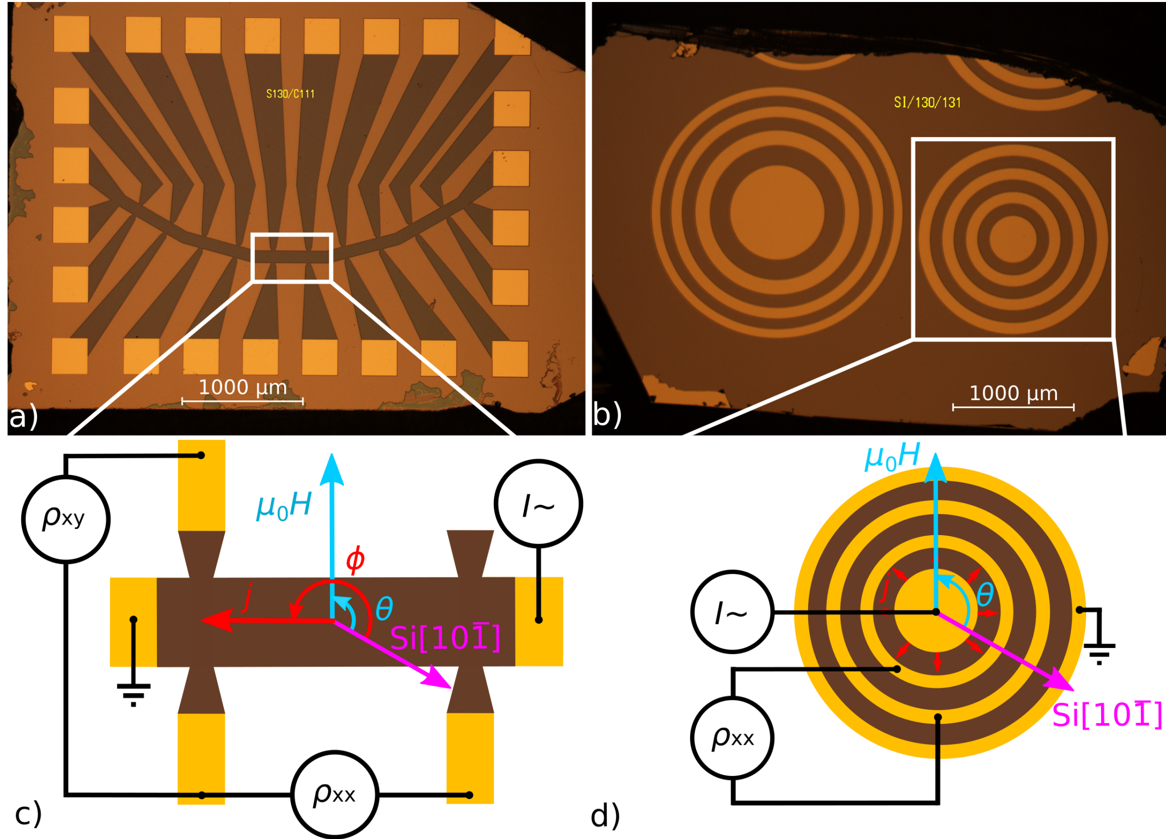

Figure 4.11: Same figure as Fig. 2.10
a) Optical picture of a Hallbar-set of the 32 nm MnSi layer on Si(111) with one current path and an angle difference of 15° between each 300 µm × 100 µm Hallbar.
b) Optical picture of two Corbino-discs of the 32 nm MnSi layer on Si(111) with gold contacts at constant radial steps of the used disc on the right.
c) Schematic of the measurement setup at the central Hallbar of a) which is aligned to the Si[10$\bar{1}$] − 150° direction. The angle θ is between magnetic field $\mu_0 H$ and reference crystal direction Si[10$\bar{1}$] and the angle ϕ between current j and reference crystal direction Si[10$\bar{1}$]
d) Sketch of the measurement at the Corbino-disc of b) with the angle θ between magnetic field $\mu_0 H$ and reference crystal direction Si[10$\bar{1}$] and radialsymmetric current flow.

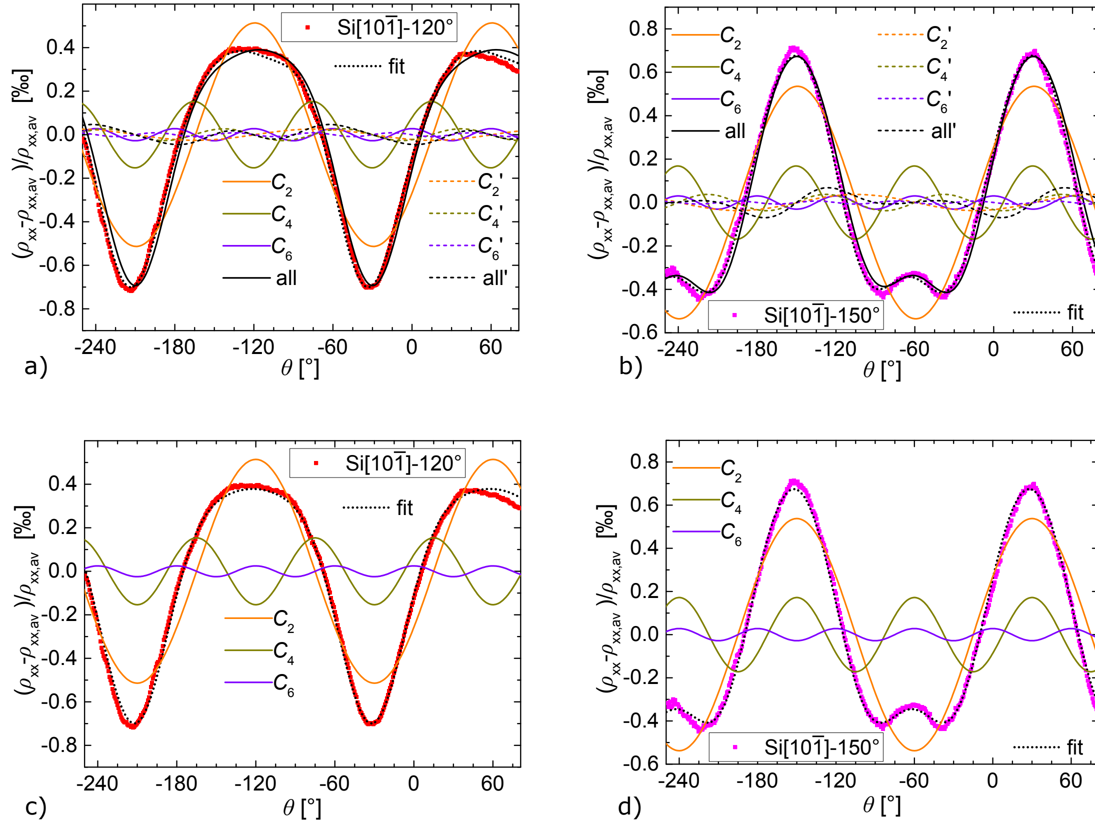

Figure 4.12: a) AMR at $T \approx 4.2$ K and $\mu_0 H = 2$ T for the rightmost Hallbar in Fig. 4.11 a) aligned along Si$[10\bar{1}] - 120°$ with a fit of Eq. 4.10 and the different contributions labeled with their coefficients.
b) AMR measurement and fit as a) for the central Hallbar in Fig. 4.11 a) aligned along Si$[10\bar{1}] - 150°$.
c)/d) Same as shown in a)/b) but with fits of Eq. 4.11 and the different contributions labeled with their coefficients.

To determine the misalignment of the current and magnetic field direction with respect to the reference crystal direction Si$[10\bar{1}]$ a fit with Eq. 4.10 is done at both measurements with all parameters free except taking the same θ and ϕ misalignment for both measurements. This leads to a current direction misalignment of 0.70° and a magnetic field direction misalignment of 4.5° with respect to the reference crystal axis. These values are then taken as fixed values for the separate fits shown in Fig. 4.12 a) and b) where only an additional constant offset is allowed. As one can see indicated by the dotted line, Eq. 4.10 is able to describe both measurements quite well.
The coefficients for each fit can be found in Tab. 4.1. C_2' and C_4' and C_6' are way

Sample	C_2 [‰]	C_2' [‰]	C_4 [‰]	C_4' [‰]	C_6 [‰]	C_6' [‰]
Si[10$\bar{1}$] – 120°	0.51	0.026	-0.15	-0.027	0.028	-0.0087
Si[10$\bar{1}$] – 150°	0.54	0.037	-0.17	-0.037	0.031	-0.0068

Table 4.1: Parameter for the fit of Eq. 4.10 shown in Fig. 4.12.

smaller than their unprimed counterparts, which strongly suggests that the number of terms necessary to describe the measured AMR can be further reduced. The natural assumption is that this can by done by applying the C_{3v} symmetry of the twinned system, as it eliminates exactly the primed parameters with negligible values. To demonstrate this, Fig 4.12 c) and d) show the same measurements as in a) and b) but with a fit of Eq. 4.11. Here a simultaneous fit leads to a current direction misalignment of $-0.021°$ and a magnetic field direction misalignment of $2.1°$. One can clearly see that Eq. 4.11 is not worse than Eq. 4.10 to describe the measurement. The corresponding coefficients, shown in Tab. 4.2, are also staying almost the same. This strongly suggests that it is the C_{3v} symmetry of the twinned system that is influencing the whole AMR.

Sample	C_2 [‰]	C_4 [‰]	C_6 [‰]
Si[10$\bar{1}$] – 120°	0.51	-0.15	0.025
Si[10$\bar{1}$] – 150°	0.54	-0.17	0.028

Table 4.2: Parameter for the fit of Eq. 4.11 shown in Fig. 4.12.

Fig. 4.13 a) shows the measurements of AMR as well as PHE at the full Hallbar set shown in Fig. 4.11 a). The AMR measurements are the upper set of colored curves and the PHE measurements the lower set, separated by the labels indicating the respective Hallbar orientations. The curves are offset for readability and the center of each is represented by a tick. The scale of 1‰ is given in the figure. Simultaneous fits of Eq. 4.11 and 4.13 for each Hallbar are shown in black. The used current direction misalignment of 0.72° and magnetic field direction misalignment of 4.5° is estimated from a fit on all Hallbars simultaneously. The fits reproduce the curves quite well with the corresponding parameters for each Hallbar listed in Tab. 4.3. An exemplary estimation of the error for the red curves by variation of the fit parameters gives $\Delta C_2 = 0.08‰$, $\Delta C_4 = 0.06‰$ and $\Delta C_6 = 0.04‰$, which means the parameters for the full set are constant within this error. Nevertheless a trend seems to be visible

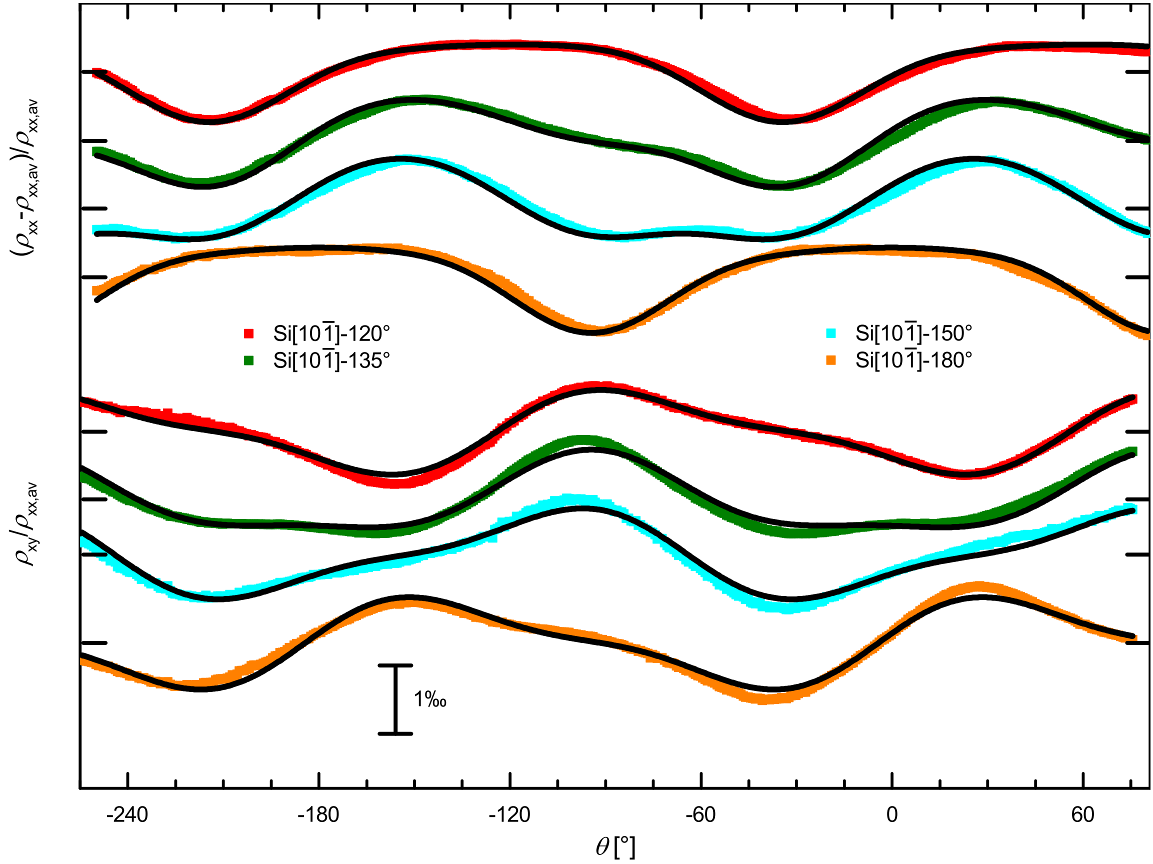

Figure 4.13: AMR and PHE for the full Hallbar set shown in Fig. 4.11 a) with the labels separating the upper AMR curves from the lower PHE curves. The curves are offset with the ticks marking the respective center. The black lines are simultaneous fits of Eq. 4.11 and 4.13 to AMR and PHE for each Hallbar individually.

with a small increase from right to left of the Hallbar set. This will be explored in more detail later.

For C_6 the estimated error is even bigger than the actual value, highlighting the need for a separate verification. As the only term of Eq. 4.13 being independent from the current direction (ϕ), C_6 can be measured at the Corbino disc. The corresponding measurement is shown in Fig. 4.14 a) and reveals a clear 6θ dependence. The additional modulation comes probably from a small misalignment between rotation plane and Corbino plane. The value $C_6 = 0.040‰$, determined with a fit of Eq. 4.11, where C_2 and C_4 are set to zero, is comparable to the C_6 parameters determined for the set of Hallbars.

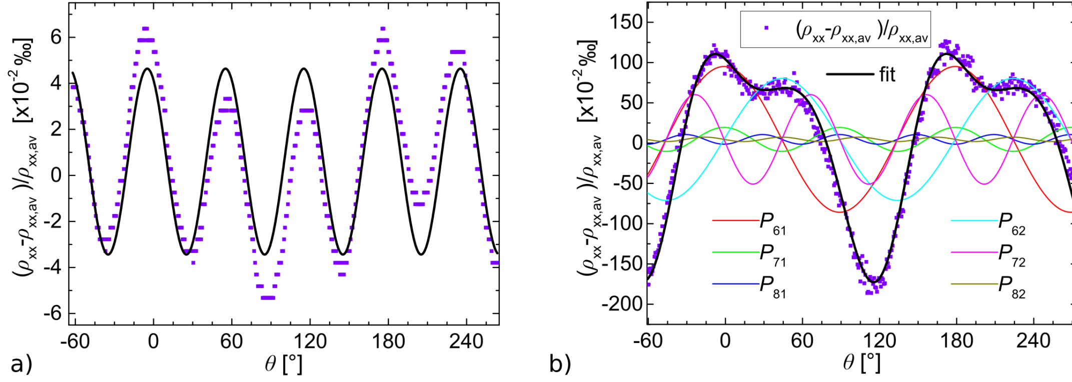

Figure 4.14: a) AMR at the Corbino disc shown in Fig. 4.11 b) of the 32 nm MnSi layer on Si(111) with a fit of the ϕ independent term of Eq. 4.11 in black. b) AMR at the corresponding Corbino disc of the 26 nm MnSi layer on Si(321) substrate with a fit of the ϕ-independent terms of Eq. 2.21 and the different contributions labeled with their coefficients.

Sample	C_2 [‰]	C_4 [‰]	C_6 [‰]
Si[10$\bar{1}$] – 120°	0.54	-0.17	0.025
Si[10$\bar{1}$] – 135°	0.55	-0.18	0.031
Si[10$\bar{1}$] – 150°	0.58	-0.18	0.032
Si[10$\bar{1}$] – 180°	0.59	-0.19	0.036

Table 4.3: Parameter for the fit of Eq. 4.11 and 4.13 shown in Fig. 4.13 a).

In summary the results show that the AMR is influenced by the symmetry of the twinned system instead of only the symmetry of a single crystal. This means that the suppressed twinning occurring on chiral substrates demonstrated in section 3.5.2 should change the resulting AMR and PHE measurements. A severe drawback however is that the layer normal and rotation axis of the chiral substrates is not the high symmetry direction Si[111], which means no symmetries can be applied to reduce the complexity. Instead the full Eq. 2.21 and 2.23 need to be fitted to the measured curves.

Fig. 4.15 shows the AMR and PHE measurements of a full set of Hallbars in the same way as before, but for the 26 nm MnSi layer on Si(321) substrate discussed before. As the exact determination of the crystal direction becomes quite complicated, the direction of the center Hallbar is now taken as the reference direction. The simul-

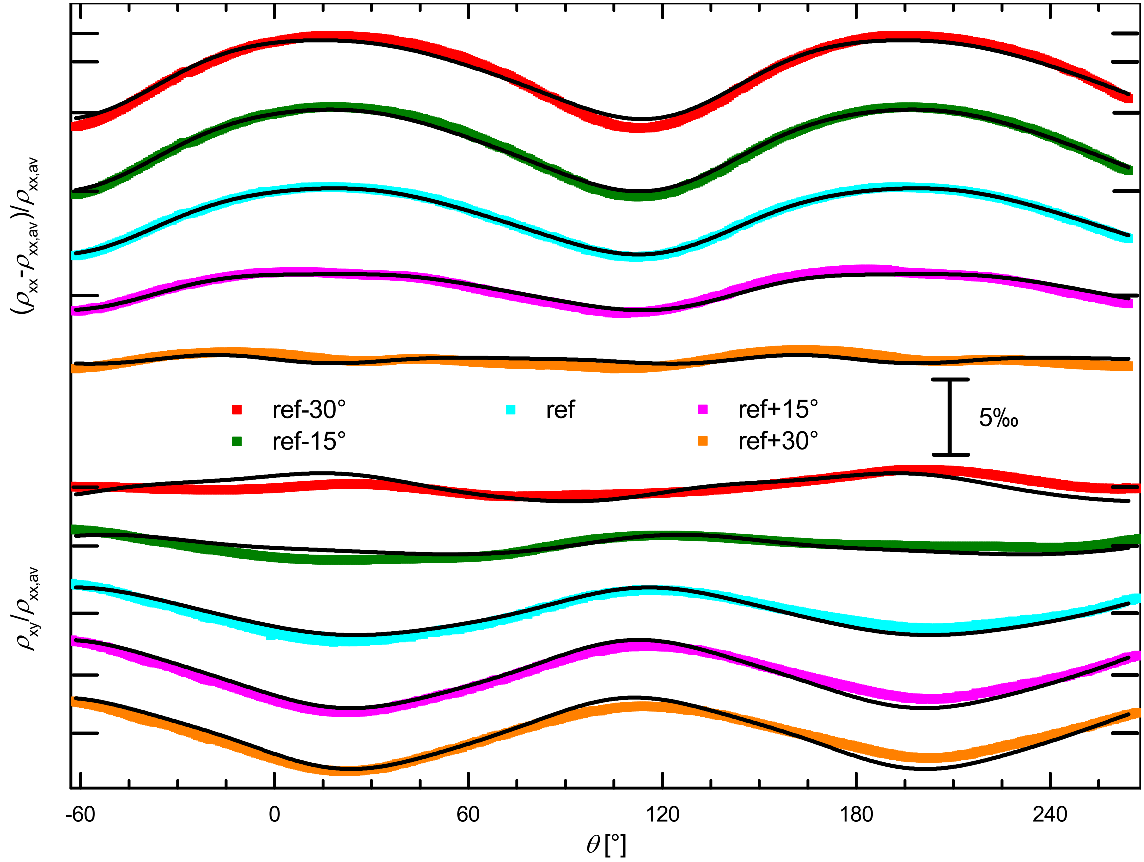

Figure 4.15: AMR and PHE for a full Hallbar set as shown in Fig. 4.11 but on the 26 nm MnSi layer on Si(321) substrate. The labels are separating the upper AMR curves from the lower PHE curves. The curves are offset with the ticks marking the respective center. The black lines are simultaneous fits of Eq. 2.21 and 2.23 to AMR and PHE for all Hallbars.

taneous fits of 2.21 and 2.23 do not reproduce all curves as well as before, but are able to describe the principal behavior reasonably well. The reason is probably that in comparison to before a fit for each Hallbar can not be done, because Eq. 2.21 and 2.23 have too many free parameters. This means slight changes of the parameters for each Hallbar, as observed for the previously shown set, worsen the overall fit.
The parameters for the fit are listed in Tab. 4.4 with $P_{ow} = P_{ow}{}^{*}/P_{00}$. One can see that no terms of Eq. 2.21 and 2.23 can obviously be neglected, as expected for the non existent symmetries of the Si(321) layer plane. The mirror symmetry of a twinned system can also not be observed rotating around this surface, as the mirror plane would have to be perpendicular to the surface to have the same influence as before. That no

Parameter	Dependence	Value [‰]	Parameter	Dependence	Value [‰]
P_{01}	$\cos(2\theta + 2\phi)$	1.2	P_{11}	$\cos(2\theta - 2\phi)$	0.26
P_{21}	$\cos(4\theta + 2\phi)$	-0.093	P_{31}	$\cos(4\theta - 2\phi)$	0.022
P_{41}	$\cos(6\theta + 2\phi)$	0.0018	P_{51}	$\cos(6\theta - 2\phi)$	-0.038
P_{61}	$\cos(2\theta)$	0.37	P_{71}	$\cos(4\theta)$	0.13
P_{81}	$\cos(6\theta)$	-0.041	P_{91}	$\cos(2\phi)$	-7.3
P_{02}	$\sin(2\theta + 2\phi)$	-0.021	P_{12}	$\sin(2\theta - 2\phi)$	1.2
P_{22}	$\sin(4\theta + 2\phi)$	-0.00070	P_{32}	$\sin(4\theta - 2\phi)$	0.066
P_{42}	$\sin(6\theta + 2\phi)$	0.069	P_{52}	$\sin(6\theta - 2\phi)$	0.033
P_{62}	$\sin(2\theta)$	0.28	P_{72}	$\sin(4\theta)$	-0.35
P_{82}	$\sin(6\theta)$	-0.11	P_{92}	$\sin(2\phi)$	-1.1

Table 4.4: Parameter for the fits of Eq. 2.21 and 2.23 shown in Fig. 4.15 a).

terms can be neglected is also well illustrated in Fig. 4.14 b) which shows the AMR measurement on a Corbino disc on the same layer. The fit of terms independent of ϕ in Eq. 2.21 in black, with the colored curves for the different contributions listed in Tab. 4.5, represent the curve quite well and no parameter can be neglected.

Parameter	Dependence	Value [‰]	Parameter	Dependence	Value [‰]
P_{61}	$\cos(2\theta)$	0.90	P_{71}	$\cos(4\theta)$	0.15
P_{81}	$\cos(6\theta)$	-0.060	-	-	
P_{62}	$\sin(2\theta)$	0.76	P_{72}	$\sin(4\theta)$	-0.56
P_{82}	$\sin(6\theta)$	-0.027	-	-	

Table 4.5: Parameter for the fit of Eq. 2.21 shown in Fig. 4.15 b).

In conclusion this shows that the AMR and PHE measurements on the Si(321) surface represent the nonexistent symmetries leading to twin suppression quite well. Unfortunately this also means that it can not be used to demonstrate the twin suppression, as the mirror symmetry is also not reflected on this surface. To be able to demonstrate the twin suppression after growth on Si(321) substrate, the sample would have to be cut to a Si(111) surface, which does not seem feasible.
Comparing the P and C parameters directly is not possible, as they consist of different sums of the a parameters. Nevertheless some of the P parameters are an order of magnitude above the C parameters. Because of that and the small trend of the C pa-

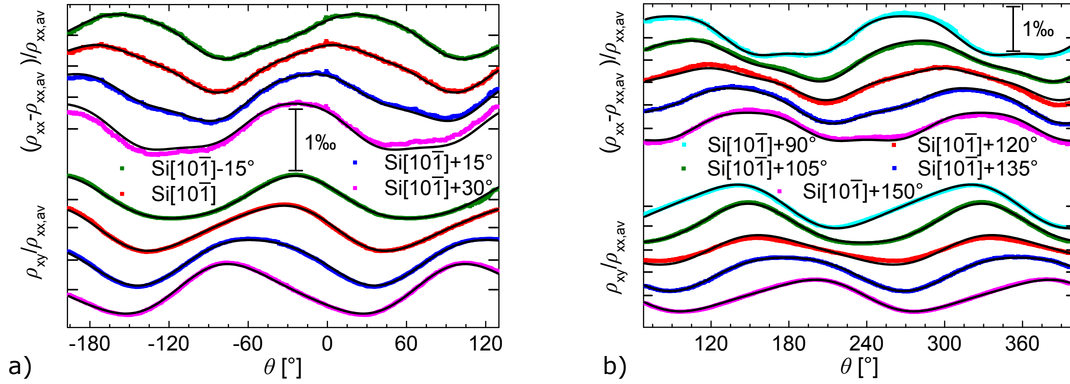

Figure 4.16: a)/b) AMR and PHE for two Hallbar sets as shown in Fig. 4.11 but on different positions on the Si(111) substrate. The labels are separating the upper AMR curves from the lower PHE curves. The curves are offset with the ticks marking the respective center. The black lines are simultaneous fits of Eq. 2.21 and 2.23 to AMR and PHE for each Hallbar.

rameters previously mentioned, possible influences on the parameters are investigated. For that AMR and PHE measurements of some of the samples on different positions of the 32 nm MnSi layer on Si(111), shown in Fig. 4.9, are shown in Fig. 4.16. The fits are done in the same way as before and represent the curves quite well. The resulting parameters with the results for the fits in Fig. 4.13 depending on $\rho_{\mathrm{xx,av}}$ are shown in Fig. 4.17 together with the exemplary error estimated before and the C_6 value of the Corbino disc indicated by the dashed violet line.

This shows a clear decrease for the absolute C_2 and C_4 value, while no conclusion can be drawn for the C_6 value which is constant within the experimental accuracy. While simple models for the parameter values exist for polycrystalline samples, for single crystals they would presumably depend on their bandstructure [CF87]. Nevertheless, a decrease with increasing impurity content (increasing $\rho_{\mathrm{xx,av}}$) was shown experimentally and reflects the measured behavior [WC67].

The higher values for some parameters in Tab. 4.4 and 4.5 on Si(321) could then indicate the suppressed scattering at domain boundaries.

In conclusion the developed model of AMR and PHE for a twinned MnSi on Si(111) system, as shown in Eq. 4.11 and 4.13, describes the measurements quite well with the parameter values decreasing with increasing disturbances, as expected from literature. The reduced symmetry on Si(321), leading to twin suppression, also prevents that AMR and PHE measurements can be used to verify the suppression. Nevertheless the

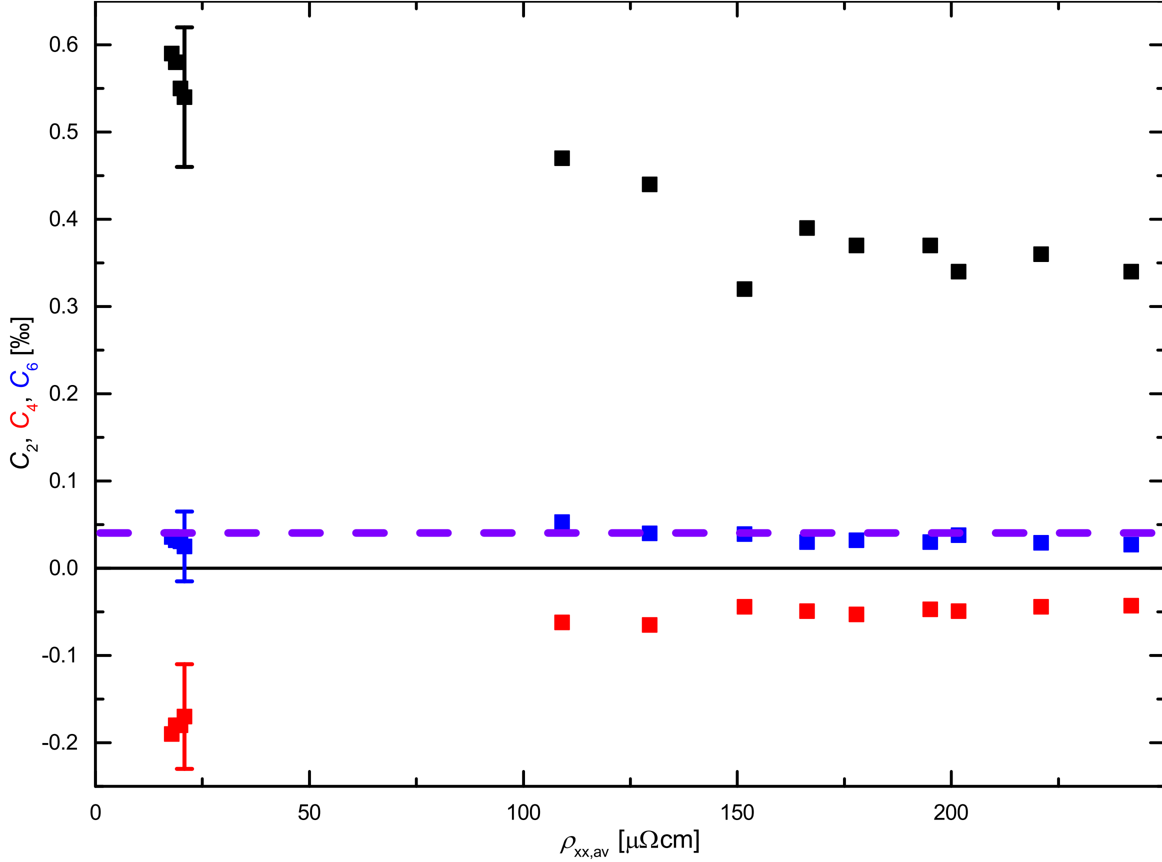

Figure 4.17: Parameters C_2 (black), C_4 (red) and C_6 (blue) versus averaged resistivity for the fits in Fig. 4.13 and 4.16, with one exemplary set of errorbars estimated from variation of the fit. C_6 of the Corbino disc is indicated by the dashed violet line.

full model, not reduced by symmetries, describes the measurements quite well. As mentioned in section 2.3, PHE measurements were also proposed as a tool to identify in plane skyrmions. For that magnetic fields below the critical field need to be applied, which will be discussed in the following section.

4.3.2 AMR and PHE below critical field and temperature

In the previous section AMR and PHE have been investigated within the field-polarized phase of MnSi. The suggested magnetic field range in which in plane skyrmions are supposed to exist is obviously below that, which leads to some problems with regard to hysteretic behavior. This can already be expected from the hysteresis shown in SQUID measurements like Fig. 4.4 a).

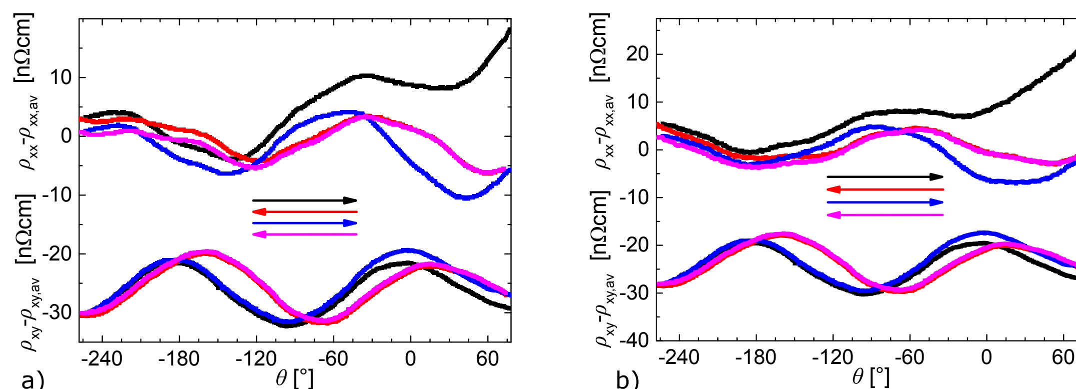

Figure 4.18: a) Repeated AMR and PHE measurements for different rotation directions at $T \approx 4.2$ K and $\mu_0 H = 0.4$ T for the rightmost Hallbar in Fig. 4.11 a). The arrows indicate the rotation direction. The curves are offset by their full average and ρ_{xy} additionally for readability.
b) Same as a) for the central Hallbar in Fig. 4.11 a) approximately aligned along Si$[10\bar{1}] - 150°$.

For AMR and PHE measurements this means the internal magnetization does not follow the external magnetic field any longer, which makes analysis as in the previous section impossible. Fig. 4.18 shows this hysteretic behavior for the two Hallbars previously discussed extensively. Because the curves are not 180° symmetric, ρ_{xx} and ρ_{xy} adjusted by their respective average over the full measurement instead of a 180° range is used, which is sufficient for principle analysis. As one could expect for a hysteresis behavior caused by magnetism, after the initial rotation in black a recurring hysteresis loop appears. Because of this behavior the measurements for different magnetic field values shown in Fig. 4.19 are done after an initial rotation and with the same rotation direction, which should make them comparable. For both sets of Hallbars a sign change in ρ_{xx} and ρ_{xy} happens around the critical field of $\mu_0 H_{\mathrm{c}} = 0.6$ T. This sign change is better illustrated in Fig. 4.20, which basically represents the sign of the peaks. Here the maximum difference to the respective average within a specific θ region, indicated by the dashed lines in Fig. 4.19, is plotted against the external magnetic field. The values for the Hallbar along Si$[10\bar{1}] - 120°$ are chosen, so that the magnetic field direction is about 90° to the current direction for ρ_{xx} and about $-45°$ for ρ_{xy}. For the Hallbar along Si$[10\bar{1}] - 150°$ it is about 0° for ρ_{xx} and about 45° for ρ_{xy}, which results in the different signs. All of the data points show similar behavior, with

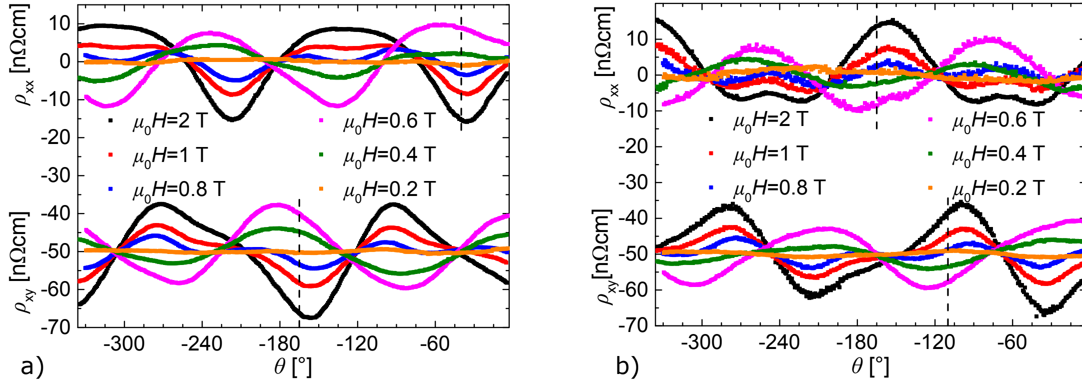

Figure 4.19: a) AMR and PHE measurements after the initial rotation at different magnetic fields $\mu_0 H$ and $T \approx 4.2$ K for the rightmost Hallbar in Fig. 4.11 a). The curves are offset by their full average and ρ_{xy} additionally for readability.
b) Same as a) for the central Hallbar in Fig. 4.11 a) approximately aligned along Si$[10\bar{1}] - 150°$.

a sign change at the critical field and then a second sign change at about $\mu_0 H_{\mathrm{c}} = 0.2$ T. This behavior, illustrated by the black curve as a guide for the eye, looks quite similar to the one observed by Yokouchi *et al.* [YKT+15]. They interpreted two sign changes as entering and exiting a skyrmion phase. However, going back to the full angle dependence in Fig. 4.19, the assumption of a real second sign change at $\mu_0 H_{\mathrm{c}} = 0.2$ T seems hard to justify. Instead, after the sign change at the critical field it seems to slowly decrease down to a constant angle independent value, which seems plausible considering that the spins follow the external field for decreasing strength less and less and instead assume their intrinsic orientation.
In conclusion, the AMR and PHE measurements of MnSi layers show one clear transition at the critical field, but hysteresis coupled with the small values prevent conclusive analysis for lower magnetic field regarding the occurrence of a skyrmion lattice. The measurements, however, indicate no additional phase transitions.

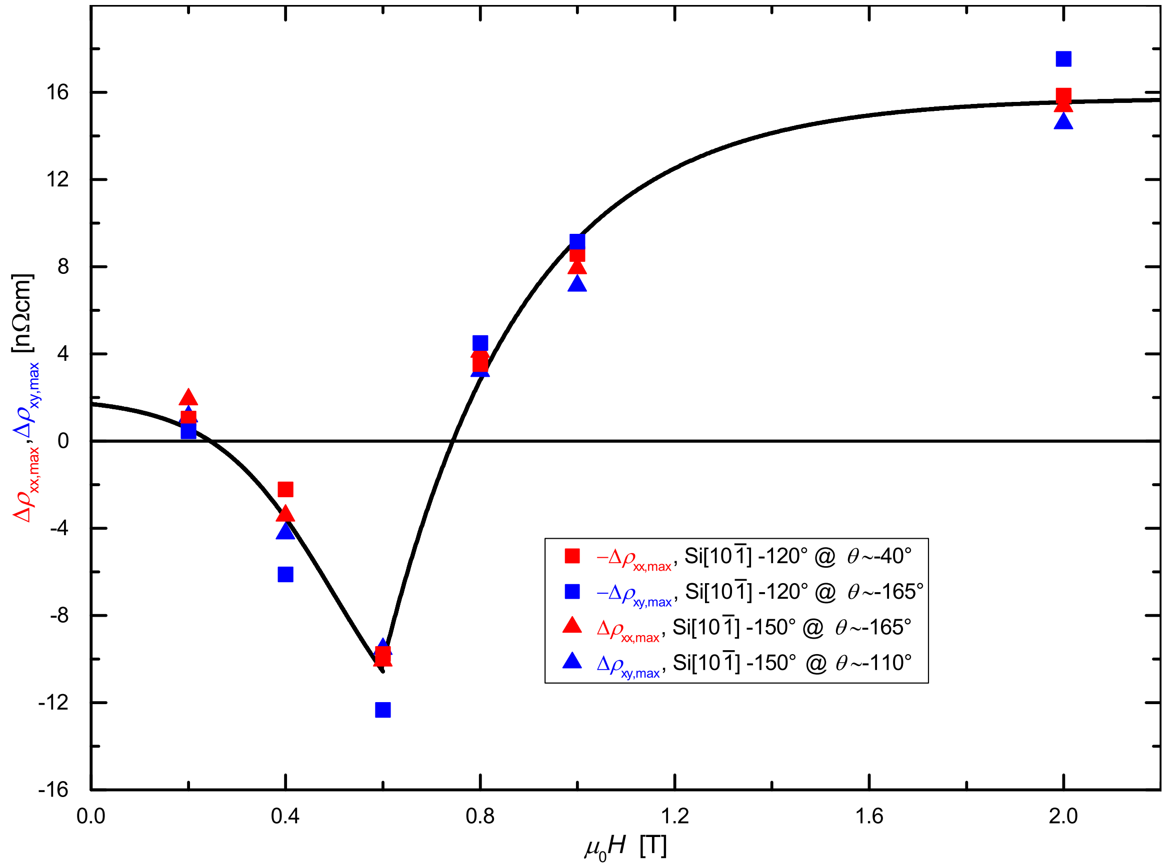

Figure 4.20: Maximum difference in specific θ regions of ρ_{xx} and ρ_{xy} to their respective average value for the curves in Fig. 4.19. The black curves are only a guide for the eye.

5 Summary

This thesis describes the growth and characterization of epitaxial MnSi thin films on Si substrates. The interest in this material system stems from the rich magnetic phase diagram resulting from the noncentrosymmetric B20 crystal structure. Here neighboring spins prefer a tilted relative arrangement in contrast to ferro- and antiferromagnets, which leads to a helical ground state where crystal and spin helix chirality are linked [IEM+85]. This link makes the characterization and control of the crystal chirality the main goal of this thesis.

After a brief description of the material properties and applied methods, the thesis itself is divided into four main parts. In the first part the advancement of the MBE growth process of MnSi on Si(111) substrate as well as the fundamental structural characterization are described. Here the improvement of the substrate interface by an adjusted substrate preparation process is demonstrated, which is the basis for well ordered flat MnSi layers. On this foundation the influence of Mn/Si flux ratio and substrate temperature on the MnSi layer growth is investigated via XRD and clear boundaries to identify the optimal growth conditions are determined. The nonstoichiometric phases outside of this optimal growth window are identified as HMS and Mn_5Si_3. Additionally, a regime at high substrate temperatures and low Mn flux is discovered, where MnSi islands are growing incorporated in a Si layer, which could be interesting for further investigations as a size confinement can change the magnetic phase diagram [DBS+18]. XRD measurements demonstrate the homogeneity of the grown MnSi layers over most of the 3 inch wafer diameter and a small ω-FWHM of about 0.02° demonstrates the high quality of the layers. XRD and TEM measurements also show that relaxation of the layers happens via misfit dislocations at the interface to the substrate.

The second part of the thesis is concerned with the crystal chirality. Here azimuthal ϕ-scans of asymmetric XRD reflections reveal twin domains with a $\pm 30°$ rotation to the substrate. These twin domains seem to consist of left and right-handed MnSi, which

are connected by a mirror operation at the $(\bar{1}10)$ plane. For some of the asymmetric XRD reflections this results in different intensities for the different twin domains, which reveals that one of the domains is rotated $+30°$ and the other is rotated $-30°$. From XRD and TEM measurements an equal volume fraction of both domains is deduced. Different mechanisms to suppress these twin domains are investigated and successfully achieved with the growth on chiral Si surfaces, namely Si(321) and Si(531). Azimuthal ϕ-scans of asymmetric XRD reflections demonstrate a suppression of up to 92%. The successful twin suppression is an important step in the use of MnSi for the proposed spintronics applications with skyrmions as information carriers, as discussed in the introduction.

Because of this achievement, the third part of the thesis on the magnetic properties of the MnSi thin films is not only concerned with the principal behavior, but also with the difference between twinned and twin suppressed layers. Magnetometry measurements are used to demonstrate, that the MnSi layers behave principally as expected from the literature. The analysis of saturation and residual magnetization hints to the twin suppression on Si(321) and Si(531) substrates and further investigations with more samples can complete this picture. For comparable layers on Si(111), Si(321) and Si(531) the Curie-Weiss temperature is identical within 1 K and the critical field within 0.1 T. Temperature dependent magnetoresistivity measurements also demonstrate the expected T^2 behavior not only on Si(111) but also on Si(321) substrates. This demonstrates the successful growth of MnSi on Si(321) and Si(531) substrates. The latter measurements also reveal a residual resistivity of less then half for MnSi on Si(321) in comparison to Si(111). This can be explained with the reduced number of domain boundaries demonstrating the successful suppression of one of the twin domains. The homogeneity of the residual resistivity as well as the charge carrier density over a wide area of the Si(111) wafer is also demonstrated with these measurements as well as Hall effect measurements.

The fourth part shows the AMR and PHE of MnSi depending on the angle between in plane current and magnetic field direction with respect to the crystal direction. This was proposed as a tool to identify skyrmions [YKT+15]. The influence of the higher C_{3v} symmetry of the twinned system instead of the C_3 symmetry of a B20 single crystal is demonstrated. The difference could serve as a useful additional tool to prove the twin suppression on the chiral substrates. But this is only possible for rotations with specific symmetry surfaces and not for the studied unsymmetrical Si(321) surface.

Measurements for MnSi layers on Si(111) above the critical magnetic field demonstrate the attenuation of AMR and PHE parameters for increasing resistivity, as expected from literature [WC67]. Even if a direct comparison to the parameters on Si(321) is not possible, the higher values of the parameters on Si(321) can be explained considering the reduced charge carrier scattering from domain boundaries. Below the critical magnetic field, which would be the region where a skyrmion lattice could be expected, magnetic hysteresis complicates the analysis. Only one phase transition at the critical magnetic field can be clearly observed, which leaves the existence of a skyrmion lattice in thin epitaxial MnSi layers open.
The best method to solve this question seems to be a more direct approach in the form of Lorentz-TEM, which was also successfully used to visualize the skyrmion lattice for thin plates of bulk MnSi [TYY+12]. For the detection of in plane skyrmions, lamellas would have to be prepared for a side view, which seems in principle possible.
The demonstrated successful twin suppression for MnSi on Si(321) and Si(531) substrates may also be applied to other material systems. Suppressing the twinning in FeGe on Si(111) would lead to a single chirality skyrmion lattice near room temperature [HC12]. This could bring the application of skyrmions as information carriers in spintronics within reach.

6 Zusammenfassung

Diese Arbeit befasst sich mit dem Wachstum und der Charakterisierung dünner epitaktischer MnSi Schichten auf Si Substraten. Das Interesse an diesem Materialsystem liegt insbesondere im reichhaltigen magnetischen Phasendiagramm begründet, welches aus der nicht zentrosymmetrischen B20 Kristallstruktur des MnSi resultiert. Im Gegensatz zu Ferro- oder Antiferromagneten bevorzugen benachbarte Spins sich unter einem Winkel zueinander auszurichten, was zu einem helikalen Grundzustand führt in dem die Händigkeit von Kristallstruktur und Spin-Helix aneinander gekoppelt sind [IEM+85]. Diese Kopplung macht die Charakterisierung und Kontrolle der Händigkeit der Kristallstruktur zum Hauptziel dieser Arbeit.
Nach einer kurzen Beschreibung der Materialeigenschaften und der angewendeten Methoden ist die Arbeit selbst in vier Hauptteile aufgeteilt. Im ersten Teil ist sowohl die Verbesserung des Molekularstrahlepitaxie-Wachstumsprozesses von MnSi auf Si(111) Substrat, als auch die grundlegende strukturelle Charakterisierung beschrieben. Hierbei ist die Verbesserung der Substratgrenzfläche mit Hilfe eines angepassten Vorbereitungsprozesses erläutert, welche die Basis für glatte, geordnete dünne MnSi Schichten bildet. Auf dieser Basis ist der Einfluss des Mn/Si Fluss-Verhältnisses sowie der Substrattemperatur mittels Röntgenbeugung dargestellt und ein optimales Wachstumsfenster identifiziert. Die nicht stöchiometrischen Phasen außerhalb dieses Wachstumsfensters sind $MnSi_{1.75-x}$ (HMS) sowie Mn_5Si_3. Zusätzlich tritt bei hohen Substrattemperaturen und niedrigem Mn Fluss eine Phase auf, in der MnSi Inseln, eingebettet in eine Si Schicht, wachsen. Diese könnten von weiterführendem Interesse sein, da die Größenbeschränkung das magnetische Phasendiagramm beeinflussen kann [DBS+18]. Röntgenbeugungsmessungen zeigen die Homogenität der gewachsenen MnSi Schichten über einen Großteil des 3 Zoll Wafer Durchmessers sowie die hohe Qualität mittels einer kleinen ω-Halbwertsbreite von ungefähr 0.02°. Röntgenbeugungs- und Transmissionselektronenmikroskopiemessungen zeigen außerdem, dass die MnSi Dünnschichten mittels Fehlversetzungen an der Grenzfläche zwischen Dünnschicht und Substrat re-

laxieren.

Der zweite Teil befasst sich mit der Händigkeit der Kristallstruktur. Azimutale ϕ-Messungen asymmetrischer Röntgenbeugungsreflexe zeigen Kristallzwillingsdomänen welche $\pm 30°$ zum Substrat rotiert sind. Die Kristallzwillingsdomänen lassen sich vermutlich als rechts- und links-händiges MnSi identifizieren, welche durch eine Spiegelung an der $(\bar{1}10)$ Ebene verbunden sind. Anhand der unterschiedlichen Intensität mancher Reflexe für unterschiedliche Händigkeit wird außerdem gezeigt, dass eine der Domänen um $+30°$ und die andere Domäne um $-30°$ rotiert ist. Mithilfe der Röntgenbeugung und Transmissionselektronenmikroskopie wird außerdem der gleiche Volumenanteil der Kristallzwillinge demonstriert. Verschieden Mechanismen zur Unterdrückung dieser Kristallzwillingsdomänen werden untersucht und die erfolgreiche Unterdrückung gelang mit Hilfe des Wachstums auf chiralen Si Substraten, nämlich Si(321) und Si(531) Substraten. Hier ist mit azimutalen ϕ-Messungen der asymmetrischen Röntgenbeugungsreflexen eine Unterdrückung von bis zu 92% demonstriert. Die erfolgreiche Unterdrückung der Kristallzwillingsdomänen ist ein wichtiger Schritt zur vorgeschlagenen Nutzung von MnSi in Spintronik-Anwendungen, wie in der Einleitung erläutert.

Aufgrund dessen befasst sich der dritte Teil nicht nur mit den magnetischen Eigenschaften der dünnen MnSi Schichten, sondern auch damit, wie die Unterschiede für Schichten mit Kristallzwillingsdomänen und mit deren Unterdrückung sind. Im ersten Abschnitt ist anhand von Magnetometriemessungen gezeigt, dass sich die MnSi Dünnschichten prinzipiell so verhalten, wie es aus der Literatur zu erwarten ist. Das Verhalten von Sättigungs- und Restmagnetisierung deutet auf die Unterdrückung der Kristallzwillingsdomänen auf Si(321) und Si(531) Substraten hin, wobei das Gesamtbild mittels einer erweiterten Probenserie vervollständigt werden kann. Für vergleichbare MnSi Dünnschichten auf Si(111), Si(321) und Si(531) ist die Curie-Weiss Temperatur innerhalb von 1 K und das kritische Magnetfeld innerhalb von 0.1 T identisch. Die Temperaturabhängigkeit des Magnetowiderstands zeigt das zu erwartende T^2 Verhalten nicht nur auf Si(111), sondern auch auf Si(321). Dies zeigt das erfolgreiche Wachstum von MnSi auf Si(321) und Si(531). Die letzteren Messungen ergeben außerdem einen Restwiderstand von weniger als der Hälfte für MnSi auf Si(321) im Vergleich zu Si(111). Dies kann durch die geringere Anzahl an Domänengrenzen erklärt werden und zeigt die erfolgreiche Unterdrückung einer Kristallzwillingsdomäne. Mit Hilfe der Restwiderstände und Hall-Messungen ist die Homogenität des Restwiderstandes und der Ladungsträgerdichte über einen großen Bereich des Wafers gezeigt.

Im vierten Teil werden der Anisotrope Magnetwiderstand und der Planare Hall Effekt für MnSi abhängig von den Winkeln von Stromrichtung und Magnetfeld im Bezug auf die Kristallrichtung untersucht. Dies wurde als Werkzeug zur Identifikation der Skyrmionenphase vorgeschlagen [YKT+15]. Der Einfluss der höheren C_{3v} Symmetrie des Kristallzwillingssystems und nicht der C_3 Symmetrie des B20 Einzelkristalls ist gezeigt Der Unterschied könnte ein nützliches zusätzliches Werkzeug für die Demonstration der Kristallzwillingsunterdrückung sein. Dies ist allerdings nur für die Rotation mit spezifischen symmetrischen Oberflächen möglich und nicht für die untersuchte unsymmetrische Si(321) Oberfläche. Messungen von MnSi Dünnschichten auf Si(111) oberhalb des kritischen Magnetfeldes zeigen die Abnahme der Anisotropie-Parameter für den Anisotropen Magnetwiderstand und den Planaren Hall-Effekt für steigenden Widerstand, wie aus der Literatur zu erwarten [WC67]. Auch wenn ein direkter Vergleich zu den Parametern für Dünnschichten auf Si(321) nicht möglich ist, können die größeren Parameterwerte bei Si(321) mit der reduzierten Streuung an Domänengrenzen erklärt werden. Die Analyse unterhalb des kritischen Magnetfeldes, der Bereich in dem eine mögliche Skyrmionenphase zu erwarten wäre, wird durch magnetische Hysterese verkompliziert. Nur ein Phasenübergang beim kritischen Magnetfeld kann deutlich gezeigt werden. Damit bleibt die Frage zur Existenz der Skyrmionen in den MnSi Dünnschichten weiter offen.

Die beste Möglichkeit diese Frage zu klären wäre ein direkterer Ansatz in Form von Lorentz-Transmissionselektronenmikroskopie, welche schon erfolgreich genutzt wurde um das Skyrmionengitter in dünnen Platten aus Volumenkristall MnSi zu visualisieren [TYY+12]. Für die Detektion von Skyrmionen in der Schichtebene müssten Lamellen für eine Seitenansicht präpariert werden, was prinzipiell möglich erscheint.

Die gezeigte erfolgreiche Unterdrückung von einem der Kristallzwillinge für MnSi Schichten auf Si(321) und Si(531) sollte außerdem auf andere Materialsysteme übertragbar sein. Die Kristallzwillingsbildung in FeGe auf Si(111) zu unterdrücken würde zu einem Skyrmionengitter mit einer einzigen Händigkeit bei annähernd Raumtemperatur führen [HC12]. Dies könnte Skyrmionen als Informationsträger in der Spintronik in greifbare Nähe bringen.

Bibliography

[AAFR99] A. Ahmadi, G. Attard, J. Feliu, and A. Rodes. Surface Reactivity at "Chiral" Platinum Surfaces. *Langmuir*, 15(7):2420, 1999.

[ANZR12] A. Allam, C. A. Nunes, J. Zalesak, and M.-C. Record. On the stability of the Higher Manganese Silicides. *Journal of Alloys and Compounds*, 512(1):278, 2012.

[ARE+18] A. S. Ahmed, J. Rowland, B. D. Esser, S. R. Dunsiger, D. W. McComb, M. Randeria, and R. K. Kawakami. Chiral bobbers and skyrmions in epitaxial FeGe/Si(111) films. *Physical Review Materials*, 2(4):041401, 2018.

[Bir66] R. R. Birss. *Symmetry and Magnetism*, volume 3 of *Series of monographs on selected topics in solid state physics*. North-Holland Pub. Co., second edition, 1966.

[Bir06] M. Birkholz. *Thin Film Analysis by X-Ray Scattering*. WILEY-VCH Verlag GmbH & Co. KGaA, 2006.

[BJ80] P. Bak and M. H. Jensen. Theory of helical magnetic structures and phase transitions in MnSi and FeGe. *Journal of Physics C: Solid State Physics*, 13(31):L881, 1980.

[BLM94] J. P. Becker, R. G. Long, and J. E. Mahan. Reflection high-energy electron diffraction patterns of carbide-contaminated silicon surfaces. *Journal of Vacuum Science & Technology A*, 12(1):174, 1994.

[BLRB10] A. B. Butenko, A. A. Leonov, U. K. Rößler, and A. N. Bogdanov. Stabilization of skyrmion textures by uniaxial distortions in noncentrosymmetric cubic helimagnets. *Physical Review B*, 82(5):052403, 2010.

[Bor] SEM and EDX measurements done together with Dr. Borzenko.

[Bru] Leptos version 7.6 (build 1) RHGWS software by Bruker AXS GmbH.

[BVJW75] D. Bloch, J. Voiron, V. Jaccarino, and J. H. Wernick. The high field-high pressure magnetic properties of MnSi. *Physics Letters A*, 51(5):259, 1975.

[BVR83] J. Beille, J. Voiron, and M. Roth. Long period helimagnetism in the cubic B20 Fe_xCo_{1-x}si and Co_xMn_{1-x} Si alloys. *Solid State Communications*, 47(5):399, 1983.

[BVT+81] J. Beille, J. Voiron, F. Towfiq, M. Roth, and Z. Y. Zhang. Helimagnetic structure of the Fe_x Co_{1-x} Si alloys. *Journal of Physics F: Metal Physics*, 11(10):2153, 1981.

[CDS+05] G. Ctistis, U. Deffke, K. Schwinge, J. J. Paggel, and P. Fumagalli. Growth of thin Mn films on Si(111)-7×7 and Si(111)-$\sqrt{3}\times\sqrt{3}$:Bi. *Physical Review B*, 71(3):035431, 2005.

[CF87] I. A. Campbell and A. Fert. *Transport Properties of Ferromagnets*, volume 3 of *Handbook of Ferromagnetic Materials*, chapter 9, page 747. Elsevier, reprinted edition, 1987.

[CIA17] CIAAW. Atomic weights of the elements 2017. http://ciaaw.org/atomic-weights.htm, 2017. Commission on Isotopic Abundances and Atomic Weights.

[Coe10] J. M. D. Coey. *Magnetism and Magnetic Materials*. Cambridge University Press, 2010.

[Con13] J. A. Constantino. *Characterization of Novel Magnetic Materials: Ultra-Thin (Ga,Mn)As and Epitaxial-Growth MnSi Thin Films*. Dissertation, urn:nbn:de:bvb:20-opus-90578, Julius-Maximilians-Universität Würzburg, 2013.

[DBS+18] B. Das, B. Balasubramanian, R. Skomski, P. Mukherjee, S. R. Vallopilly, G. C. Hadjipanayis, and D. J. Sellmyer. Effect of size confinement on skyrmionic properties of MnSi nanomagnets. *Nanoscale*, 10(20):9504, 2018.

[DGM+11] V. A. Dyadkin, S. V. Grigoriev, D. Menzel, D. Chernyshov, V. Dmitriev, J. Schoenes, S. V. Maleyev, E. V. Moskvin, and H. Eckerlebe. Control of chirality of transition-metal monosilicides by the Czochralski method. *Physical Review B*, 84(1):014435, 2011.

[DKS+17] C. Dhital, M. A. Khan, M. Saghayezhian, W. A. Phelan, D. P. Young, R. Y. Jin, and J. F. DiTusa. Effect of negative chemical pressure on the prototypical itinerant magnet MnSi. *Physical Review B*, 95(2):024407, 2017.

[Dör38] W. Döring. Die Abhängigkeit des Widerstandes von Nickelkristallen von der Richtung der spontanen Magnetisierung. *Annalen der Physik*, 424(3):259, 1938.

[Dzy58] I. E. Dzyaloshinsky. A thermodynamic theory of "weak" ferromagnetism of antiferromagnetics. *Journal of Physics and Chemistry of Solids*, 4(4):241, 1958.

[Dzy64] I. E. Dzyaloshinskii. Theory of Helicoidal Structures in Antiferromagnets. I. Nonmetals. *Journal of Experimental and Theoretical Physics*, 19(4):960, 1964.

[Ebe90] K. Eberl. *Herstellung und Charakterisierung von Silizium/Germanium Heterostrukturen und kurzperiodigen Übergittern.* Dissertation, Technische Universität München, 1990.

[EGN96] M. M. R. Evans, J. C. Glueckstein, and J. Nogami. Epitaxial growth of manganese on silicon: Volmer-Weber growth on the Si(111) surface. *Physical Review B*, 53(7):4000, 1996.

[ET82] M. Eizenberg and K. N. Tu. Formation and Schottky behavior of manganese silicides on n-type silicon. *Journal of Applied Physics*, 53(10):6885, 1982.

[FCS13] A. Fert, V. Cros, and J. Sampaio. Skyrmions on the track. *Nature Nanotechnology*, 8:152, 2013.

[Few15] P. F. Fewster. *X-Ray Scattering from Semiconductors and other Materials.* World Scientific, third edition, 2015.

[FSM13] K. Fabian, V. P. Shcherbakov, and S. A. McEnroe. Measuring the Curie temperature. *Geochemistry, Geophysics, Geosystems*, 14(4):947, 2013.

[FSP+18] C. D. Frye, C. K. Saw, B. Padavala, N. Khan, R. J. Nikolic, and J. H. Edgar. Suppression of Rotational Twins in Epitaxial $B_{12}P_2$ on 4H-SiC. *Crystal Growth & Design*, 18(2):669, 2018.

[GA90] A. B. Gokhale and R. Abbaschian. The Mn-Si (Manganese-Silicon) system. *Journal of Phase Equilibria*, 11(5):468, 1990.

[GKS+12] B. Geisler, P. Kratzer, T. Suzuki, T. Lutz, G. Costantini, and K. Kern. Growth mode and atomic structure of MnSi thin films on Si(111). *Physical Review B*, 86(11), 2012.

[GNJ+08] J. I. Goldstein, D. Newbury, D. Joy, C. Lyman, P. Echlin, E. Lifshin, L. Sawyer, and J. Michael. *Scanning Electron Microscopy and X-Ray Microanalysis*. Springer Science + Business Media, LLC, third, corrected printing edition, 2008.

[GWG17] M. Garst, J. Waizner, and D. Grundler. Collective spin excitations of helices and magnetic skyrmions: review and perspectives of magnonics in non-centrosymmetric magnets. *Journal of Physics D: Applied Physics*, 50(29):293002, 2017.

[Hah95] T. Hahn, editor. *Space-Group Symmetry*, volume A of *International Tables for Crystallography*. For The International Union of Crystallography by Kluwer Academic Publishers, fourth, revised edition, 1995.

[Har] Measurements done with Bachelor student M. Hartl.

[HC12] S. X. Huang and C. L. Chien. Extended Skyrmion Phase in Epitaxial FeGe(111) Thin Films. *Physical Review Letters*, 108(26):267201, 2012.

[HGZJ09] J. Hirvonen Grytzelius, H. M. Zhang, and L. S. O. Johansson. Coverage dependence and surface atomic structure of Mn/Si(111)-$\sqrt{3}\times\sqrt{3}$ studied by scanning tunneling microscopy and spectroscopy. *Physical Review B*, 80(23):235324, 2009.

[HIKT08] S. Higashi, Y. Ikedo, P. Kocán, and H. Tochihara. Epitaxially grown flat MnSi ultrathin film on Si(111). *Applied Physics Letters*, 93(1):013104, 2008.

[HKT09] S. Higashi, P. Kocán, and H. Tochihara. Reactive epitaxial growth of MnSi ultrathin films on Si(111) by Mn deposition. *Physical Review B*, 79(20):205312, 2009.

[HRS04] M. A. Herman, W. Richter, and H. Sitter. *Epitaxy: Physical Principles and Technical Implementation*, volume 62 of *Springer Series in Materials Science*. Springer-Verlag, 2004.

[HS96] M. A. Herman and H. Sitter. *Molecular Beam Epitaxy*, volume 7 of *Springer Series in Materials Science*. Springer-Verlag, second, revised and updated edition, 1996.

[HS04] J.H. Hubbel and S. M. Seltzer. Tables of X-Ray Mass Attenuation Coefficients and Mass Energy-Absorption Coefficients (version 1.4) [Online]. http://physics.nist.gov/xaamdi [2018.10.15], 2004. National Institute of Standards and Technology, Gaithersburg, MD.

[Hur74] C. M. Hurd. Galvanomagnetic effects in anisotropic metals. *Advances in Physics*, 23(2):315, 1974.

[IC04] A. Ichimiya and P. I. Cohen. *Reflection High Energy Electron Diffraction*. Cambridge University Press, 2004.

[IEM+85] M. Ishida, Y. Endoh, S. Mitsuda, Y. Ishikawa, and M. Tanaka. Crystal Chirality and Helicity of the Helical Spin Density Wave in MnSi. II. Polarized Neutron Diffraction. *Journal of the Physical Society of Japan*, 54(8):2975, 1985.

[ITBR76] Y. Ishikawa, K. Tajima, D. Bloch, and M. Roth. Helical spin structure in manganese silicide MnSi. *Solid State Communications*, 19(6):525, 1976.

[JKK+15] L. Jogschies, D. Klaas, R. Kruppe, J. Rittinger, P. Taptimthong, A. Wienecke, L. Rissing, and M. C. Wurz. Recent Developments of Magnetoresistive Sensors for Industrial Applications. *Sensors*, 15(11):28665, 2015.

[JMP+10] F. Jonietz, S. Mühlbauer, C. Pfleiderer, A. Neubauer, W. Münzer, A. Bauer, T. Adams, R. Georgii, P. Böni, R. A. Duine, K. Everschor, M. Garst, and A. Rosch. Spin Transfer Torques in MnSi at Ultralow Current Densities. *Science*, 330(6011):1648, 2010.

[JP07] S. J. Jenkins and S. J. Pratt. Beyond the surface atlas: A roadmap and gazetteer for surface symmetry and structure. *Surface Science Reports*, 62(10):373, 2007.

[JR91] J.-E. Jørgensen and S. E. Rasmussen. Refinement of the Structure of MnSi by Powder Diffraction. *Powder Diffraction*, 6(4):194, 1991.

[KBSR11] N. S. Kiselev, A. N. Bogdanov, R. Schäfer, and U. K. Rößler. Chiral skyrmions in thin magnetic films: New objects for magnetic storage technologies? *Journal of Physics D: Applied Physics*, 44(39):392001, 2011.

[KHZ+16] W. Kang, Y. Huang, X. Zhang, Y. Zhou, and W. Zhao. Skyrmion-Electronics: An Overview and Outlook. *Proceedings of the IEEE*, 104(10):2040, 2016.

[KKM+10] E. Karhu, S. Kahwaji, T. L. Monchesky, C. Parsons, M. D. Robertson, and C. Maunders. Structure and magnetic properties of MnSi epitaxial thin films. *Physical Review B*, 82(18):184417, 2010.

[KKR+11] E. A. Karhu, S. Kahwaji, M. D. Robertson, H. Fritzsche, B. J. Kirby, C. F. Majkrzak, and T. L. Monchesky. Helical magnetic order in MnSi thin films. *Physical Review B*, 84(6):060404, 2011.

[KKS+97] V. M. Kaganer, R. Köhler, M. Schmidbauer, R. Opitz, and B. Jenichen. X-ray diffraction peaks due to misfit dislocations in heteroepitaxial structures. *Physical Review B*, 55(3):1793, 1997.

[KOD82] K. Kadowaki, K. Okuda, and M. Date. Magnetization and Magnetoresistance of MnSi. I. *Journal of the Physical Society of Japan*, 51(8):2433, 1982.

[KPS+16] C. Koppka, A. Paszuk, M. Steidl, O. Supplie, P. Kleinschmidt, and T. Hannappel. Suppression of Rotational Twin Formation in Virtual

GaP/Si(111) Substrates for III–V Nanowire Growth. *Crystal Growth & Design*, 16(11):6208, 2016.

[KRB+12] E. A. Karhu, U. K. Rößler, A. N. Bogdanov, S. Kahwaji, B. J. Kirby, H. Fritzsche, M. D. Robertson, C. F. Majkrzak, and T. L. Monchesky. Chiral modulations and reorientation effects in MnSi thin films. *Physical Review B*, 85(9):094429, 2012.

[KTH+04] A. Kumar, M. Tallarida, M. Hansmann, U. Starke, and K. Horn. Thin manganese films on Si(111)-(7×7): electronic structure and strain in silicide formation. *Journal of Physics D: Applied Physics*, 37(7):1083, 2004.

[KYKI76] S. Kusaka, K. Yamamoto, T. Komatsubara, and Y. Ishikawa. Ultrasonic study of magnetic phase diagram of MnSi. *Solid State Communications*, 20(9):925, 1976.

[LBA+70] L. Ludgren, O. Beckman, V. Attia, S. P. Bhattacheriee, and M. Richardson. Helical Spin Arrangement in Cubic FeGe. *Physica Scripta*, 1(1):69, 1970.

[LKY+13] Y. Li, N. Kanazawa, X. Z. Yu, A. Tsukazaki, M. Kawasaki, M. Ichikawa, X. F. Jin, F. Kagawa, and Y. Tokura. Robust Formation of Skyrmions and Topological Hall Effect Anomaly in Epitaxial Thin Films of MnSi. *Physical Review Letters*, 110(11):117202, 2013.

[LKY+14] Y. Li, N. Kanazawa, X. Z. Yu, F. Kagawa, and Y. Tokura. Li *et al.* Reply. *Physical Review Letters*, 112(5):059702, 2014.

[LT87] H. M. Liu and T. T. Tsong. Atomic structures of several silicon surfaces: A direct field ion microscope observation. *Journal of Applied Physics*, 62(4):1532, 1987.

[Mat75] J. W. Matthews. Coherent interfaces and misfit dislocations. In *Epitaxial Growth part B*, Materials Science and Technology, chapter 8, page 559. Academic Press, 1975.

[MBC+10] E. Magnano, F. Bondino, C. Cepek, F. Parmigiani, and M. C. Mozzati. Ferromagnetic and ordered MnSi(111) epitaxial layers. *Applied Physics Letters*, 96(15):152503, 2010.

[MBJ+09] S. Mühlbauer, B. Binz, F. Jonietz, C. Pfleiderer, A. Rosch, A. Neubauer, R. Georgii, and P. Böni. Skyrmion Lattice in a Chiral Magnet. *Science*, 323(5916):915, 2009.

[MCG96] C. F. McFadden, P. S. Cremer, and A. J. Gellman. Adsorption of Chiral Alcohols on “Chiral” Metal Surfaces. *Langmuir*, 12(10):2483, 1996.

[MCN+06] E. Magnano, E. Carleschi, A. Nicolaou, T. Pardini, M. Zangrando, and F. Parmigiani. Growth of manganese silicide films by co-deposition of Mn and Si on Si(111): A spectroscopic and morphological investigation. *Surface Science*, 600(18):3932, 2006.

[MI11] K. Momma and F. Izumi. VESTA 3 for three-dimensional visualization of crystal, volumetric and morphology data. *Journal of Applied Crystallography*, 44(6):1272, 2011.

[MLRB14] T. L. Monchesky, J. C. Loudon, M. D. Robertson, and A. N. Bogdanov. Comment on “Robust Formation of Skyrmions and Topological Hall Effect Anomaly in Epitaxial Thin Films of MnSi”. *Physical Review Letters*, 112(5):059701, 2014.

[MM78] K. Makoshi and T. Moriya. Theory of Helical Spin Structure in Itinerant Electron Systems. II. *Journal of the Physical Society of Japan*, 44(1):80, 1978.

[MNT16] P. J. Mohr, D. B. Newell, and B. N. Taylor. CODATA recommended values of the fundamental physical constants: 2014. *Reviews of Modern Physics*, 88(3):035009, 2016.

[Mor60] T. Moriya. Anisotropic Superexchange Interaction and Weak Ferromagnetism. *Physical Review*, 120(1):91, 1960.

[Mor76] T. Moriya. Theory of helical spin structure in itinerant electron systems. *Solid State Communications*, 20(3):291, 1976.

[MP75] T. McGuire and R. Potter. Anisotropic magnetoresistance in ferromagnetic 3d alloys. *IEEE Transactions on Magnetics*, 11(4):1018, 1975.

[MSK+13] D. Morikawa, K. Shibata, N. Kanazawa, X. Z. Yu, and Y. Tokura. Crystal chirality and skyrmion helicity in MnSi and (Fe, Co)Si as determined by transmission electron microscopy. *Physical Review B*, 88(2):024408, 2013.

[MWK+17] S. A. Meynell, M. N. Wilson, K. L. Krycka, B. J. Kirby, H. Fritzsche, and T. L. Monchesky. Neutron study of in-plane skyrmions in MnSi thin films. *Physical Review B*, 96(5):054402, 2017.

[MWL+14] S. A. Meynell, M. N. Wilson, J. C. Loudon, A. Spitzig, F. N. Rybakov, M. B. Johnson, and T. L. Monchesky. Hall effect and transmission electron microscopy of epitaxial MnSi thin films. *Physical Review B*, 90(22):224419, 2014.

[Nab79] F. R. N. Nabarro, editor. *Dislocations in Crystals*, volume 2 of *Dislocations in Solids*, chapter 7. North-Holland Publ. Co., 1979.

[NNK+15] Y. Nii, T. Nakajima, A. Kikkawa, Y. Yamasaki, K. Ohishi, J. Suzuki, Y. Taguchi, T. Arima, Y. Tokura, and Y. Iwasa. Uniaxial stress control of skyrmion phase. *Nature Communications*, 6:8539, 2015.

[NOMH99] T. Nagao, S. Ohuchi, Y. Matsuoka, and S. Hasegawa. Morphology of ultrathin manganese silicide on Si(111). *Surface Science*, 419(2):134, 1999.

[NPB+09] A. Neubauer, C. Pfleiderer, B. Binz, A. Rosch, R. Ritz, P. G. Niklowitz, and P. Böni. Topological Hall Effect in the *A* Phase of MnSi. *Physical Review Letters*, 102(18):186602, 2009.

[NSO+10] N. Nagaosa, J. Sinova, S. Onoda, A. H. MacDonald, and N. P. Ong. Anomalous Hall effect. *Reviews of Modern Physics*, 82(2):1539, 2010.

[NT13] N. Nagaosa and Y. P. Tokura. Topological properties and dynamics of magnetic skyrmions. *Nature Nanotechnology*, 8:899, 2013.

[NYHK80] O. Nakanishi, A. Yanase, A. Hasegawa, and M. Kataoka. The origin of the helical spin density wave in MnSi. *Solid State Communications*, 35(12):995, 1980.

[PJK05] S. J. Pratt, S. J. Jenkins, and D. A. King. The symmetry and structure of crystalline surfaces. *Surface Science*, 585(1):L159, 2005.

[PMJL97] C. Pfleiderer, G. J. McMullan, S. R. Julian, and G. G. Lonzarich. Magnetic quantum phase transition in MnSi under hydrostatic pressure. *Physical Review B*, 55(13):8330, 1997.

[Poh13] C. Pohl. *Silicon Based MBE of Manganese-Silicide and Silicon-Suboxide*. Dissertation, urn:nbn:de:bvb:20-opus-83757, Julius-Maximilians-Universität Würzburg, 2013.

[RAM+17] P. K. Rout, I. Agireen, E. Maniv, M. Goldstein, and Y. Dagan. Six-fold crystalline anisotropic magnetoresistance in the (111) $LaAlO_3/SrTiO_3$ oxide interface. *Physical Review B*, 95(24):241107, 2017.

[RHF+13] R. Ritz, M. Halder, C. Franz, A. Bauer, M. Wagner, R. Bamler, A. Rosch, and C. Pfleiderer. Giant generic topological Hall resistivity of MnSi under pressure. *Physical Review B*, 87(13):134424, 2013.

[RVK+07] A. W. Rushforth, K. Výborný, C. S. King, K. W. Edmonds, R. P. Campion, C. T. Foxon, J. Wunderlich, A. C. Irvine, P. Vašek, V. Novák, K. Olejník, J. Sinova, T. Jungwirth, and B. L. Gallagher. Anisotropic Magnetoresistance Components in (Ga,Mn)As. *Physical Review Letters*, 99(14):147207, 2007.

[SAA+97] S. M. Shivaprasad, C. Anandan, S. G. Azatyan, Y. L. Gavriljuk, and V. G. Lifshits. The formation of MnSi(111) interface at room and high temperatures. *Surface Science*, 382(1):258, 1997.

[Sch16] S. Schreyeck. *Molecular Beam Epitaxy and Characterization of Bi-Based V_2VI_3 Topological Insulators*. Dissertation, urn:nbn:de:bvb:20-opus-145812, Julius-Maximilians-Universität Würzburg, 2016.

[SIF+09] H. Suto, K. Imai, S. Fujii, S.-i. Honda, and M. Katayama. Growth process and surface structure of MnSi on Si(111). *Surface Science*, 603(1):226, 2009.

[SMM+05] K. Schwinge, C. Müller, A. Mogilatenko, J. J. Paggel, and P. Fumagalli. Structure and magneto-optic Kerr measurements of epitaxial MnSi films on Si(111). *Journal of Applied Physics*, 97(10):103913, 2005.

[SPT73] K. E. Sundström, S. Petersson, and P. A. Tove. Studies of formation of silicides and their barrier heights to silicon. *physica status solidi (a)*, 20(2):653, 1973.

[SSN11] M. Sawicki, W. Stefanowicz, and A. Ney. Sensitive SQUID magnetometry for studying nanomagnetism. *Semiconductor Science and Technology*, 26(6):064006, 2011.

[Sta87] P. A. Stadelmann. EMS - a software package for electron diffraction analysis and HREM image simulation in materials science. *Ultramicroscopy*, 21(2):131, 1987.

[Tar] TEM measurements and analysis done by Dr. Tarakina.

[TFL90] J. D. Thompson, Z. Fisk, and G. G. Lonzarich. Perspective on heavy-electron and Kondo-lattice systems from high pressure studies. *Physica B: Condensed Matter*, 161(1):317, 1990.

[Tho57] W. Thomson. XIX. On the Electro-dynamic Qualities of Metals:—Effects of Magnetization on the Electric Conductivity of Nickel and of Iron. *Proceedings of the Royal Society of London*, 8:546, 1857.

[TPSF97] C. Thessieu, C. Pfleiderer, A. N. Stepanov, and J. Flouquet. Field dependence of the magnetic quantum phase transition in MnSi. *Journal of Physics: Condensed Matter*, 9(31):6677, 1997.

[TTIE85] M. Tanaka, H. Takayoshi, M. Ishida, and Y. Endoh. Crystal Chirality and Helicity of the Helical Spin Density Wave in MnSi. I. Convergent-Beam Electron Diffraction. *Journal of the Physical Society of Japan*, 54(8):2970, 1985.

[TTP+17] M. Trabel, N. V. Tarakina, C. Pohl, J. A. Constantino, C. Gould, K. Brunner, and L. W. Molenkamp. Twin domains in epitaxial thin MnSi layers on Si(111). *Journal of Applied Physics*, 121(24):245310, 2017.

[TYY+12] A. Tonomura, X. Yu, K. Yanagisawa, T. Matsuda, Y. Onose, N. Kanazawa, H. S. Park, and Y. Tokura. Real-Space Observation of Skyrmion Lattice in Helimagnet MnSi Thin Samples. *Nano Letters*, 12(3):1673, 2012.

[UM75] K. Ueda and T. Moriya. Contribution of Spin Fluctuations to the Electrical and Thermal Resistivities of Weakly and Nearly Ferromagnetic Metals. *Journal of the Physical Society of Japan*, 39(3):605, 1975.

[War90] B. E. Warren. *X-Ray Diffraction.* Dover Publications, INC., Dover edition, 1990.

[WBBM14] M. N. Wilson, A. B. Butenko, A. N. Bogdanov, and T. L. Monchesky. Chiral skyrmions in cubic helimagnet films: The role of uniaxial anisotropy. *Physical Review B*, 89(9):094411, 2014.

[WC67] R. H. Walden and R. F. Cotellessa. Magnetoresistance of Nickel-Copper Single-Crystal Thin Films. *Journal of Applied Physics*, 38(3):1335, 1967.

[WCZ+17] B. Wiedemann, A. Chacon, S. L. Zhang, Y. Khaydukov, T. Hesjedal, O. Soltwedel, T. Keller, S. Mühlbauer, T. Adams, M. Halder, C. Pfleiderer, and P. Böni. Reciprocal space mapping of magnetic order in thick epitaxial MnSi films. *arXiv:1710.00544 [cond-mat.str-el]*, 2017.

[Wil95] A. J. C. Wilson, editor. *Mathematical, Physical and Chemical Tables*, volume C of *International Tables for Crystallography.* For The International Union of Crystallography by Kluwer Academic Publishers, 1995.

[WKL+13] M. N. Wilson, E. A. Karhu, D. P. Lake, A. S. Quigley, S. Meynell, A. N. Bogdanov, H. Fritzsche, U. K. Rößler, and T. L. Monchesky. Discrete helicoidal states in chiral magnetic thin films. *Physical Review B*, 88(21):214420, 2013.

[WKQ+12] M. N. Wilson, E. A. Karhu, A. S. Quigley, U. K. Rößler, A. B. Butenko, A. N. Bogdanov, M. D. Robertson, and T. L. Monchesky. Extended elliptic skyrmion gratings in epitaxial MnSi thin films. *Physical Review B*, 86(14):144420, 2012.

[Woh78] E. P. Wohlfarth. Magnetic properties of crystalline and amorphous alloys: A systematic discussion based on the Rhodes-Wohlfarth plot. *Journal of Magnetism and Magnetic Materials*, 7(1):113, 1978.

[WWSW66] H. J. Williams, J. H. Wernick, R. C. Sherwood, and G. K. Wertheim. Magnetic Properties of the Monosilicides of Some 3d Transition Elements. *Journal of Applied Physics*, 37(3):1256, 1966.

[YGC+04] Z. Yang, Y. Gu, L. Chen, L. Shi, J. Ma, and Y. Qian. Preparation of Mn_5Si_3 nanocages and nanotubes by molten salt flux. *Solid State Communications*, 130(5):347, 2004.

[YKO+11] X. Z. Yu, N. Kanazawa, Y. Onose, K. Kimoto, W. Z. Zhang, S. Ishiwata, Y. Matsui, and Y. Tokura. Near room-temperature formation of a skyrmion crystal in thin-films of the helimagnet FeGe. *Nature Materials*, 10(2):106, 2011.

[YKT+15] T. Yokouchi, N. Kanazawa, A. Tsukazaki, Y. Kozuka, A. Kikkawa, Y. Taguchi, M. Kawasaki, M. Ichikawa, F. Kagawa, and Y. Tokura. Formation of In-plane Skyrmions in Epitaxial MnSi Thin Films as Revealed by Planar Hall Effect. *Journal of the Physical Society of Japan*, 84(10):104708, 2015.

[Zae17] F. Zaera. Chirality in adsorption on solid surfaces. *Chemical Society Reviews*, 46(23):7374, 2017.

[ZL11] Z.-Q. Zou and W.-C. Li. Two-dimensional fractal-like growth on semiconductors: The formation of continuous manganese monosilicide ultrathin films on Si(111). *Physics Letters A*, 375(4):849, 2011.

[ZTTF02] Q. Zhang, M. Tanaka, M. Takeguchi, and K. Furuya. Analytical UHV transmission electron microscopy studies of electronic structure changes between as-deposited Mn and Mn silicide on Si(111) surface. *Surface Science*, 507-510:453, 2002.

Publications

1. M. Trabel, N. V. Tarakina, C. Pohl, J. A. Constantino, C. Gould, K. Brunner, and L. W. Molenkamp. Twin Domains in Epitaxial Thin MnSi Layers on Si(111). *Journal of Applied Physics*, 121(24):245310, 2017.

2. M. Trabel, M. Baussenwein, C. Gould, M. Sawicki, K. Brunner, and L. W. Molenkamp. Crystalline anisotropic magnetoresistance in epitaxial thin MnSi layers on Si(111) and the influence of twinning. Manuscript in preparation.

Conference contributions

1. M. Trabel, B. Halbig, N. V. Tarakina, C. Pohl, U. Bass, C. Gould, J. Geurts, K. Brunner, and L. W. Molenkamp. Twisted twin domains in epitaxial thin MnSi layers on Si(111). Presentation, *DPG conference Berlin*, 2015.

2. M. Trabel, N. V. Tarakina, C. Pohl, M. Sawicki, C. Gould, K. Brunner, and L. W. Molenkamp. Investigations of Structural, Magnetic and Electrical Properties of Thin Epitaxial MnSi Layers. Poster, *Jaszowiec conference*, 2015.

Acknowledgments

I want to thank all people contributing to the success of this work.
First of all Prof. Dr. Laurens W. Molenkamp for the possibility to do my PhD thesis at his chair.
Prof. Dr. Karl Brunner for his great supervision and interesting ideas for the project.
Prof. Dr. Charles Gould for his supervision of the magnetotranport and magnetometry parts of this project.
All former PhD students who worked on the project

- Dr. Tsvetelina Naydenova, Dr. Jennifer Anne Constantino and Dr. Christoph Pohl.

All the Exchange, Bachelor, Master and PhD students directly working on the project, without whom it would not have been possible

- Ruilin Liang,
- Dominik Schindler, Matthias Hartl, André Kowalewski,
- Benedikt Halbig, Henrik Straßberger
- and Martin Baußenwein.

Experts from other scientific fields for collaboration on the project

- Dr. Maximilian Kessel, Dr. Tanja Borzenko, Dr. Nadezda Tarakina, Dr. Utz Baß, Prof. Dr. Jean Geurts and Prof. Dr. hab. Maciej Sawicki.

The technical staff for molecular beam epitaxie and cleanroom

- Martin Zipf, Volkmar Hock, Petra Wolf-Müller and Carmen Bundschuh,

for the magnetotransportlabs and liquid nitrogen and helium supplies

- Roland Ebert and Cornelius-Sebastian Ziga,

and the whole scientific workshop for research and teaching. My office colleagues for the great atmosphere and interesting discussions

- Pascal Laudenbach, Lukas Lunczer, Dr. Christopher Ames and especially Dr. Steffen Schreyeck for his scientific input.

The whole chair of Experimental Physics 3 for the great atmosphere, and especially Andreas Budewitz, Simon Hartinger and David Mahler for all the interesting discussions as well as support in the lab.
And last but not least my family and my girlfriend Nanda who supported me during all this time.